NTNU

Norwegian University of
Science and Technology

Numerical Analyses of Moment Resisting Beam-to-Column Connections in Timber Structures

Anders Fristad Drageset

Torbjørn Hadland Hoff

Master of Science in Civil and Environmental Engineering
Submission date: June 2017
Supervisor: Kjell A Malo, KT
Co-supervisor: Haris Stamatopoulos, KT

Norwegian University of Science and Technology
Department of Structural Engineering

Department of Structural Engineering
Faculty of Engineering Science and Technology
NTNU- Norwegian University of Science and Technology

ACCESSIBILITY

OPEN

MASTER THESIS 2017

SUBJECT AREA:	DATE:	NO. OF PAGES:
Structural Engineering	11.06.17	97 + 27 Appendix

TITLE:

Numerical Analyses of Moment Resisting Beam-to-Column Connections in Timber Structures

Numeriske analyser av momentstive bjelke-søyle forbindelser i trekonstruksjoner

BY:

Anders Fristad Drageset

Torbjørn Hadland Hoff

SUMMARY:
This Master thesis is a continuation of an ongoing study of connections in timber structures with the use of long threaded rods as fasteners. As a part of the research project *Wood frame solutions for free space design in urban buildings*, the objective has been to optimize a moment resisting beam-to-column connection by use of numerical analyses. The main focus has been optimizing both the inclination angle of the rods and the steel connector between the beam and the column, in order to obtain high rotational stiffness.

Previously two configurations, using connecting circular profile, have been tested experimentally. These were replicated numerically in order to validate the results from the simulations. The rotational stiffness in the numerical models were 10 545 kNm/rad and 13 813 kNm/rad for the two configurations, while the results from the experimental testing were 9 079 kNm/rad and 7 603 kNm/rad respectively. The correlating results for one configuration, but large discrepancy for the other, were contributed to the inability of the cohesive zone to replicate the experimental withdrawal stiffness for the angles and embedment lengths featured in the latter configuration.

A new steel connector was designed. The concept is a plate bent to accommodate the rod inclinations. The numerical simulations resulted in a higher rotational stiffness than the previously used circular profile. Nine configurations with varying rod-to-grain angles, connector types and dimensions of the timber components were analyzed. A configuration where the column rods had inclinations of 75 and 70 degrees relative to the grains and the beam rod 5 degrees, achieved the highest rotational stiffness with a magnitude of 20 796 kNm/rad. By comparing the numerical and experimental results, the experimental rotational stiffness may be in the range of 11 404 - 13 783 kNm/rad.

A configuration designed based on fire requirements, possessing a larger width of the timber components, and column rods in different planes, displayed promising results. Although one rod was located within the charring depth, the connection were able to sustain the loading in SLS.

RESPONSIBLE TEACHER: Kjell Arne Malo
SUPERVISOR(S): Kjell Arne Malo, Haris Stamatopoulos
CARRIED OUT AT: Department of Structural Engineering, NTNU

MASTEROPPGAVE 2017

Anders Fristad Drageset og Torbjørn Hadland Hoff

Numerical Analyses of Moment Resisting Beam-to-Column Connections in Timber Structures

(Numeriske analyser av momentstive bjelke-søyle forbindelser i trekonstruksjoner)

Kandidatene skal videreutvikle et knutepunkt mellom bjelke-søyle fobindelser i limtre ved hjelp av numeriske analyser. Det skal benyttes skråstilte aksialbærende treskruer (gjengestenger) som forbindelsesmiddel. Dette arbeidet er en del av prosjektet Woodsols, hvor en viktig del av prosjektet er å videreutvikle knutepunkt med momentstive egenskaper. Oppgavens hovedformål er å optimalisere innskruingsvinklene til gjengestengene og forbedre det sammenkoblende stålprofilet basert på tidligere utført arbeid.

Oppgaven omfatter et litteraturstudie og numeriske modelleringer av hele knutepunktet. Analysene skal benyttes for å undersøke hvilke innskruingsvinkler og sammenkoblingsmetoder som er gunstige med tanke på kapasitet og stivhet, og om det er mulig å benytte slike knutepunkt i høye og store trekonstruksjoner i framtiden.

Forutsetninger: De numeriske resultatene skal evalueres ut i fra eksperimentelle forsøk, analytiske beregningsmetoder og andre numeriske modeller hvor dette er tilgjengelig.

Veileder: Kjell Arne Malo
Medveileder: Haris Stamatopoulos

Besvarelsen skal leveres til Institutt for konstruksjonsteknikk 11. juni 2017.

Preface

This thesis is a part of the 2-year Masters degree program Civil and Environmental Engineering. The study is written at the Department of Structural Engineering, NTNU, during the Spring semester of 2017. The thesis is a part of the research project *Wood frame solutions for free space design in urban buildings*, led by Kjell Arne Malo for NTNU.

The study is based on numerical analyses of timber connections. The main focus is optimisation of the configuration of axially loaded threaded rods in order to design a moment resisting beam-to-column connection.

We would like to express our gratitude to Kjell Arne Malo and Haris Stamatopoulos for excellent supervising and guidance through the entire study. Additionally, we would like to thank Ph.D-candidate Aivars Vilguts for valuable input and wish him luck with the continued work of his thesis. Hopefully the work presented in this thesis can be of use. Finally, we would like to thank all our classmates in the Civil and Environmental Engineering class for making the two years here at NTNU so memorable.

Trondheim, Sunday 11st June, 2017

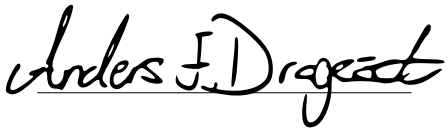

Anders Fristad Drageset

Torbjørn Hadland Hoff

Abstract

This Master thesis is a continuation of an ongoing study of connections in timber structures with the use of long threaded rods as fasteners. As a part of the research project *Wood frame solutions for free space design in urban buildings*, the objective has been to optimise a moment resisting beam-to-column connection by use of numerical analyses. The main focus has been optimising both the inclination angle of the rods and the steel connector between the beam and the column, in order to obtain high rotational stiffness.

To simulate withdrawal of the rods in the numerical models, cohesive zones were implemented. The stiffness parameters of the cohesive zone were calibrated according to both numerical simulations featuring threaded rods, and experimental tests. The numerical and experimental withdrawal stiffness correlated well, especially for smaller angles and longer embedment lengths.

Previously, two configurations using a connecting circular steel profile have been tested experimentally. These were replicated numerically to validate the results from the simulations. The rotational stiffness of the numerical models were 10 545 and 13 813 kN m/rad for the two configurations, while the results from the experimental testing were 9079 and 7603 kN m/rad respectively. The correlating results for one configuration, but large discrepancy for the other, were contributed to the inability of the cohesive zone to replicate the experimental withdrawal stiffness for the featured angles and embedment lengths.

A new steel connector was designed. The concept is a plate bent to accommodate the rod inclinations. The numerical simulations indicated a higher rotational stiffness than the previously used circular profile.

Nine configurations with varying rod-to-grain angles, connector types and dimensions of the timber components were analysed. A configuration where the column rods had inclinations of 75 and 70 degrees relative to the grains and the beam rod 5 degrees, achieved the highest rotational stiffness with a magnitude of 20 796 kN m/rad. By comparing the numerical and experimental results, the experimental rotational stiffness may be in the range of 11 404-13 783 kN m/rad.

A configuration designed based on fire requirements, possessing a larger width of the timber components and column rods in different planes, displayed promising results. Although one rod was located within the charring depth, the connection had sufficient capacity to sustain the loading in SLS in a fire situation.

Sammendrag

Denne masteroppgaven er en videreføring av et pågående studie, som tar for seg forbindelser i trekonstruksjoner med bruk av lange gjengestenger som fester. Som en del av forskningsprosjektet *Wood frame solutions for free space design in urban buildings*, har hovedoppgaven vært å optimalisere momentstive bjelke-til-søyle forbindelser ved bruk av numeriske beregningsverktøy.

For å simulere uttrekk av gjengestenger i de numeriske modellene, ble kohesive soner benyttet. Stivhetsparametrene i de kohesive sonene ble kalibrert etter test-resultater fra eksperimentelle forsøk. Deretter sammenliknet opp mot liknende numeriske modeller hvor det var benyttet gjengede stenger. De numeriske verdiene sammenliknet med de eksperimentelle ga sammenfallende resultater, spesielt for lavere vinkler og lengre innføringslengder.

Det er tidligere gjennomført eksperimentelle tester på forbindelser hvor det ble benyttet sirkulære stålforbindere. Disse ble gjenskapt numerisk for å kunne validere nøyaktigheten av de numeriske resultatene. Rotasjonstivheten for de numeriske modellene var 10 545 og 13 813 kN m/rad, mens de eksperimentelle målingene ga henholdsvis 9079 og 7603 kN m/rad. De sammenfallende verdiene for en av forbindelsene og avvikende resultater for den andre, skyldes større avvik mellom eksperimentelle og numeriske uttrekksstivheter for de aktuelle vinklene og innføringslengdene.

Et nytt sammenkoblende stålprofil ble utviklet. Konseptet er en plate tilpasset innskruingsvinklene til gjengestengene. De numeriske simuleringene indikerte høyere rotasjonsstivhet enn det tidligere benyttede sirkelprofilet.

Ni forbindelser med ulike innskruingsvinkler, sammenkoblingsmetoder og dimensjoner på limtrekomponentene ble analysert. En forbindelse med innskruingsvinkler på 75 og 70 grader i søylen og 5 grader i bjelken resulterte i den høyeste rotasjonstivheten med en verdi på 20 796 kN m/rad. Ved å sammenligne de numeriske og eksperimentelle verdiene, kan dette gi en reell rotasjonsstivhet på 11 404-13 783 kN m/rad.

En forbindelse dimensjonert etter brannkrav, med større bredde på limtrekomponentene og gjengestengene i søylen i ulike plan, viste lovende resultater. Selv om en av stengene var plassert innenfor forkullingsdybden, hadde forbindelsen tilstrekkelig kapasitet til å bære lasten i bruksgrensetilstand ved brann.

Contents

Preface **i**

Abstract **iii**

Sammendrag **v**

1 Introduction **1**
1.1 Background 1
1.2 Scope of thesis 2
1.3 Limitations 2

2 Theory **3**
2.1 Connections 3
2.2 Components in a connection 5
2.2.1 Wood as a structural material 5
2.2.2 Fasteners 7
2.3 Rigid joints in timber structures 8
2.3.1 Beam-to-column connections 8
2.4 State of the art 10
2.5 Summary 18

3 Connection **19**
3.1 Optimization of rod configuration 19
3.1.1 Force distribution 21
3.1.2 Component method 24
3.2 Withdrawal properties 31
3.2.1 Numerical modelling 31
3.2.2 Cohesive withdrawal properties 37
3.3 Connector 45
3.3.1 Circular profile 45
3.3.2 Design criteria 46
3.3.3 Design procedure 46
3.3.4 Rotational stiffness of the connector 48
3.3.5 Assembly 53
3.4 Numerical models of various configurations 55
3.4.1 An overview of the configurations 58
3.5 Fire design 59

4 Results **64**
4.1 Axial forces in the rods 64
4.2 Rotational stiffness 66
4.3 Stresses in the column 67
4.3.1 Stress states for selected configurations 68
4.3.2 Comparison 71
4.4 Deflection of the beam 75

5 Evaluation **76**
5.1 Numerical modelling 76
5.1.1 Withdrawal properties 76
5.1.2 Connector 79
5.1.3 Models of configurations 81
5.2 Results 83
5.2.1 Axial forces in the rods 83
5.2.2 Rotational stiffness 83
5.2.3 Stresses in the column 84
5.2.4 Deflection of the beam 88
5.3 Connector 89
5.3.1 Design 89
5.3.2 Assembly 90

6 Concluding remarks **92**
6.1 Conclusion 92
6.2 Proposals for future work 94

References **95**

Appendices **100**

A Calculations **100**
A.1 Force distribution - MatLab-script 100
A.2 Acting moment in the joint 101
A.3 Comparison of material usage 103
A.4 Component method applied to the steel plate 104

B Cohesive zone parameters **105**
B.1 Withdrawal calibrated at l = 100 mm 105
B.2 Withdrawal calibrated at l = 300 mm 106

C Sketches of the configurations **107**

D Stresses in the column **112**
D.1 Stress states 112
D.2 Comparisons 115
D.2.1 Center 115
D.2.2 Left 116

E Stresses in the rods - Withdrawal models **117**

F Documentation of numerical models **123**
F.1 Withdrawal models 123
F.2 Connector 124
F.3 Connection 125

G Digital resources **127**

1. Introduction

In this chapter the background, objective and limitations of this master thesis will be presented. The thesis is a part of the research project *Wood frame solutions for free space design in urban buildings* (abbriv. WoodSols), whose main objective is to develop industrialised structural solutions based on rigid wooden frames for use in urban buildings having five to ten stories open architecture [1].

1.1 Background

The research project WoodSols' main goal is to develop structural solutions that can make the use of timber in urban constructions more attractive. As a part of achieving this objective, the development of moment resisting frames is an important task. The purpose of a moment resisting frame is to horizontally stabilise a structure in the plane of the frame. Paramount in these frames, is the connection between the horizontal and vertical timber components. The beam-to-column connections have to be as rigid as possible for the frame to obtain moment resisting properties. Increased lateral stiffness facilitate more open and flexible architecture as the need for stabilising measures is reduced.

The intention of the project is to develop solutions that can be used in an industrialised structural system. In order to achieve this objective, an uncomplicated assembly phase of the connection is critical. Additionally, the connection has to possess sufficient capacity, also in the case of fire.

1.2 Scope of thesis

This Master thesis is a continuation of an ongoing study of connections in timber structures with the use of long threaded rods as fasteners. The objective of this thesis is to optimise a moment resisting beam-to-column connection by use of numerical analyses. The main focus is optimising both the inclination angle of the rods and the steel connector between beam-to-column interaction.

The experimental testing performed by Lied & Nordal [2] will be used to validate the numerical results.

1.3 Limitations

The priority in this thesis was to establish comprehensive numerical models of several configurations. As both the optimisation and modelling were time consuming procedures, the configurations were not tested experimentally.

2. Theory

The focus on wood as a structural material has increased in recent years. As a result, new types of wooden structures are emerging. An example is tall buildings, such as "Treet" in Bergen, Norway and CF Møller´s proposals for a new wooden skyscraper in Stockholm, Sweden. This can result in higher utilisation of wooden material and need for new structural principles such as rigid joints.

In this chapter, an overview of previous work and results will be given. Specially, the work done with threaded rods in moment resisting joints. The main objective is to give a presentation of various connections and their strengths and weaknesses.

2.1 Connections

According to *Handbook 1: Timber structure´s*, there are three main properties to consider when designing a joint. These are [3]:

- Load-carrying capacity
- Stiffness
- Ductility

Load-carrying capacity

The joint should have high effectiveness, given by the relation of the capacity of the timber members and the capacity of the joint. For timber-to-timber-connections the maximum factor of effectivity is considered to be $\eta \approx 0.60$ and $\eta \approx 0.50$ for theoretical and practical purposes respectively [3].

Stiffness

The stiffness of the joint influences the deformations of timber buildings and thus has to be considered in the serviceability limit state (SLS). Joints may be categorized into three different types depending on their stiffness [3]:

1. "Very stiff" joints with brittle failure modes - $\eta \approx 1.0$:
   The ultimate load is limited by the mechanical properties of the members. Example: Finger-joints.

2. "Stiff" connections - $\eta \approx 0.6 - 0.8$:
   Plastic load-carrying behaviour is desirable. Examples: Shear plates, punched metal plates, glued-in rods and axially loaded rods.
3. "Flexible" connections - $\eta < 0.6$:
   Tolerates intentioned movements of supports etc. Examples: "Slender" dowels and bolts, laterally loaded wood screws and nails.

Ductility

In general, timber is characterised by brittle mechanical behaviour which is not desirable for structural applications. A remedy may be to design the joint with sufficient deformability resulting in an overall acceptable ductility.

Other technical requirements

- Dynamical behavior:
  If a joint is subjected to dynamical loading, fatigue has to be considered.
- Fire resistance:
  Joints may strongly influence the overall fire resistance of a structure. While timber possesses relatively favourable properties in the case of fire, unprotected steel components do not.

2.2 Components in a connection

A corner joint in timber structures consists of several components. The main parts are the beam and column that are joined together. Additionally there are usually several smaller components which functions as fasteners between the timber parts.

2.2.1 Wood as a structural material

Wood is an organic material with a complex structure. The majority of this complexity may be attributed to the the grains which are orientated along the longitudinal axis. Due to the grains, wood may be characterised as an orthotropic material with different properties in the longitudinal, radial and tangential direction [3], which can be seen in Figure 2.1. The highest capacities are along the longitudinal direction and for structural applications it is consequently desirable to transfer the majority of the forces along this axis.

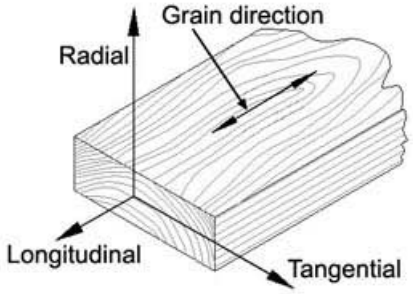

Figure 2.1: Orientation of directions in timber [4].

Glued-laminated timber

Glued-laminated timber (abbriv. glulam) is produced by gluing thin wood lamellas together on their wide faces to produce members with sizes limited only by the production facilities and transport considerations [5]. This may be favourable compared to ordinary solid wooden beams, because glulam beams can be produced with any rectangular cross-section. Mainly softwoods, such as spruce, are used, since the use of hardwood is often associated with difficulties in gluing.

Properties of glued-laminated timber

Strength and stiffness
Glulam has higher mean strength than solid timber, due to the smaller variability in strength and stiffness [5]. Strength reducing defects, such as growth defects, are either removed during the production process or more uniformly distributed in the finished product. With glulam the risk of local defects is reduced and defects has less importance compared to solid timber.

Moisture
When produced, the moisture content in glulam wood is about 12 % [5]. Glulam is regarded as more moisture stable than solid timber, as it is delivered dry and changes slower due to the large dimensions. The moisture content in timber, including glulam, should not exceed 20 to 22%, because uptake of moisture may lead to internal stresses and attack of fungi [5]. Extended high moisture exposure of the structural wood may lead to irreversible dimensional changes [5].

Density
The density of ordinary glulam (GL20-32) is about 390 - 440 kg/m^3, for GL30 the density is in the range of 430 kg/m^3 [5].

Table 2.1: Properties of different glulam strength classes [6].

Property [MPa]	**Symbol**	**GL24c**	**GL26c**	**GL28c**	**GL30c**	**GL32c**
Bending strength	$f_{m.g.k}$	24	26	28	30	32
Tensile strength	$f_{t.0.g.k}$	17	19	19.5	19.5	19.5
	$f_{t.90.g.k}$			0.5		
Compression strength	$f_{c.0.g.k}$	21.5	23.5	24	24.5	24.5
	$f_{c.90.g.k}$			2.5		
Shear strength	$f_{v.g.k}$			3.5		
Young's modulus	$E_{0.g.mean}$	11000	12000	12500	13000	13500
	$E_{90.g.mean}$			300		
Shear modulus	$G_{g.mean}$			650		
Rolling shear modulus	$G_{r.g.mean}$			65		
Density [kg/m^3]	$\rho_{g.mean}$	400	420	420	430	440

2.2.2 Fasteners

There are several methods of joining timber members. The most common are made of steel and includes dowels, screws, nails and plates [3].

For plane frames with similar thickness of the horizontal and vertical components, the fastener may be loaded either laterally or axially. Laterally loaded fasteners may exhibit low initial stiffness due to gaps between the fastener and the surrounding wood. In addition, they may induce tensile stresses perpendicular to the grains when subjected to moment action [7].

Threaded rods

A more desirable type of connection in joints exposed to large moments are therefore axially loaded fasteners, primarily threaded rods. These may be regarded as "reinforcement bars" as they transfer stresses across cracks and contribute to the overall structural integrity [7]. The performance of these rods is largely dependent on two properties; the angle between the rod and direction of the grain, and the embedment length. There is an approximate linear relation between the embedment length and withdrawal capacity, while the withdrawal stiffness is greatest for small angles and larger embedment lengths [7]. These properties will be elucidated in section 2.4.

2.3 Rigid joints in timber structures

The increased use of wood as a structural material, leads to new requirements for structural principles. Open and flexible architecture requires building systems without closely spaced columns or walls. To solve this issue, the rotational stiffness may be increased to fulfil lateral displacement requirements and/or withstand moment loading.

For a medium-rise building with long spans and without shear-walls or X-bracing, the serviceability requirement may be the governing factor in design. An article authored by H. Stamatopoulos [7], shows that a medium-rise building with a total height of 30 m, requires a stiffness of 10 000-11 000 kN m/rad to fulfil a serviceability of $\delta_H \leq \frac{H}{300}$. There are several alternatives to produce a rigid joint, such as axially loaded fasteners like glued-in rods and screwed-in threaded rods. Gluing may be cumbersome if it has to take place at site. To overcome this problem, intermediate steel parts as fasteners are used. These fasteners are usually vulnerable to fire and have to be properly covered. A new and better structural principle is therefore preferred.

2.3.1 Beam-to-column connections

A beam-to-column connection may be divided into two zones. By subjecting the beam to a vertical force acting downwards, tensile forces arise in the upper part of the connection, while the lower part is subjected to compression forces, as illustrated in Figure 2.2. Long, threaded rods may be used to transfer these forces between the timber components. Due to the load applied to the beam, a combination of axial and lateral forces will develop in these rods.

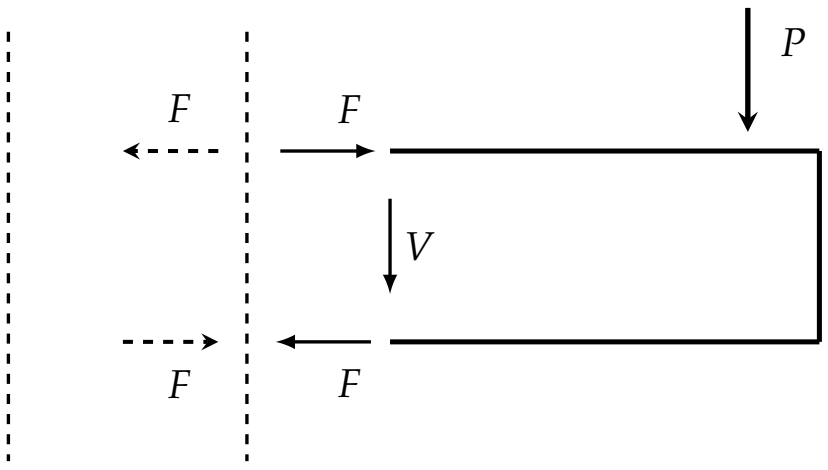

Figure 2.2: Tensile and compression forces in a beam-column connection

The properties of the threaded rods are largely dependent on the angle between the longitudinal axis of the rods and the grain direction [7]. In a beam-to-column connection, the grain direction in the column is perpendicular to the grain direction in the beam. Installing the rods with an inclination may lead to a better utilisation of the rods due to the combination of the different rod-to-grain angles in the column and in the beam.

In moment resisting frames, inclined threaded rods have proved to be one of the better methods of designing rigid corner joints, since they are continuous and thus do not have to be coupled at the intersection. Consequently, the problem of low initial stiffness due to gaps are generally avoided [7].

2.4 State of the art

This section provides an overview of the previous research done on both axially loaded threaded rods and moment resisting connections. The main focus are the withdrawal properties of long, threaded rods and moment resisting connections, utilising axially loaded fasteners.

2.4.1 Westerheim: *"Conceptual study of connections using glulam and long threaded bars exposed to fire loading"*

Six experiments were performed in 2013 to examine the capacity and fire resistance of glulam connections using long threaded rods [8]. The design is shown in Figure 2.3 with two rods in the upper part of the connection and one in the lower part. The two upper rods were installed with an inclination of 15 degrees with respect to the direction of the grain in the beam and with a length of 1004 mm. The inclination of the lower rod was 45 degrees with a length of 748 mm. Two variants of the connection were produced with edge spacing of 59 mm and 43 mm respectively.

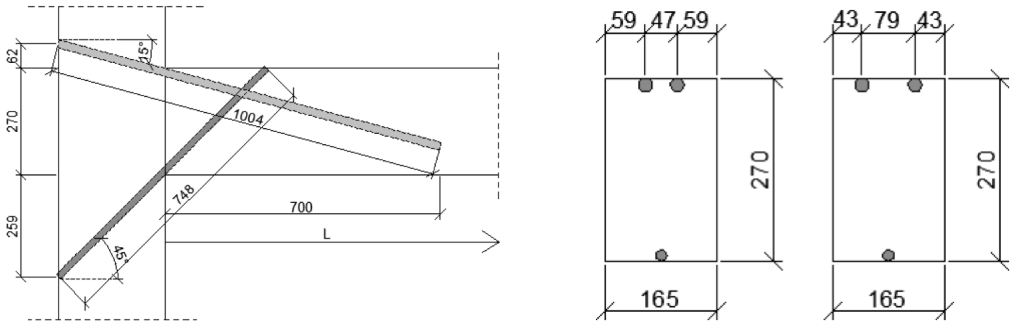

Figure 2.3: Rod placement and edge spacing for the two variants [8].

The capacity of all the connections was in the range of 40-54 kN. The tests with the smallest edge distances were able to resist the highest loading. The failure mode was a combination of withdrawal and transverse loading of the rods. Both connections showed a satisfying fire resistance above 60 minutes.

2.4.2 Stamatopoulos: *"Withdrawal Properties of Threaded Rods Embedded in Glued-Laminated Timber Elements"*

Eurocode 5 does not provide rules for estimations of withdrawal stiffness for axially loaded fasteners, nor capacity calculations for rods with an outer diameter larger than

12 mm or an inclination larger than 30 degrees relative to the grains. This Ph.D-thesis investigated the withdrawal properties of axially loaded threaded rods by use of analytical, numerical and experimental methods [9]. The main parameters were embedment length and rod-to-grain angle. The threaded rods had an outer diameter of 20 mm and were embedded in glulam elements of class L40c (corresponds to GL30c).

Malo & Stamatopoulos:
"Withdrawal stiffness of threaded rods embedded in timber elements"

Analytical estimations of withdrawal stiffness based on Volkersen's theory and numerical simulations were compared with experimental results [10]. Both theoretical approaches were in general in good agreement with the experimental testing. There were however some small discrepancies between the numerical and experimental results for short embedment lengths and small rod-to-grain angles.

As seen in Figure 2.4 the withdrawal stiffness is inversely proportional to the rod-to-grain angle. There is also an approximately linear relation between the withdrawal stiffness and embedment length up to ~300 mm. For greater lengths there is only a small increase in stiffness.

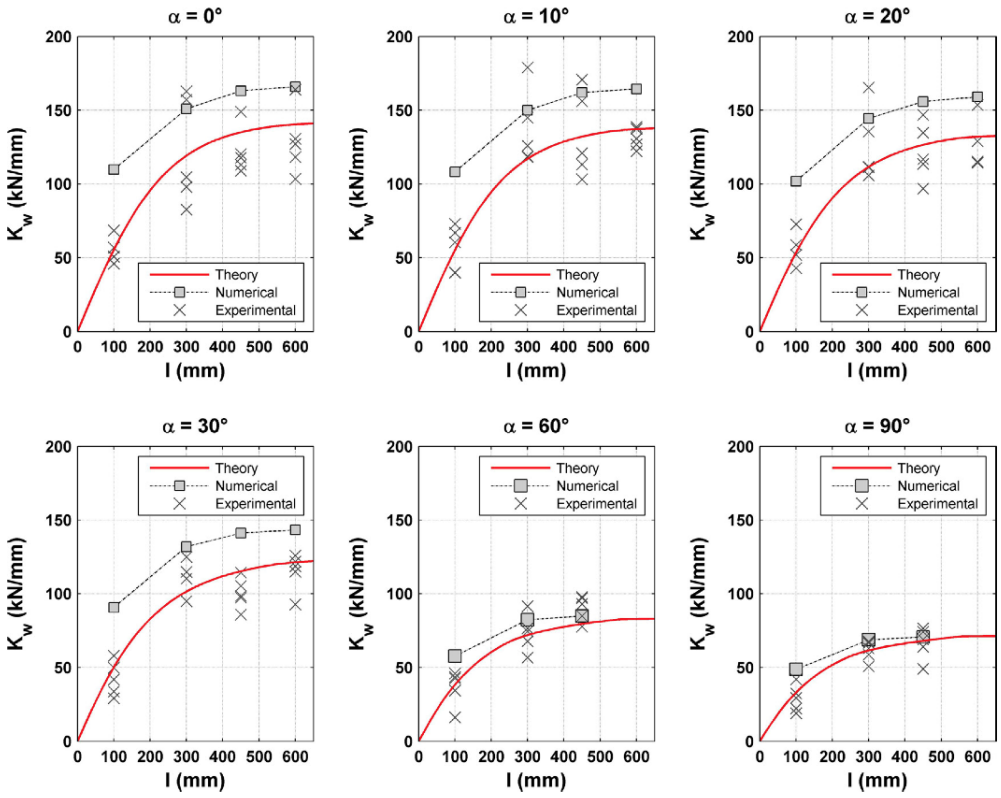

Figure 2.4: Withdrawal stiffness as a function of embedment length [10]-

Malo & Stamatopoulos:
"Withdrawal capacity of threaded rods embedded in timber elements"

A similar study was conducted with a focus on withdrawal capacity. The experimental results and theoretical estimations were found to be in good agreement [11].

As seen in Figure 2.5 the withdrawal capacity is nearly linearly proportional to the embedment length. Some of the concluding remarks were that small rod-to-grain angles led to a more brittle behaviour than larger angles, and that large embedment lengths may induce steel yielding. Lengths of 600 mm and more will lead to ductile steel failure rather than withdrawal failure.

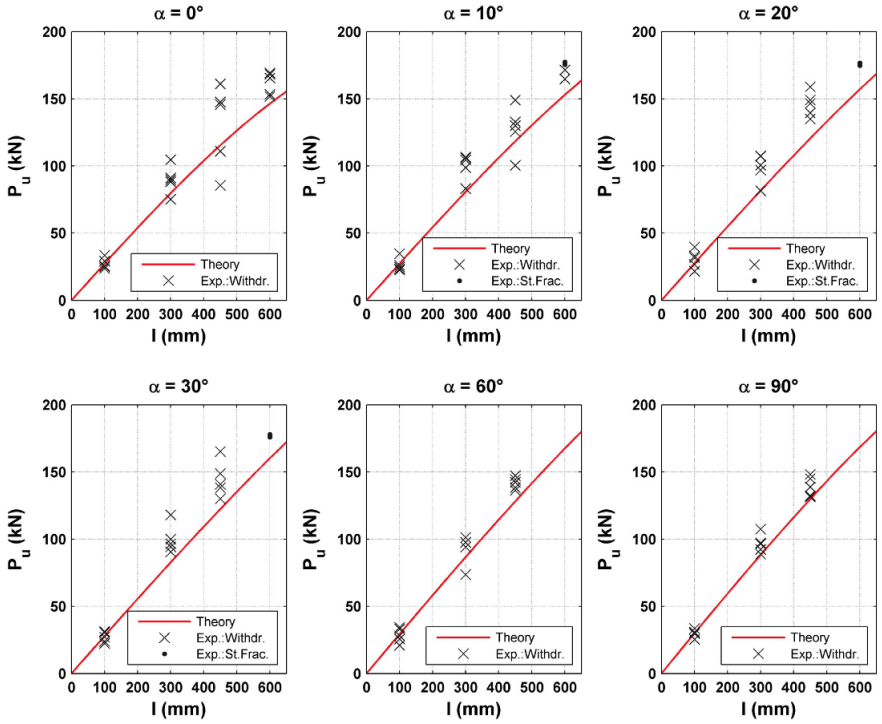

Figure 2.5: Experimental and theoretical capacities as a function of embedment length [11].

Malo & Stamatopoulos:
"Withdrawal of pairs of threaded rods with small edge distances and spacings"

This paper investigated withdrawal of pairs of screwed-in threaded rods with varying angles between the rod axis and the grain direction [12]. Two different configurations were tested, one with small edge distances and the other with small spacing between the rods. The distances were in both configurations smaller than the minimum requirements according to Eurocode 5, as shown in Figure 2.6. The threaded rods were embedded in a row perpendicular to the plane of the grain.

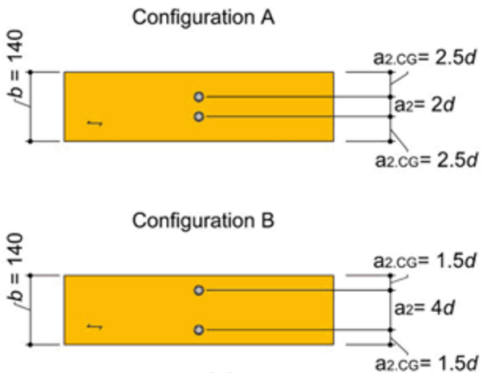

Figure 2.6: Edge distances and spacings [12].

By comparing the experimental results to the withdrawal capacity of single rods, the effective number, n_{ef}, was found to be in the range 1.72-1.94, see Figure 2.7c. An analytical expression was derived for estimating n_{ef}. The experimental results were compared to an analytical model based on Volkersen's theory and numerical simulations. Both estimations were in good agreement with the experimental results, as indicated in Figure 2.7a. The difference between the results for the two configurations was small.

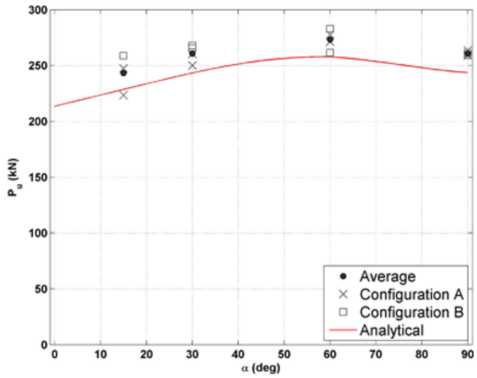

(a) Withdrawal capacity as a function of α

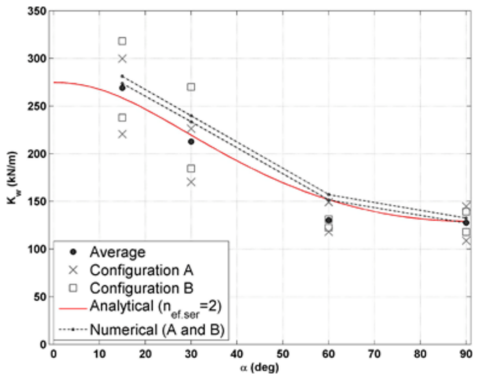

(b) Withdrawal stiffness as a function of α

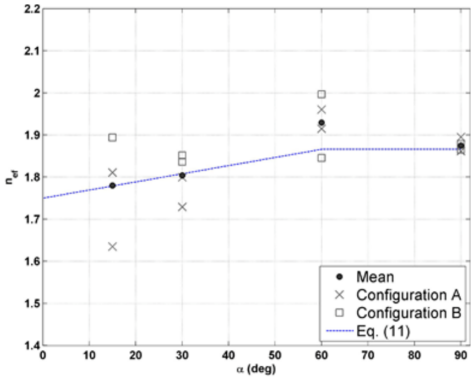

(c) n_{ef} as a function of α

Figure 2.7: Results from experimental testing compared to analytical estimates [12].

2.4.3 Grytting & Sæle: *"Axial and Lateral Loaded Threaded Rods in Timber Structures"*

A report investigating the behaviour of long threaded rods subjected to both lateral and axial loading was performed in 2015 [13]. The connections were evaluated analytically, numerically and experimentally. Twelve tests were carried out with different inclinations between the rod and the direction of the grain. For 45 degrees and 90 degrees, one test was performed, whereas the results for 60 degrees and 75 degrees were based on the mean values from five experiments. The load direction was perpendicular to the grains for all tests, as illustrated in Figure 2.8.

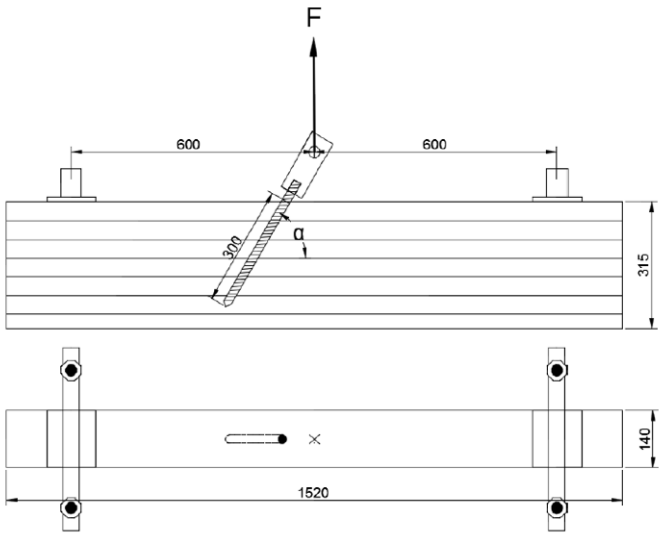

Figure 2.8: Illustration of the experimental set-up [13].

The experimental data showed a reduction in load capacity with increasing lateral loading, as seen in Table 2.2. The failure mode for all test was withdrawal of the threaded rod due to failure of the timber threads.

Table 2.2: Results from the experimental testing [13].

Inclination [°]	Capacity [kN]
45	49
60	64
75	85
90	88

Numerical simulations were performed with satisfying results. By the use of Hill's yield criterion it was possible to simulate failure of the timber threads in accordance with the experimental tests. Crack initiation and propagation were applied through

the Extended Finite Element Method (abbriv. XFEM). The cracks were modelled with Linear Elastic Fracture Mechanics and Virtual Crack Closure Technique and correlated well with the observations made during the experimental testing.

2.4.4 Veium: *"Axially Loaded Threaded Rods in Glulam Connections"*

In 2016, experiments were performed on a moment-resisting beam-to-beam connection [14]. The two glulam members were joined together using threaded rods and circular steel profiles, before being subjected to loading. Bending capacity and stiffness were measured. The threaded rods were screwed in with a 5 degree inclination relative to the grains. Various connections were tested with differing effective lengths and number of rods. An effective length of 1200 mm was necessary to avoid withdrawal.

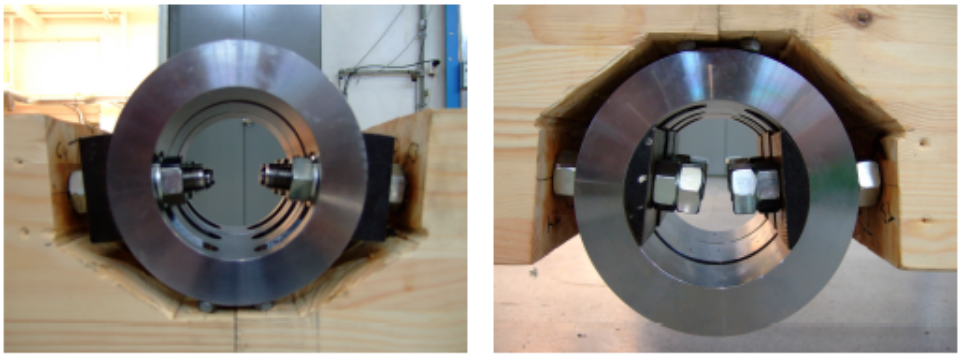

Figure 2.9: Circular steel profiles in compression zone (left) and tensile zone (right) [14]

The tests with two pairs of rods resulted in failure due to rods in tension and a maximum capacity of 58 % of the capacity of the beam. By increasing the number of rods to three pairs, the percentage increased to 82 % of the beam capacity. The failure then occurred in the wood resulting in large deformations and the desired ductility in the connection was obtained. Complete experimental results are presented in Table 2.3.

Table 2.3: Results from experimental testing [14].

Test no.	1	1b	2	3	4
Date	27.05	30.05	03.06	01.06	07.06
Failure component	Nut	Steel rod	Steel rod	Timber	Withdrawal
Moment:					
Experimental $[kNm]$	156.6	164.9	168.2	236.6	225.3
Theoretical $[kNm]$	142.1	142.1	142.1	216.1	216.1
% of theoretical	110	116	118	109	104
% of beam capacity	54	57	58	82	78
Stiffness: $[\frac{kNm}{rad}]$					
Theoretical , $S_{j,ini}$	16 681	16 681	16 655	25 293	25 223
S_j in 1. loading phase	13 745	12 288	22 981	25 346	31 582
S_j in relief phase	18 269	16 005	25 036	30 772	38 566
S_j in 2. loading phase	17 905	15 949	24 575	30 469	38 197
Observed shear crack	Yes	Yes[1]	No	No	No

[1]Shear crack occurred in test number 1

2.4.5 Lied & Nordal: *"A Conceptual Study of Glulam Connections Using Threaded Rods and Connecting Circular Steel Profiles"*

In the autumn of 2016, the circular steel profiles from the work of Veium were used in a beam-to-column connection [2]. The main focus was to develop a connection with moment resisting properties. Numerical simulations were used to optimise the design of the circular steel profiles and to find the most favourable rod-to-grain angle combination. The rotational stiffness was also estimated both numerically and analytically by use of a component method model.

Three different connections were produced with varying rod-to-grain angles and embedment lengths. Two of them are illustrated in Figure 2.10. Additionally, it was produced two identical connections with circular profiles in the upper part and an inclined rod in the lower part making the total number of tests four. The connections were subjected to a point load applied to the beam surface with a moment arm of 2 metres. Displacements and rotations were measured. The experimental results and a comparison with theoretical estimations can be found in Table 2.4.

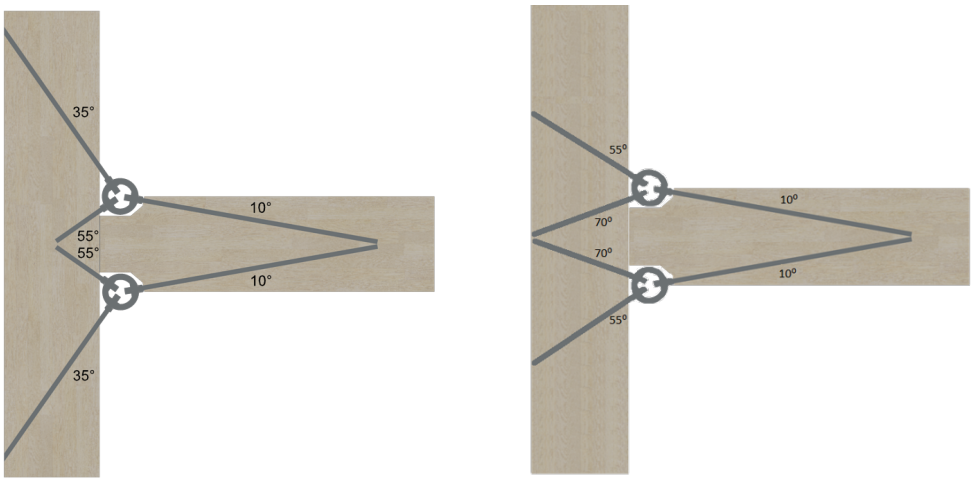

(a) Test 3 (b) Test 4

Figure 2.10: The two configurations with circular profiles.

Table 2.4: Comparison between theoretical and experimental results [2].

Test no.	1	2	3	4
Moment:				
Experimental $[kNm]$	105.3	104.3	78.8	133.3
Theoretical $[kNm]$	163.4	163.4	163.4	163.4
% of theoretical	64	64	48	82
Stiffness: $[\frac{kNm}{rad}]$				
Initial contact interaction	Yes	Yes	No	Yes
Theoretical, Abaqus model	2667	2667	2130	-
Theoretical, Component method	2132	2132	11398	15225
Experimental	6571	7137	9079	7603

The theoretical stiffness obtained from the Abaqus/CAE model were a lot lower than the results from the experimental testing. This was mainly contributed to the spring elements connecting directly to single points, resulting in local displacements in these points. The component method gave satisfying results for test 3, but not for the other tests. The assumptions made when defining the withdrawal stiffness of the rods was suggested as a possible explanation.

The rotational stiffness was greatest for test 3, but it also possessed the lowest moment capacity. This was contributed to withdrawal of the lower rod in the tensile part of the connection due to short embedment length. Test 4 exhibited both high stiffness and large capacity, making this configuration the most promising as a moment resisting connection.

2.5 Summary

The results obtained by Lied & Nordal [2] indicate great potential regarding the use of threaded rods and connecting circular steel profiles in moment resisting joints. One of the most important parameters in connections using threaded rods embedded in timber is the angle between the rod axis and direction of the grain. Although both withdrawal capacity and stiffness of threaded rods embedded in timber with varying inclinations are thoroughly elucidated by Malo & Stamatopoulos [10–12], there is still uncertainty regarding interaction between several rods embedded in the same timber element with different angles. The previously mentioned work indicate that a smaller angle relative to the grain results in the highest stiffness and that a length of approximately $20d_{inner}$ is sufficient to achieve maximum withdrawal stiffness for a given inclination.

The work by Veium [14] and Lied & Nordal [2] proved that the connecting circular steel profiles perform well in connections where high stiffness is a priority. Both manufacturing and mounting are relatively uncomplicated, and they can be used for a wide range of angles. They do however occupy a fairly large space, and did not yield as the connection reached maximum capacity making the failure mode brittle.

Westerheim [8] and Malo & Stamatopoulos [12] observed that the requirements for minimum edge distances and spacing, given in Eurocode 5, are too conservative for rods with diameter larger than 12 mm. A configuration with edge distances of $1.5d$ and another with spacing of $2d$ gave capacities close to that of a single rod with large distances.

3. Connection

The main objective of this chapter is to continue the work done by Lied & Nordal [2], and try to optimise both the inclination relative to the grains and further develop the steel connection between the rods. Optimisation of the rod-to-grain angle will hopefully increase the stiffness of the connection, and fulfil the requirements established by WoodSols [1]. Further development of the steel connector will be investigated, and a new design will be proposed.

3.1 Optimization of rod configuration

According to the theory described in section 2.4, both the rod-to-grain angle and embedment length are of major importance when considering the stiffness of threaded rods embedded in timber. The establishment of a favourable combination of rod-to-grain angles with sufficient embedment lengths are crucial in order to design a connection with moment resisting properties.

There are several methods of investigating the behaviour of various rod configurations. Analytical estimations may be the most inaccurate, but can be beneficial as they are often faster than numerical modelling and may thus give an indication as to which configurations may be worth investigating further. Numerical models are usually more accurate, but without validation by experimental testing, the results have to be used with caution.

In this section the configuration of rods will be optimised through analytical calculations. The forces in each rod due to the applied loading will be considered and a calculation model for threaded rods embedded in timber, developed by Postdoctoral Fellow Haris Stamatopoulos, will be presented. The results will be used to determine which configurations that may possess high rotational stiffness and these will be further investigated through numerical simulations.

Configuration considerations

The connection is designed to be part of moment resisting frames. Although the self-weight of slabs etc. and imposed loads will normally lead to a tension zone in the upper part of the connection and a compression zone in the lower part. Natural induced forces, like wind load, may alter these zones. When the frame is subjected to lateral loading, the beam will be pushed down due to the rigid joint. Consequently,

on the opposite side of the frame, the beam will push the joint up and outwards, as illustrated in Figure 3.1.

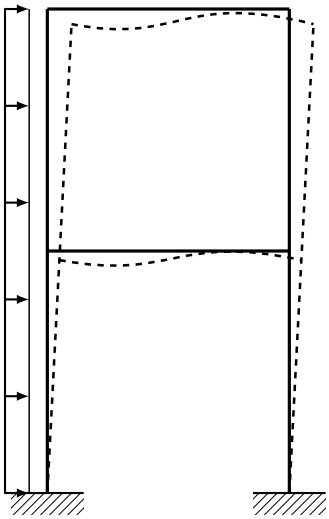

Figure 3.1: Moment resisting frame subjected to lateral loading.

Thus, a symmetrical connection about the centre line along the longitudinal axis of the beam is desirable as the lateral loading may be applied from either side.

Labelling of configurations and rods

The labelling system used in this thesis for the various configurations refers to the angle between the rod and the grain direction. By considering the upper part of the connection with the beam on the right-hand side, the first number refers to the lower column rod and proceeds clockwise ending with the beam rod. The result is that Test 4 by Lied & Nordal, described in section 2.4, is labelled 70-55-10. The system is illustrated in Figure 3.2.

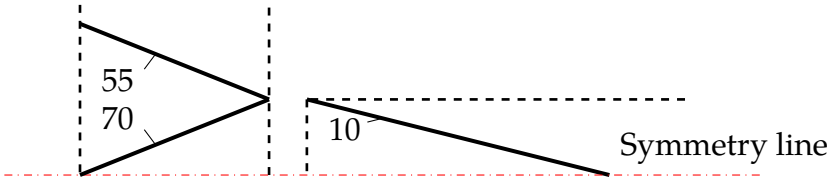

Figure 3.2: Labelling of the different configurations.

The connection consists of several rods which will be referred to throughout this thesis. These rods are labelled according to where they are located, both regarding timber component and tension/compression zone. The rods in the beam and the column are labelled with a B or C respectively, in addition to a U or L referring to either the upper or the lower part of the connection respectively. As there are two rods in both zones in the column, it is necessary to label the inner rods, i.e. the first

number in the configuration label, with the number 1 and the outer rods with 2. All the rods with their respective labels are illustrated in Figure 3.3.

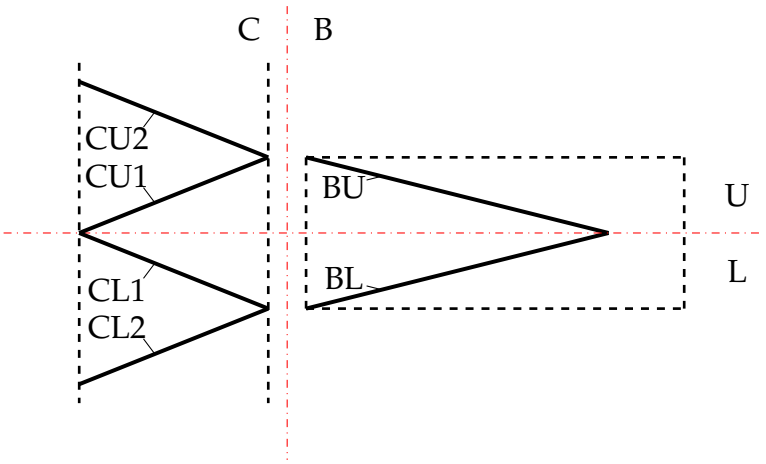

Figure 3.3: Labelling of rods in the different configurations.

3.1.1 Force distribution

To determine the optimal combination of rod-to-grain angles it was necessary to find a configuration where each rod contribute equally. If one rod was to be pulled out long before the others, the entire connection would loose both stiffness and capacity.

In order to calculate the axial forces in the two rods in the column, a simplified MatLab-script was written based on decomposition of forces. The principle is illustrated in Figure 3.4. The input parameters are the angle between the longitudinal axis of the rod and the grain direction, and the point load. By keeping the point load fixed and only vary the inclinations of the rods, the script will present the axial force in each rod for different configurations.

Enforcing force equilibrium in both Cartesian directions in Figure 3.4 will yield the following two equations:

$$F_x = F_{ax.1} \sin \alpha_{c1} + F_{ax2} \sin \alpha_{c2} \tag{3.1}$$

$$F_y = F_{ax.1} \cos \alpha_{c1} - F_{ax2} \cos \alpha_{c2} \tag{3.2}$$

F_x and F_y are the horizontal and vertical forces resulting from the applied point load, P, through the following relations:

$$F_x = \frac{PL}{z} \tag{3.3}$$

$$F_y = \frac{P}{2} \tag{3.4}$$

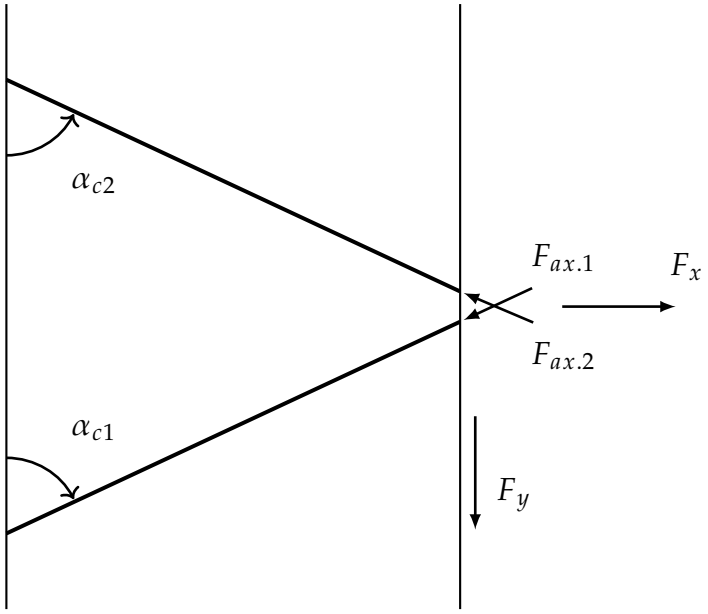

Figure 3.4: Decomposition of forces.

where L is the horizontal distance between the column face and the load, and z is the vertical moment arm between the two horizontal forces due to the moment action.

The two equilibrium equations may be written on matrix form:

$$\begin{bmatrix} F_x \\ F_y \end{bmatrix} = \begin{bmatrix} \sin\alpha_{c1} & \sin\alpha_{c2} \\ \cos\alpha_{c1} & -\cos\alpha_{c2} \end{bmatrix} \begin{bmatrix} F_{ax.1} \\ F_{ax.2} \end{bmatrix} \tag{3.5}$$

By rearranging the matrices, expressions for the axial force in each rod may be formulated:

$$\begin{bmatrix} F_{ax.1} \\ F_{ax.2} \end{bmatrix} = \frac{1}{\sin\alpha_{c1} \cdot \cos\alpha_{c2} + \cos\alpha_{c1} \cdot \sin\alpha_{c2}} \begin{bmatrix} \cos\alpha_{c2} & \sin\alpha_{c2} \\ \cos\alpha_{c1} & -\sin\alpha_{c1} \end{bmatrix} \begin{bmatrix} F_x \\ F_y \end{bmatrix} \tag{3.6}$$

Table 3.1 is an overview of a selection of rod-to-grain angles and the resulting axial forces due to the applied point load. The input parameters were defined as $P = 10\,\text{kN}$, $L = 2000\,\text{mm}$ and $z = 450\,\text{mm}$, resulting in:

$$F_x = \frac{PL}{z} = 44.44\,\text{kN} \tag{3.7}$$

$$F_y = \frac{P}{2} = 5\,\text{kN} \tag{3.8}$$

Table 3.1: Distribution of forces.

Rod no.	Angle [°]	Axial forces [kN]
CU1	55	33.54
CU2	35	29.59
CU1	70	26.12
CU2	55	24.29
CU1	70	16.34
CU2	70	30.96
CU1	75	18.31
CU2	70	28.48
CU1	45	27.89
CU2	45	34.96

Due to the shear force, a smaller angle for rod CU2 than CU1 results in a more even distribution. A combination of 70 and 55 degrees, corresponding to Test 4 performed by Lied & Nordal [2], yields the most even distribution and the lowest maximum force. Equal inclinations results in a more unbalanced distribution and a higher maximum force. For larger angles however, the longitudinal axis of the rods will be more aligned with the horizontal force component. This is desirable when considering its magnitude compared to the vertical force component.

The evaluation of the force distribution in the column rods validate the favourable combination of inclinations in the tests performed by Lied & Nordal [2]. It also indicate that larger, and maybe even equal angles, may be worth investigating further, even though the maximum axial force increased slightly and the distribution was not as balanced.

3.1.2 Component method

An analytical approach to determine the rotational stiffness of a joint was developed by Postdoctoral Fellow Haris Stamatopoulos. The calculation model is a combination of the component method and matrix structural analysis, where the joint is divided into several components which contributes to the overall stiffness individually.

In this calculation model, the two upper column rods are defined as one component, and the beam rod as a second one. Due to symmetry, the same components are found in the lower part of the connection. The direct stiffness method is applied to divide each component, which may be considered as a system, into subsystems consisting of elements. The rods are divided into two elements, the part embedded in timber and the free part. By the use of force-displacement-relations, the axial and lateral stiffness of each element can be calculated. As these values are known, the stiffness of the column and beam may be estimated. These can be combined through the component method, as described in Eurocode 3, to find the rotational stiffness of the entire connection.

Element stiffness

Withdrawal stiffness

Estimation of the stiffness of an axially loaded connector is based on the classical Volkersen's theory [15]. The concept imply that all shear deformation takes place in an infinitely thin shear layer, while the connector and surrounding wood are in states of pure axial and uniform stress. Depending on the supports different loading conditions may be assumed. In this context, the relevant conditions are pull-shear or pull-pull. These are quite similar, but for the latter it is necessary to determine the effective area of the wood. In complicated loading conditions, this is difficult. Thus, a pull-shear condition is assumed with the withdrawal stiffness determined by the following equation:

$$K_w = \frac{P}{\delta_w} = \pi \cdot d \cdot l_{ef} \cdot \Gamma_{e.\alpha} \cdot \frac{\tanh \omega}{\omega} \tag{3.9}$$

Where d is the outer thread diameter of the rod and l_{ef} is the embedment length. The parameter ω is defined as:

$$\omega = \sqrt{\pi \cdot d_{e.\alpha} \cdot \beta \cdot l_{ef}^2} \tag{3.10}$$

where

$$\beta = \frac{1}{E_s \cdot A_s} + \frac{1}{E_{w.\alpha} \cdot A_w} \tag{3.11}$$

In a pull-shear loading condition the wood is assumed to be in a state of pure shear resulting in $A_w \rightarrow \infty$ and thus $\beta = \frac{1}{A_s \cdot E_s}$.

The parameter Γ_e is the equivalent shear stiffness of the shear zone and the slope of the first linear part of the bi-linear constitutive law of the $\tau - \delta$-curve. The expression is a function of the rod-to-grain angle α and is given by [10]:

$$\Gamma_{e.\alpha} = \frac{9.35}{1.5 \cdot \sin^{2.2}\alpha + \cos^{2.2}\alpha} \tag{3.12}$$

Axial stiffness of the free part

The axial stiffness of the free part of the rod is evaluated based on the axial stiffness of a solid bar in tension, as illustrated in Figure 3.5.

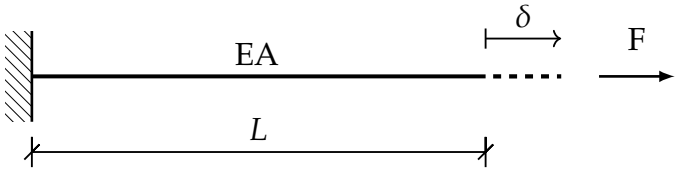

Figure 3.5: Axially loaded bar.

$$\delta = \frac{FL}{EA} \tag{3.13}$$

$$K = \frac{F}{\delta} = \frac{EA}{L} \tag{3.14}$$

When evaluating the connection the following notation will be applied:

$$K_{0.ax} = \frac{E_s A_s}{l_0} \tag{3.15}$$

Total axial stiffness

The total axial stiffness is calculated by combining the two contributions as equivalent springs in series:

$$K_{ax} = \frac{K_w \cdot K_{0.ax}}{K_w + K_{0.ax}} \tag{3.16}$$

Joint slip

The lateral stiffness of threaded rods embedded in timber can be estimated by use of formulas given in Eurocode 5. It will develop a slip between the connector and the surrounding timber when the connector is subjected to lateral load [13]. This slip modulus, K_{ser}, is calculated through varying formulas given in EC5 dependent on the type of mechanical fastener [16]. The resulting value is valid for one shear plane and one fastener in SLS. The formula has relatively few variables, with only the density of timber and the diameter of the fastener as parameters. For screws the formula is:

$$K_{ser} = \frac{\rho_m^{1.5} \cdot d_{eff}}{23} \tag{3.17}$$

where ρ_m is the mean density of timber and d_{eff} is the outer thread diameter.

Lateral stiffness of the free part

The lateral stiffness of the free part is evaluated from the expression for the bending stiffness of a cantilevered beam, as illustrated in Figure 3.6.

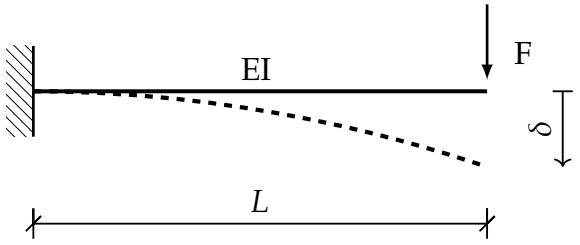

Figure 3.6: Laterally loaded cantilever.

$$\delta = \frac{FL^3}{3EI} \tag{3.18}$$

$$K = \frac{F}{\delta} = \frac{3EI}{L^3} \tag{3.19}$$

When evaluating the connection the following notation will be applied:

$$K_{0.lat} = \frac{3E_s I_s}{l_0^3} \tag{3.20}$$

Total lateral stiffness

The total lateral stiffness is calculated identical to the total axial stiffness by combining the two contributions as equivalent springs in series:

$$K_{lat} = \frac{K_{ser} \cdot K_{0.lat}}{K_{ser} + K_{0.lat}} \tag{3.21}$$

Component stiffness

Column

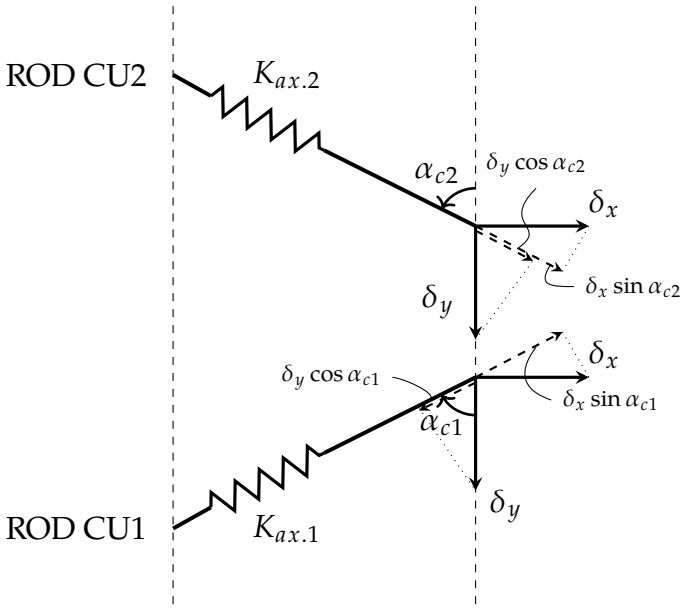

Figure 3.7: Element displacements in the column.

For the column component, the lateral stiffness contribution is assumed to be so small that it can be neglected to simplify calculations.

Substituting the relevant parameters for the column as described above into the system stiffness relation results in:

$$\begin{bmatrix} \delta_{ax.1} \\ \delta_{ax.2} \end{bmatrix} = \frac{1}{A} \begin{bmatrix} n_{12} \cdot c_2^2 + c_1^2 & n_{12} \cdot s_{12} \cdot c_2 - c_1 \cdot s_1 \\ n_{12} \cdot s_{12} \cdot c_2 - c_1 \cdot s_1 & n_{12} \cdot s_2^2 + s_1^2 \end{bmatrix} \begin{bmatrix} \frac{M}{z} \\ \frac{V}{2} \end{bmatrix} \tag{3.22}$$

where

$$n_{12} = \frac{K_{ax2}}{K_{ax1}} \tag{3.23}$$

$$A = n_{12} \cdot K_{ax1}(c_1 \cdot s_2 + c_2 \cdot s_1)^2 \tag{3.24}$$

$$L_v = \frac{M}{V} \tag{3.25}$$

An expression for the rotation of the column component can be established from Figure 3.8:

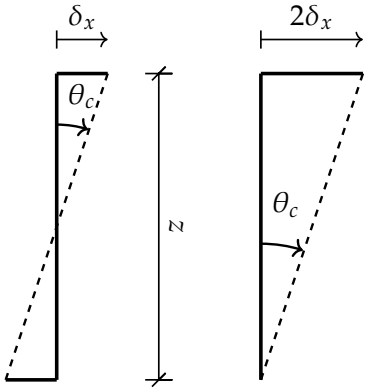

Figure 3.8: Illustration of the rotation-displacement relation.

$$\theta_c = \frac{2\delta_x}{z} \tag{3.26}$$

Inserting Equation 3.22 results in:

$$\theta_c = \frac{2M}{z^2 \cdot A}\left[(n_{12} \cdot c_2^2 + c_1^2) + \frac{n_{12} \cdot s_2 \cdot c_2 - c_1 \cdot s_1}{2L_v} \cdot z\right] \tag{3.27}$$

Having defined the rotation, an expression for the rotational stiffness of the column can be established:

$$K_{\theta_c} = \frac{M}{\theta_c} = \frac{z^2 \cdot A}{2}\left[n_{12} \cdot c_2^2 + c_1^2 + \frac{n_{12} \cdot s_2 \cdot c_2 - c_1 \cdot s_1}{2L_v} \cdot z\right]^{-1} \tag{3.28}$$

Beam

As there is only one rod, i.e. one subsystem in the beam component, the lateral forces can not be neglected. This is due to fact that with one rod and thus one load path, it would not be possible to satisfy the equilibrium equations in the x- and y-directions.

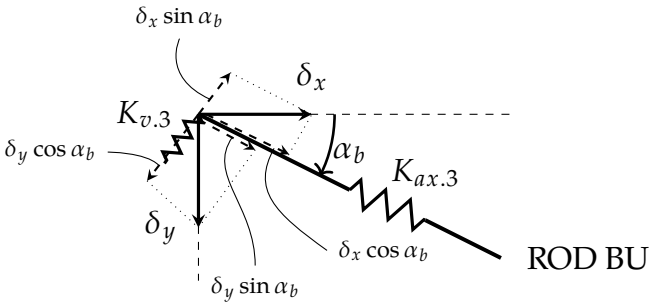

Figure 3.9: Element displacements in the beam.

Consequently, the system stiffness relation for the beam becomes:

$$\begin{bmatrix} \delta_x \\ \delta_y \end{bmatrix} = \frac{1}{n_v \cdot K_{ax.3}} \begin{bmatrix} n_v \cdot s_3^2 + c_3^2 & -c_3 \cdot s_3 \cdot (n_v - 1) \\ -c_3 \cdot s_3 \cdot (n_v - 1) & n_v \cdot s_3^2 + c_3^2 \end{bmatrix} \begin{bmatrix} \frac{M}{z} \\ \frac{V}{2} \end{bmatrix} \tag{3.29}$$

where

$$n_v = \frac{K_{v.3}}{K_{ax.3}} \tag{3.30}$$

By defining the rotation analogously with the column component:

$$\theta_b = \frac{2\delta_x}{z} \tag{3.31}$$

and inserting Equation 3.29 results in:

$$\theta_b = \frac{2M}{z^2 \cdot n_v \cdot K_{ax.3}} \left[(n_v \cdot s_3^2 + c_3^2) + \frac{c_3 \cdot s_3 \cdot (n_v - 1)}{2L_v} \cdot z \right] \tag{3.32}$$

Consequently, an expression for the rotational stiffness of the beam can be established:

$$K_{\theta_b} = \frac{M}{\theta_b} = \frac{z^2 \cdot n_v \cdot K_{ax.3}}{2} \left[(n_v \cdot s_3^2 + c_3^2) + \frac{c_3 \cdot s_3 \cdot (n_v - 1)}{2L_v} \cdot z \right]^{-1} \tag{3.33}$$

Rotational stiffness

Having defined the rotational stiffness of both the column component, K_{θ_c}, and the beam component, K_{θ_b} , the total rotational stiffness of the entire connection can be calculated by use of the expression for equivalent springs in series:

$$K_{\theta_{tot}} = \frac{K_{\theta_c} \cdot K_{\theta_b}}{K_{\theta_c} + K_{\theta_b}} \tag{3.34}$$

These formulas are used in a spreadsheet constructed by PhD Candidate Aivars Vilguts. The calculations are summarised in a graph which can be seen in Figure 3.10. The input data are based on the connection with the circular profile as done by Lied & Nordal [2].

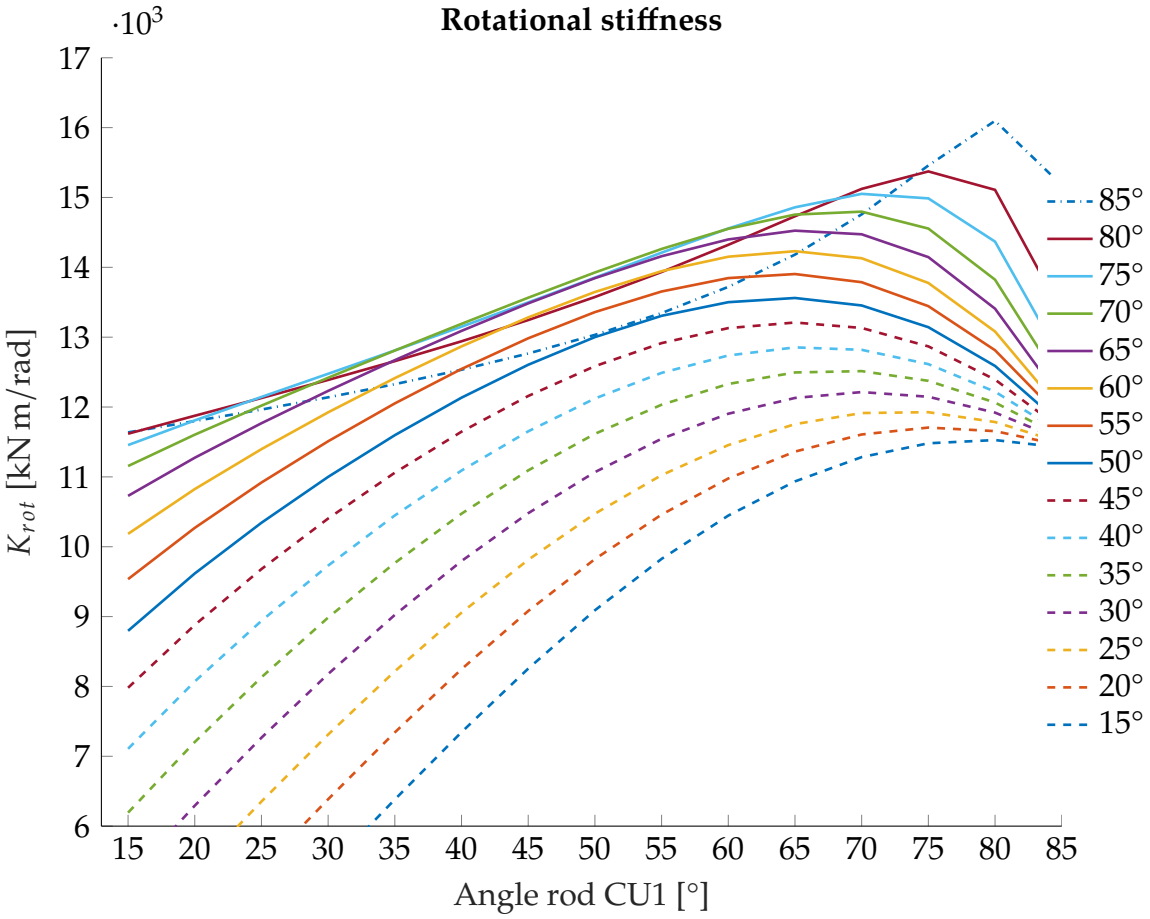

Figure 3.10: Rotational stiffness for varying angles of rod CU2 as a function of inclination of rod CU1. The inclination for rod BU in the beam is 10 degrees.

According to Figure 3.10 larger angles results in a higher rotational stiffness. This may be attributed to the horizontal force component resulting from the applied point load. By having a smaller rod-to-grain angle, the lateral loading increases. The consequence is that even though the withdrawal stiffness is greatest along the grains [10], it is not utilised due to the lateral force direction.

For all angles, the embedment length is larger than the required $20d_{inner}$, mentioned in section 2.5, giving maximum withdrawal stiffness for a given angle. Consequently, even though the embedment length is larger for smaller angles, this do not effect the total stiffness of the connection.

3.2 Withdrawal properties

The numerical modelling program used in this thesis, is Abaqus. Abaqus is a simulation program that enables the user to simulate complex models with the use of numerical solutions, as finite element analysis. To reduce the computational time, due to limited amount of computing capacity, simplification of the connection parts, like the threaded rods, is desirable.

3.2.1 Numerical modelling

In this thesis the use of linear static analysis will be applied. The fundamental requirements that a static problem must satisfy are:

- static equilibrium
- kinematic compatibility
- force-displacement

If the solution satisfies all three requirements, the solution is correct, and if the solution is linear, as in our case, the solution is unique [17]. The elastic change of work performed by the outer forces, R, over the corresponding displacements, r, can be written as [18]:

$$W = \frac{1}{2}\sum_i R_i r_i = \frac{1}{2}R^T r \tag{3.35}$$

The relation between R and r is defined by the kinematic compatibility:

$$R = Kr \quad \text{or} \quad r = K^{-1}R \tag{3.36}$$

Where K is defined as the global stiffness matrix, R the global force matrix and r the global displacement matrix. Whereas R and K are known parameters, r is the unknown parameter [17].

The relationship between global nodal displacement, r^i, and element nodal displacement, v^i, is defined with the kinematic compatibility matrix, $\mathbf{a}$ [17]:

$$v^i = (\mathbf{a}^i)r \tag{3.37}$$

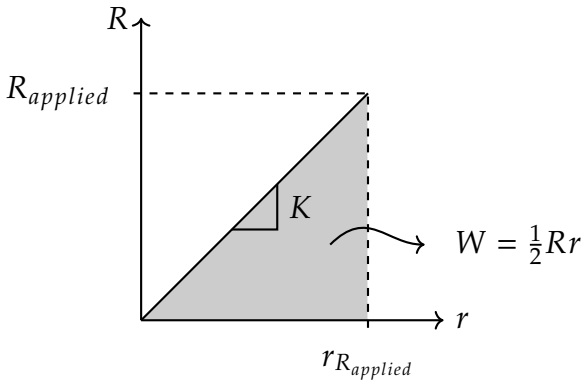

Figure 3.11: Visual relationship between applied load, R, and displacement, r.

The global stiffness, force and displacement matrices are established by adding together the contributions from each element in the model, and assembled by the compatibility matrix (a^i). The global stiffness matrix is defined by [17]:

$$K = \sum_{i=1}^{m} (\mathbf{a}^i)^T k^i (\mathbf{a}^i) \tag{3.38}$$

Were k^i is the local element stiffness matrix. The global force matrix defined by [17]:

$$R = \sum_{i=1}^{m} (\mathbf{a}^i) S^i \tag{3.39}$$

Where S^i is defined as the local nodal loads.

Element type

Modelling a representation of a beam-to-column connection, the use of solid elements is essential. In Abaqus Standard the robust eight-node element, C3D8, is widely used. This is a plane stress/strain solid element with representation of displacement in each direction x, y and z [19]. The relationship between nodal degrees of freedom, **{v}**, and displacement of a point **[u v w]** within the element is given by:

$$\mathbf{u} = [\mathbf{N}]\{\mathbf{v}\} \quad \text{where} \quad \{\mathbf{u}\} = [\mathbf{u\ v\ w}]^{\mathbf{T}} \text{ and } \{\mathbf{v}\} = [\mathbf{u_i\ v_i\ w_i}]^{\mathbf{T}} \tag{3.40}$$

Where **[N]** defines the shape function matrices. The requirement for each shape function N_i is to produce a unit value at node i and vanish at every other node [17]. For the eight-node element the shape function matrix is given by:

$$N = \begin{bmatrix} N_1 & 0 & 0 & N_2 & 0 & 0 & \dots & N_8 & 0 & 0 \\ 0 & N_1 & 0 & 0 & N_2 & 0 & \dots & 0 & N_8 & 0 \\ 0 & 0 & N_1 & 0 & 0 & N_2 & \dots & 0 & 0 & N_8 \end{bmatrix} \tag{3.41}$$

where

$$N_i = \frac{1}{8}(1 + \xi_i\xi)(1 + \eta_i\eta)(1 + \zeta_i\zeta) \quad \text{for} \quad i = 1, \dots, 8 \tag{3.42}$$

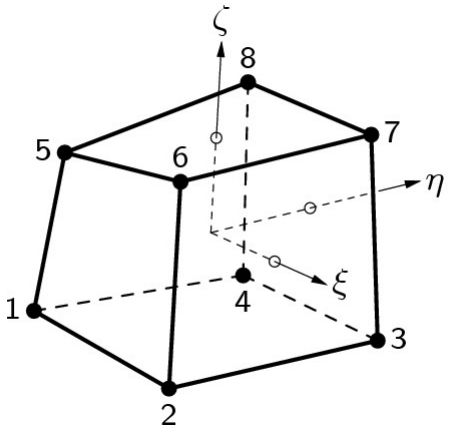

Figure 3.12: Eight-node hexahedron, also known as linear hexahedron.

The relationship between displacement and strain is given by $\{\varepsilon\} = [\partial][\mathbf{u}]$, hence:

$$\{\varepsilon\} = [\mathbf{B}]\{\mathbf{v}\} \quad \text{where} \quad [\mathbf{B}] = [\partial][\mathbf{N}] \tag{3.43}$$

From the principle of virtual work, where the virtual work performed by the real external forces over the virtual displacements (ũ and ṽ) is equal to the virtual work performed by the real internal stresses over the virtual strains ($\tilde{\varepsilon}$) [17]. These virtual strains ($\tilde{\varepsilon}$) is compatible with (ũ and ṽ). This gives $W_e = W_i$, that reads:

$$\tilde{v}^T S + \int \tilde{u}^T F \mathrm{d}V + \int \tilde{u}^T \mathbf{\Phi} \mathrm{d}S = \int \tilde{\varepsilon}^T \sigma \mathrm{d}V \tag{3.44}$$

Substituting for $\tilde{u}$, $\tilde{\varepsilon}$ and σ, and rearranging Equation 3.44 results in:

$$S = \int \mathbf{B}^T \mathbf{C}\mathbf{B} \mathrm{d}V - \int \mathbf{B}^T \mathbf{C} \varepsilon \mathrm{d}V - \int \mathbf{N}^T F \mathrm{d}V + \int \mathbf{N}^T \mathbf{\Phi} \mathrm{d}S = kv + S^0 \tag{3.45}$$

The stiffness matrix reads:

$$k = \int \mathbf{B}^T \mathbf{C}\mathbf{B} \mathrm{d}V \tag{3.46}$$

The eight-node solid element exhibit shear locking [17]. That is due to spurious shear strain, they are excessively stiff when asked to display the beam-bending mode. To avoid this problem the use of "under-integration" or "reduced-integration" is available in Abaqus Standard. Reduced integration of an element has a softening effect because some polynomial terms vanish at Gauss point of a low-order integration rule and therefore make no contribution to strain energy. The use of reduced integration also introduce the defect known as zero-energy deformation mode or hourglass mode [17].

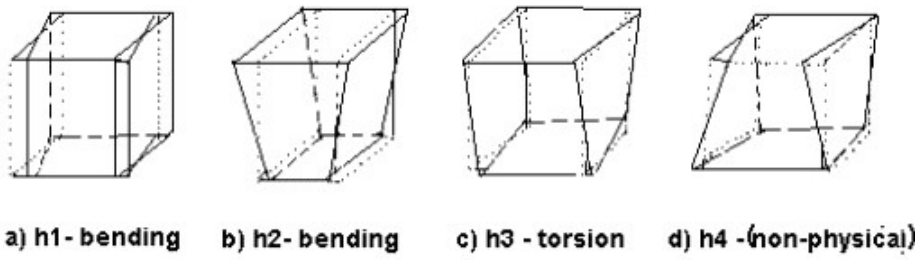

Figure 3.13: Spurious mode patterns

An element whose stiffness matrix incorporates a spurious mode has no resistance to nodal loads that tend to activate the mode. To reduce the effect of the hourglass mode, Abaqus introduce a hourglass control in each element [20]. The evaluation of the effect of hourglass mode can be studied by comparing the amount of "artificial energy" against total internal energy. The amount of artificial energy should not exceed 3% of total internal energy [21].

Cohesive zone

To reproduce the withdrawal of threaded rods, the use of cohesive zone in Abaqus may be applicable. The rod-wood interaction would then be idealised as a cylindrical interaction between steel and wood. Cohesive zone models have been proved useful in many different varieties of fracture issues in homogeneous solids.

A.A. Griffith developed a theory on energy-balance [22]. The energy criterion is based on the principle that crack extension can only occur when the energy available for crack growth is sufficient to overcome the resistance of the material. G.R Irwin defined the energy release rate, G, as the rate of change in potential energy with crack area for a linear elastic material [23]. Crack extension occurs when the energy release rate reaches a critical value, $G = G_{cr}$.

There are three different types of force application to enable a crack to propagate [24]. *Opening mode*, or mode I fracture, is tensile stress normal to the plane of the crack. *Sliding mode*, or mode II fracture, is shear stress acting parallel to the plane of

the crack and perpendicular to the crack. *Tearing mode*, or mode III fracture, is shear stress acting parallel to the plane of the crack and parallel to the crack front. The various modes are illustrated in Figure 3.14.

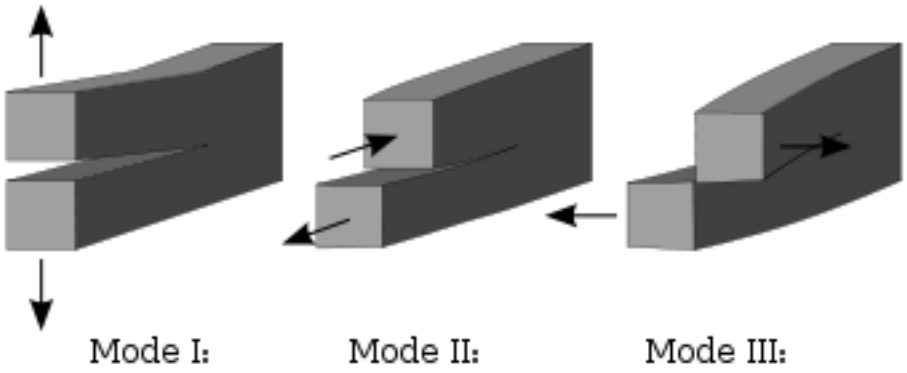

Figure 3.14: The three fracture modes

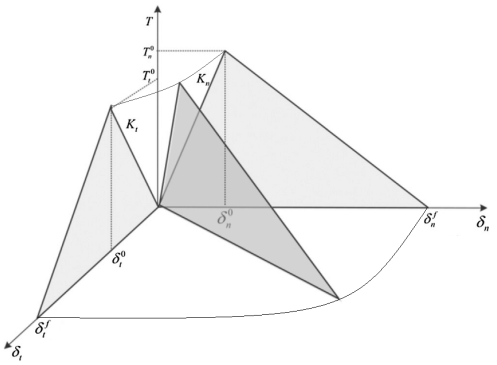

Figure 3.15: Graphical illustration of traction separation

Cohesive zone modelling is based (abbriv. CZM) on the theory of linear elastic failure mechanics. It was first introduced by Hillerborg to model brittle smeared cracks in concrete, but its application for wood was also discussed [25]. Abaqus Standard allows the use of cohesive zone as an interaction between surfaces in both 3D and 2D modelling [26]. CZM utilise the relationship between stresses and relative displacements Figure 3.15, to simulate the elastic behaviour up to the cohesive strength (T_n^0 in tension or T_t^0 in shear) and subsequent softening, to model the degradation of material properties up to failure. The constitutive behaviour before damage, damage initiation criterion and damage evolution have to be specified to describe material behaviour from linear elastic to failure. In this thesis, only the elastic behaviour is of interest. The triangular law assumes an initial linear elastic behaviour, where the elastic behaviour is defined by a constitutive matrix $[K_{CZM}]$ containing the stiffness parameters [26].

$$t = \begin{bmatrix} t_n \\ t_s \\ t_t \end{bmatrix} = \begin{bmatrix} K_{nn} & 0 & 0 \\ 0 & K_{ss} & 0 \\ 0 & 0 & K_{tt} \end{bmatrix} \cdot \begin{Bmatrix} \delta_n \\ \delta_s \\ \delta_t \end{Bmatrix} = K_{CZM} \cdot \delta \tag{3.47}$$

No coupling between stiffness coefficients was specified, therefore all terms outside the diagonal of $[K_{CZM}]$ matrix were assumed zero.

Material properties

The elastic material properties used in the models are displayed in the following tables [27].

Table 3.2: Material properties wood

Material property	**Symbol**	**Value**	**Input for Simulation**
Mean density $[\frac{kg}{m^3}]$	ρ_M	470	470
Moduli of Elasticity [MPa]	$E_L = E_{WO}$	13000	13000
	$E_R = E_T$	410	410
Shear Moduli [MPa]	$G_{LR} = G_{LT}$	760	760
	G_{RT}	65	30
Poisson ratios	ν_{LR}	0.501	0.60
	ν_{LT}	0.695	
	ν_{TR}	0.315	0.60
	ν_{RT}	0.835	

Table 3.3: Material properties steel

Material property	**Symbol**	**Value**	**Input for Simulation**
Mean density [MPa]	ρ_M	7850	7850
Moduli of Elasticity [MPa]	E	210000	210000
Poisson ratio	ν	0.3	0.3

3.2.2 Cohesive withdrawal properties

To model a 3D representation of the connection tested by Lied & Nordal [2], the values of the cohesive zone has to be determined. The cohesive zone stiffness properties K_{nn}, K_{ss} and K_{tt}, that represents the elastic behaviour, are in this thesis simplified to $K_{tt} = K_{ss}$ and the use of one value at rod perimeter. K_{ss} and K_{tt} represent the two shear modes respectively. As seen in Figure 3.16, the use of one set of parameter at the rod perimeter may be a good simplification for angles closer to 0 degrees, but not for angles close to 90 degrees. For smaller angles the wood have an equal shear stress failure, but as the inclination increases towards 90 degrees there is a clear difference between the two failure modes. Therefore the use of two parameters may give a better correlation. The influence of K_{nn} will be tested, but it is assumed that K_{nn} has minor influence on the vertical withdrawal stiffness.

(a) Failure mode of specimen $\alpha = 0^o$ (b) Failure mode of specimen $\alpha = 90^o$

Figure 3.16: Failure mode of specimen

A model based on H. Stamatopoulos' withdrawal tests [11] was made, see Figure 3.17. Dimensions (width · height), material properties and mesh size were kept constant, and loading was applied at the top of the rod. The rod was modelled with a diameter of $d_{inner} = 15\ mm$, as the inner diameter of the rod used in the experimental tests [10]. The top of the rod was clamped in the horizontal direction and free to move in the vertical direction (corresponding to the direction of withdrawal), as done in the experiment [11]. The only difference between the cohesive models, were the embedment lengths and the rod-to-grain angles, α. The values of K_{nn}, K_{ss} and K_{tt} were changed to match the withdrawal stiffness measured in the experiment, see Figure 2.4. The damage initiation criterion and damage evolution values are not of relevance in this thesis, where the main focus is the elastic stiffness.

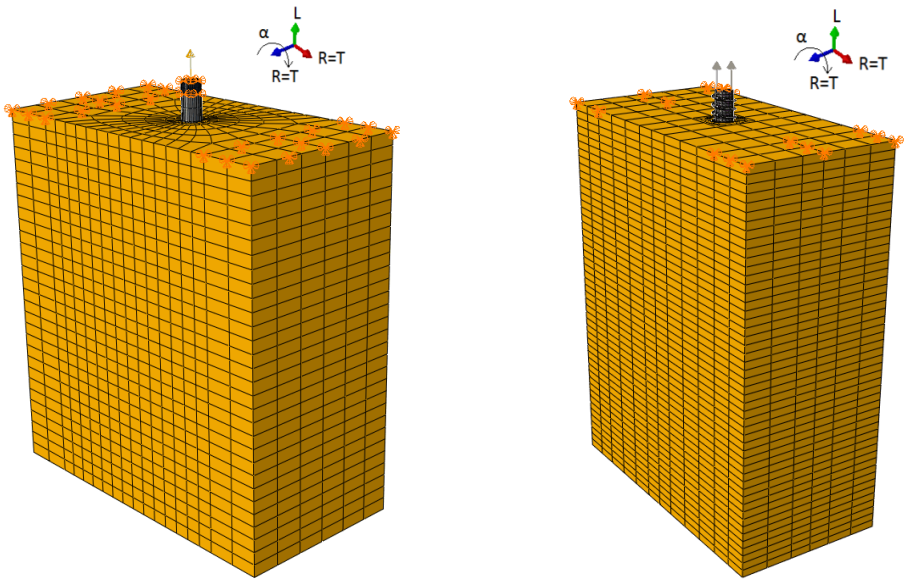

(a) Cohesiv zone model (b) Threaded rod model

Figure 3.17: Withdrawal models used in Abaqus.

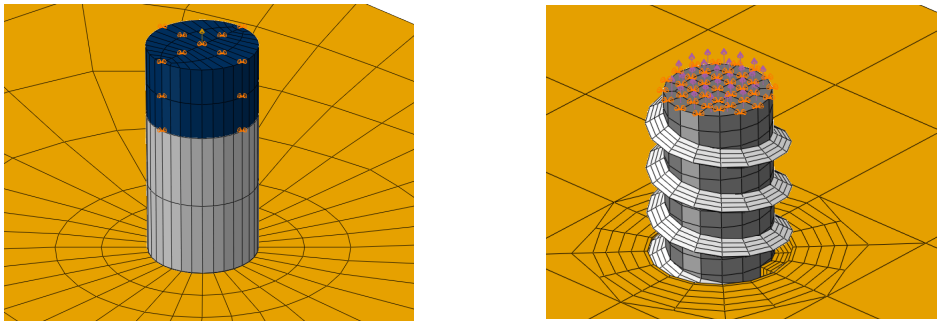

(a) Cylindrical rod (b) Threaded rod

Figure 3.18: Free length rod, as seen in Figure 3.18a, the loading in the cohesive model has been applied with the use of rigid body.

Sensitivity

The model was tested to evaluate the sensitivity of the cohesive zone and its parameters. Various tests were done; *mesh*, *stiffness parameter* and *equation solving* sensitivity.

Mesh sensitivity was performed by modelling a high density mesh along the rod perimeter, and changing the element height; 2 mm, 5 mm and 10 mm respectively.

The cohesive *stiffness parameters*, K, were tested by finding a value resulting in a withdrawal stiffness correlating with the experimental test performed by H. Stamatopoulos [11]. The value of the stiffness parameter was then adjusted using small increments and the change in withdrawal stiffness was measured.

Equation solving sensitivity was tested to check that the stiffness would not be

influenced by an increased amount of iterations. Since the equation solving was done by using a linear static analysis, this should have no impact on the result.

The result of the sensitivity studies are presented in Table 3.4

Table 3.4: Sensitivity

		Mesh	
Size		Stiffness	Change in stiffness [%]
2		99.16	0
5		99.24	0.08
10		99.39	0.16
		Equation Solving	
Iteration steps		Numerical stiffness	Change in stiffness [%]
1		99.39	0
10		99.39	0
		Withdrawal parameters	
K_{nn}	$K_{tt} = K_{ss}$	Numerical stiffness	Change in stiffness [%]
0.1	45	99.39	0
10	45	99.62	0.23
100	45	100.62	1.22
0.1	40	96.51	−2.89
0.1	50	101.86	2.49
0.1	60	105.92	6.58

Stiffness property K_{tt} and K_{ss}

To determine the cohesive values in the different models, a unit load $P = 1kN$ was applied. The withdrawal stiffness K_w was evaluated by:

$$K_w = \frac{P}{\delta} \tag{3.48}$$

Where P is the unit load applied at the top of the rod and δ is the displacement measured at the centre of the rod at the wood surface respectively. This location is chosen to exclude the extension of the free length of the rod, similarly to the simulations performed by H. Stamatopoulos [11]. In Figure 3.20, all the values are displayed. As seen, the values roughly range in the area $K_{tt} = 60 - 50$. For simplicity one set of parameters would be advantageous for the further work. Then the only variable would be the inclination of the rod.

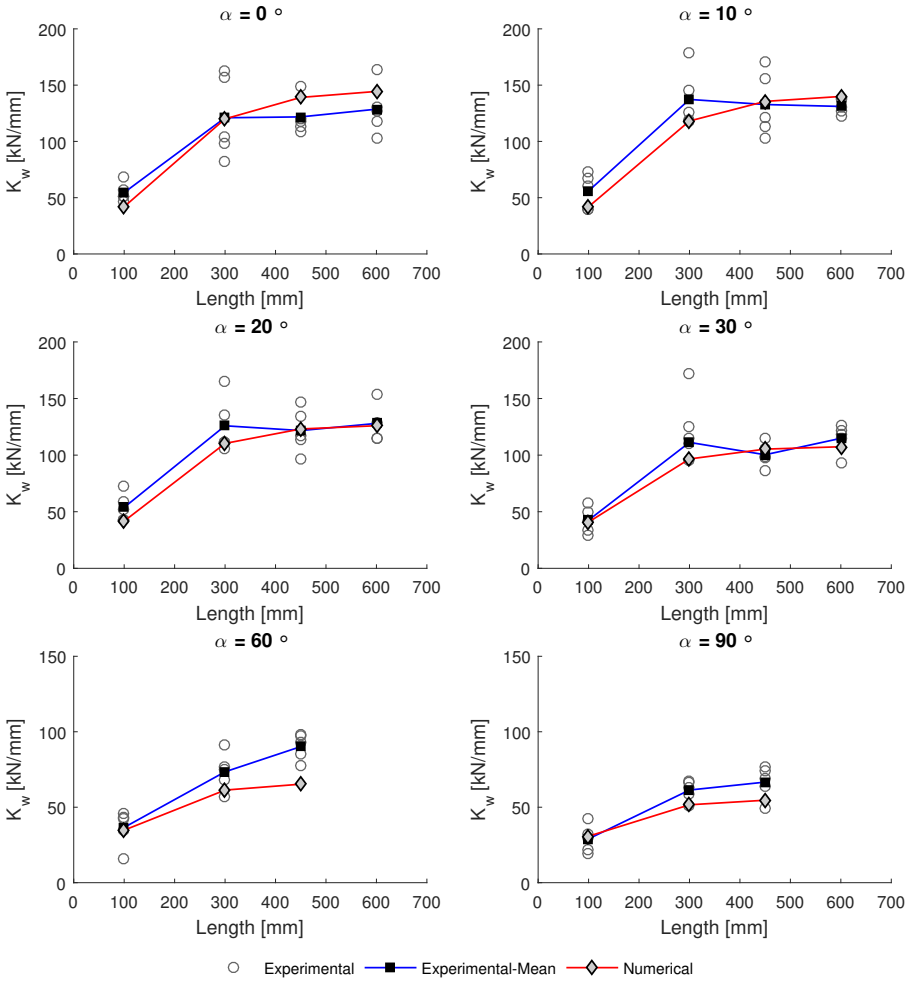

Figure 3.19: Stiffness with cohesive parameters calibrated for each length

As seen in Figure 3.19, there is a good correlation between the experimental results and the numerical simulations, especially at angles of 0 – 30 degrees. For larger angles the models are not able to replicate the measured experimental withdrawal stiffness. Especially for short lengths and larger angles such as 60 and 90 degrees. A similar drop in stiffness at smaller angles was also experienced in the numerical simulations with threaded rods, see Figure 2.4. The difference between the cohesive and threaded rod model, is that the threaded rod is stiffer than experimental measurements for angles of 0 – 30 degrees, but in good correlation for angles of 60 – 90 degrees.

To establish one set of parameters, the values found at length $l = 300\,\text{mm}$ is of interest. According to H. Stamatopoulos, the increase in stiffness is limited to lengths longer than $l \sim 300\,\text{mm}$ [11]. However, as seen in Figure 3.19 the values found at $l = 300\,\text{mm}$ are relatively high compared with the mean values for each angle. Therefore a second approach was to use the mean, of the mean values, for each angle. This was done in order to determine if this may result in a more satisfying cohesive value of K_{tt} for all angles. As displayed in Figure 3.20 the mean values for each length are as follows:

Table 3.5: Mean cohesive value of K_{tt} for each angle

	0°	10°	20°	30°	60°	90°	Mean of mean
Mean	49	60.5	63.75	56.25	60	60	**58.25**

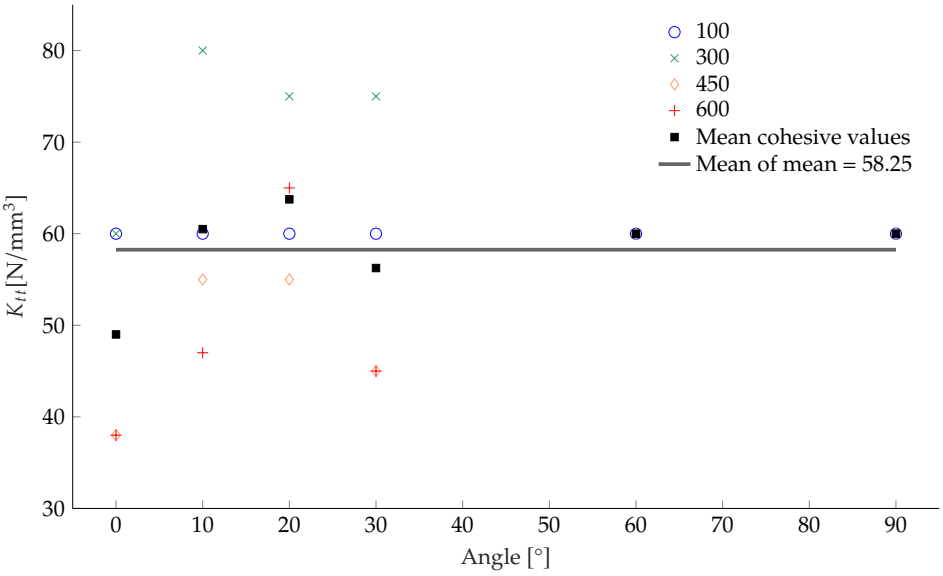

Figure 3.20: Cohesive values

In Figure 3.21 the stiffness measured in Abaqus compared with the experimental measurements shows a satisfactory result for larger angles and greater lengths, and within the range of measured stiffness. However, as seen in Figure 3.19, the stiffness does not correlate with the experimental measurements for lower angles such as 60 and 90 degrees and shorter lengths. In this thesis, the length of interest is primarily at $l > 300\,\text{mm}$, where $l = 450\,\text{mm}$ equals the width of the column. Consequently, a reduced stiffness for larger angles must be accounted for when investigating the stiffness of a beam-to-column connection. $K_{tt} = 58.25$ may therefore be a good approximation for the withdrawal stiffness. The use of cohesive values calibrated for $l = 100\,\text{mm}$ and $l = 300\,\text{mm}$ were tested. As seen in Figure 3.20, these values deviate from the mean values. The results can be seen in Appendix B.

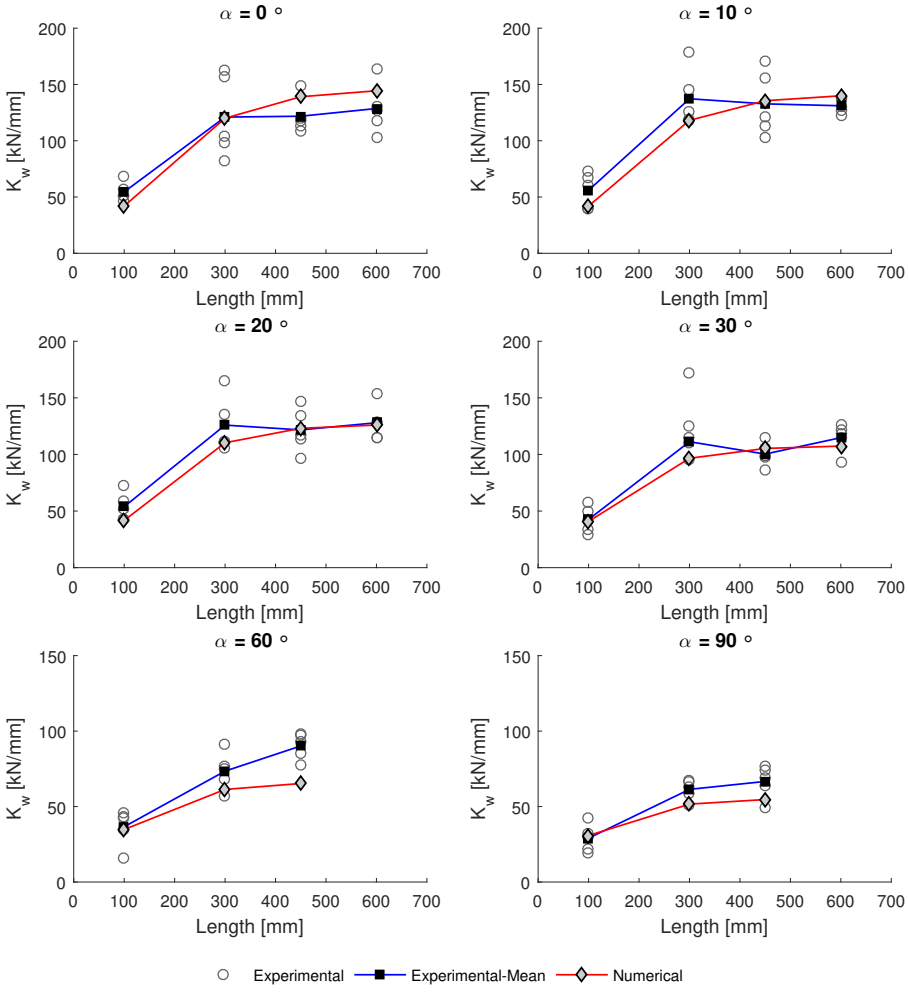

Figure 3.21: Stiffness with cohesive parameters set to a mean value: $K_{tt} = 58.25$

Stiffness property K_{nn}

The property of K_{nn} may be found in the paper written by D. Symons [28], where the slip-modulus of inclined screws on elastic foundations was studied. The principle is illustrated in Figure 3.22.

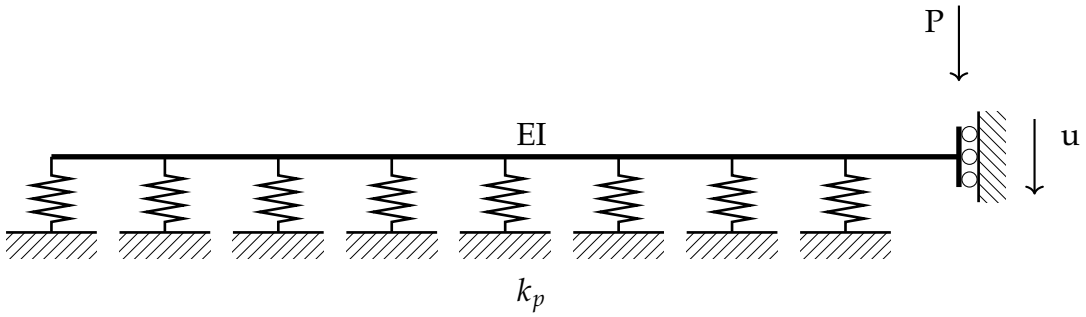

Figure 3.22: Vertical screw modelled as a beam on elastic foundation [28].

They found, that the modulus does not significantly depend on the diameter of the dowel. Diameters of 12 mm, 16 mm, 20 mm and 48 mm were tested without large differences. Studies of spruce showed that the ratio $\beta = k_t/k_p$ of the orthogonal modulus ranged from 0.63 to 0.56 , where k_t and k_p are the foundation modulus transverse and parallel to the grain respectively. Their findings, see Table 3.6, result in $K_{nn.\alpha=0} = \frac{1320}{16}$ N/mm^3 and $K_{nn.\alpha=90} = \frac{732}{16}$ N/mm^3.

Study	Gattesco (1998)	Gattesco and Toffolo (2004)
k_p [MPa]	1210	1320
k_t [MPa]	763	732
Ratio of modulus $\beta = \frac{k_t}{k_p}$	0.63	0.56

Table 3.6: Measurements of timber foundation stiffness for screw with $d = 16\ mm$

The modulus of elasticity of the wood-rod-interaction as a function of the inclination can be estimated by Hankinson's formula:

$$K_{nn.\alpha} = \frac{K_{nn.0} \cdot K_{nn.90}}{K_{nn.0} \cdot sin^2\alpha + K_{nn.90} \cdot cos^2\alpha} \tag{3.49}$$

Stress distribution along rod

The stress distribution along the rod was also evaluated to see if the decrease in stresses were observed. A comparison of the stress distribution in the threaded rods modelled by H. Stamatopoulos [11] was also preformed. As seen in Figure 3.23 the stresses along the rod decreased as expected, and correlated well with the analytical model. Similar figures for various rod-to-grain angles can be found in Appendix E. The stresses in the rod correlated with both the numerical measurements with threaded rods and an analytical estimation by H. Stamatopoulos [11]. As the force in the rod decreases, it is assumed that the stress within the rod is distributed and transferred to the wood.

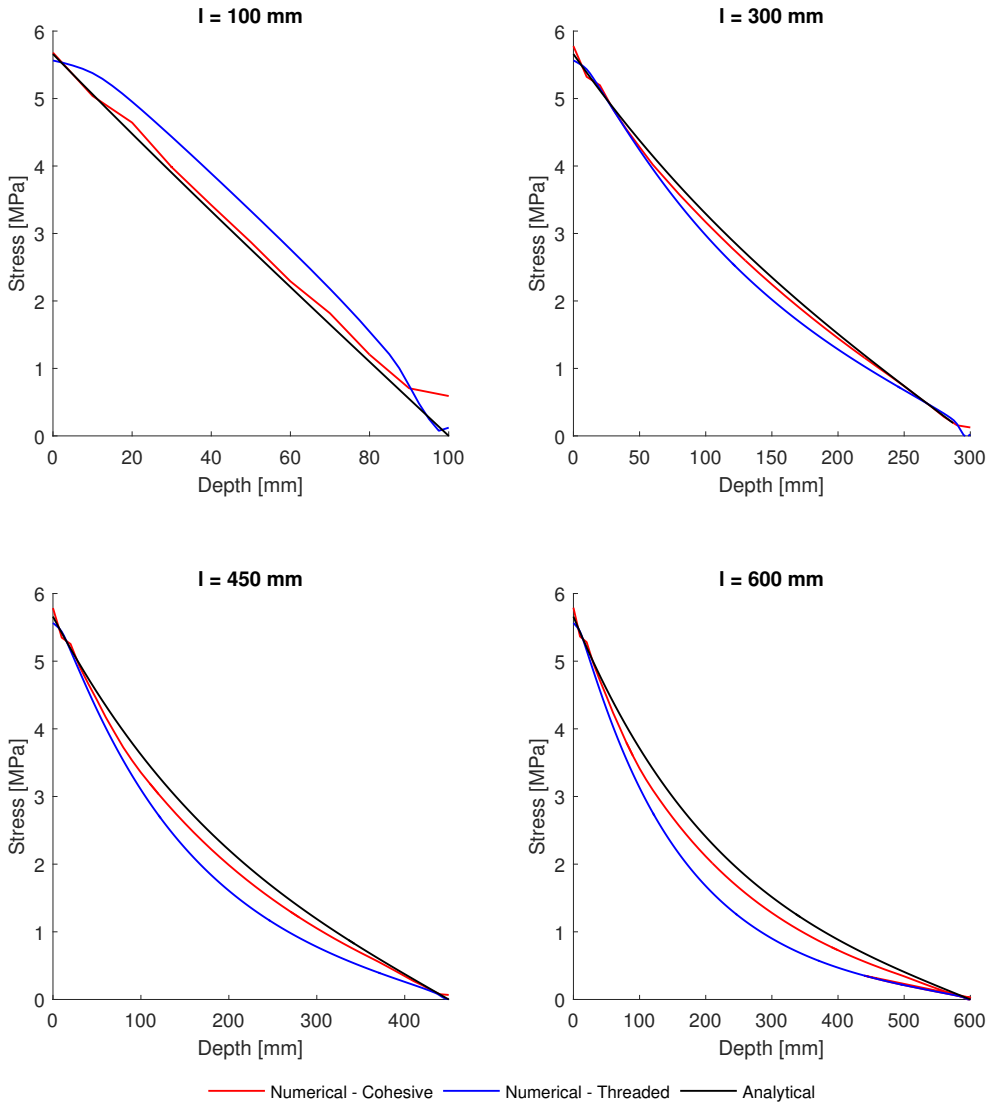

Figure 3.23: Distribution of axial stress in rods embedded along the grain.

3.3 Connector

The method of connecting the timber components has great impact on both the rotational stiffness and moment capacity. In this section various methods of connecting the threaded rods in the column and beam will be investigated.

3.3.1 Circular profile

The connecting circular profiles used by both Veium [14] and Lied & Nordal [2] proved to be an efficient solution when designing a connection where high stiffness is desirable. The experimental results showed high rotational stiffness and large capacity. They can also accommodate a wide range of rod inclinations. The mounting proved to be fairly uncomplicated as the circular profiles were split in two parts, see Figure 3.24b, allowing them to be fastened from each side after the threaded rods were embedded in the timber elements.

The main disadvantage may be the size of the circular profile. To have enough space for three rods with tensile plates and two nuts, an inner diameter of 110 mm – 120 mm was required. This meant that a part of the beam had to be removed, as seen in Figure 3.24a. To maximise the moment arm, the profiles also extend above the face of the beam, which may be inconvenient when considering flooring and other instalments which will need to be placed on top of the beam if this type of connection is to be used in practice.

(a) The circular steel profile fully mounted (b) The two parts

Figure 3.24: The circular steel profile used by Veium [14] and Lied & Nordal [2]. Images from [2].

One of the main reasons for using a circular steel profile in a beam-to-column-connection was the easy adjustment for different rod inclinations. As the most favourable combination of rod-to-grain angles is decided, this would allow for the steel profile to be customised for these angles. This may lead to a reduction in dimensions and a possibility of increased stiffness.

3.3.2 Design criteria

The main focus when designing a new steel profile was to not compromise the favourable properties of the circular steel profile. This meant that the improved profile also should possess high stiffness, sufficient capacity and easy mounting. Ideally the new profile should improve on these properties while simultaneously occupy a smaller space. If the connection is to be used for structural applications, the steel profile should also allow the beam, which in reality may be a part of a slab, to be lowered down unobstructed.

3.3.3 Design procedure

Several ideas for a new design of the steel profile were discussed. If the rods connected to the steel profile in the same spot seen from side view, the height of the profile would be drastically reduced. However, due to the width of the timber elements this is not possible.

One of the earliest versions was a steel plate with a width equal to that of the timber elements. Various alternative locations of the plate were examined. By placing it on the surface of the column, a part of it had to be cut in order to fasten the beam rod. Due to the limited depth of the column, this was not desired as it could drastically reduce the stiffness of the column component. Consequently it was decided to locate the plate in a sufficient distance from the column face so the cuts would be done in the beam rather than the column.

The holes for the three rods were initially aligned vertically, replicating the number of rods used in the experimental testing by Lied & Nordal. However, during the process of determining the optimal combination of angles, a configuration where some of the rods crossed each other in side view was discussed. By locating the holes asymmetrically with respect to the vertical centre line of the plate, it was possible for the middle rods to cross each other. Due to the width of the column it would only be spacing of 3.4 mm between the outer threads of the rods in this location, leaving a very small margin for error. It was desirable to examine if the large angles and long embedment lengths would result in high rotational stiffness. Consequently it was decided to continue with this configuration to see if the rotational stiffness and moment capacity were of sufficient magnitudes to warrant the added need for preciseness during the screwing phase.

Originally the steel plate was vertical with washers and nuts providing inclination allowing the rods to adjoin at a perpendicular surface with respect to the longitudinal axis of the rods. The reason for this was to facilitate an easy production phase. However, there were concerns that more parts would lead to a reduction in stiffness of the connection. Consequently it was decided to bend the plate such that the plate itself provided the perpendicular surface where the rods connected. The redundant steel of the version of the plate where the holes were vertically aligned, was trimmed, leaving two connectors possessing a width of 40 mm each per zone.

Due to the need for sufficient space for the nuts fastening the beam rod on the tension side, the free length of the column rods is not as short as desirable. A similar situation occurs on the other side of the plate where the nuts fastening the upper column rod CU1 need sufficient distance to the beam. Rod CU2 is not a problem as the nuts are above the surface of the beam.

Sections of the final design for two selected configurations is displayed in Figure 3.25. One of the advantages with this design is the flexibility in accommodating various rod inclinations. The only parameter that would need to be altered is the extent of the bending of the plate between the holes, as illustrated in Figure 3.25.

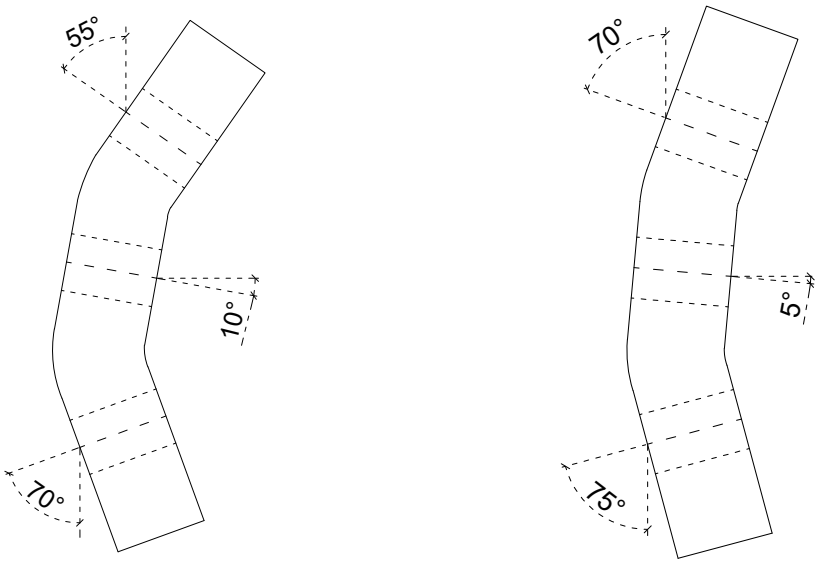

(a) Plate for 70-55-10 (b) Plate for 75-70-05

Figure 3.25: Steel plate

3.3.4 Rotational stiffness of the connector

The main focus in this thesis is the rotational stiffness of the connection. Consequently, this is the most important parameter to consider when evaluating the various configurations of the connecting steel profile.

Component method

The spreadsheet described in subsection 3.1.2 provided by Aivars Vilguts was modified in order to calculate the rotational stiffness of the connection with the new steel profile. Additionally, the inclination of rod BU in the beam was changed to evaluate the stiffness of configurations with an angle of 5 degrees.

A configuration similar to test 4 by Lied & Nordal [2], where the column rods CU1 and CU2 had inclinations of 70 and 55 degrees respectively, increased from 14 263 kN m/rad to 15 498 kN m/rad. The changed input parameters were the free lengths due to the new steel profile and the inclination of rod BU in the beam of 5 degrees. As the free lengths increases, the higher rotational stiffness is mainly contributed to the smaller angle of rod BU. A figure similar to Figure 3.10 where the rotational stiffness is plotted for varying rod-to-grain angles is presented in section A.4.

Numerical modelling

To determine the dimensions of the steel plate, a simplified Abaqus 3D model was constructed. The model consisted of the upper and lower steel profiles and a part of the beam and column. The timber components were modelled as rigid bodies and thus not given proper material properties. The threaded rods were connected to the timber parts at the surface using tie constraints which enables them to act as one part. Both the definition of rigid bodies and the tie constraints were done in order to solely measure the stiffness of the steel profile. Consequently, e.g. withdrawal is not included in this model.

The column part was constrained at the top and bottom faces. The loading was applied as a horizontal tension force at the center of the upper beam rod at the face of the beam part, and an equally large horizontal compression force at the same location in the lower part of the beam. Additionally a vertical force was applied at the centroid of the beam part. An overview of the model, including mesh, loading and boundary conditions can be seen in Figure 3.27a.

Calculation of rotational stiffness

To estimate the rotational stiffness of the numerical models, the horizontal displacements in a total of four locations was measured. One measuring point was on the beam at the upper edge, $\Delta_{x.u.beam}$, and one in a point projected vertically from the upper point down to the lower edge, $\Delta_{x.l.beam}$. There were also two measuring points on the column, $\Delta_{x.u.column}$ and $\Delta_{x.l.column}$, to account for its lateral movement. These were located at equal height as the measuring points on the beam and at the centre line of the column. The locations of the measuring points can be seen in Figure 3.26.

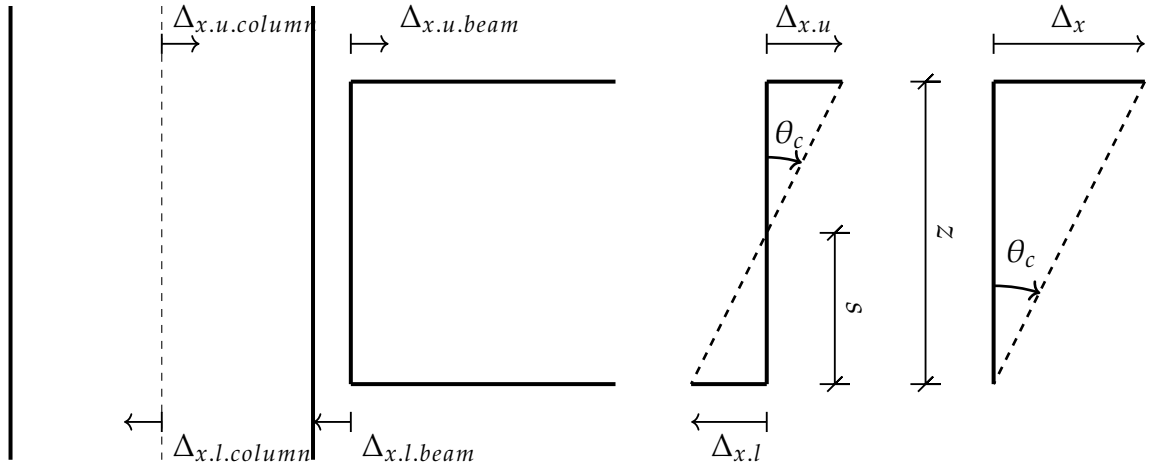

Figure 3.26: Illustration of the locations of the measuring points and the rotation-displacement relation.

The upper and lower horizontal displacements are calculated by subtracting the displacement of the column:

$$\Delta_{x.u} = \Delta_{x.u.beam} - \Delta_{x.u.column} \tag{3.50}$$

$$\Delta_{x.l} = \Delta_{x.l.beam} - \Delta_{x.l.column} \tag{3.51}$$

The rotational center is then found by calculating the ratio of the triangles in Figure 3.26:

$$s = \Delta_{x.l} \cdot \frac{z}{\Delta_x} \tag{3.52}$$

Where s is the vertical distance from the lower edge of the beam, z is the beam height of 450 mm and $\Delta_x = \Delta_{x.u} + \Delta_{x.l}$ is the two horizontal displacements.

The rotation is then calculated as:

$$\alpha = \arctan \frac{\Delta_{x.l}}{s} \tag{3.53}$$

Knowing the rotation the rotational stiffness is given by:

$$K_{rot} = \frac{M_{Ed}}{\alpha} \tag{3.54}$$

Where M_{Ed} is the moment acting due to the applied point load:

$$M_{ed} = L \cdot F \tag{3.55}$$

To compare the new design with the circular profile, the latter was also modelled using the same procedure as described above. The result can be seen in Figure 3.27b. This was done to ensure that the two models were as similar as possible, leaving only the design of the steel profile as a parameter.

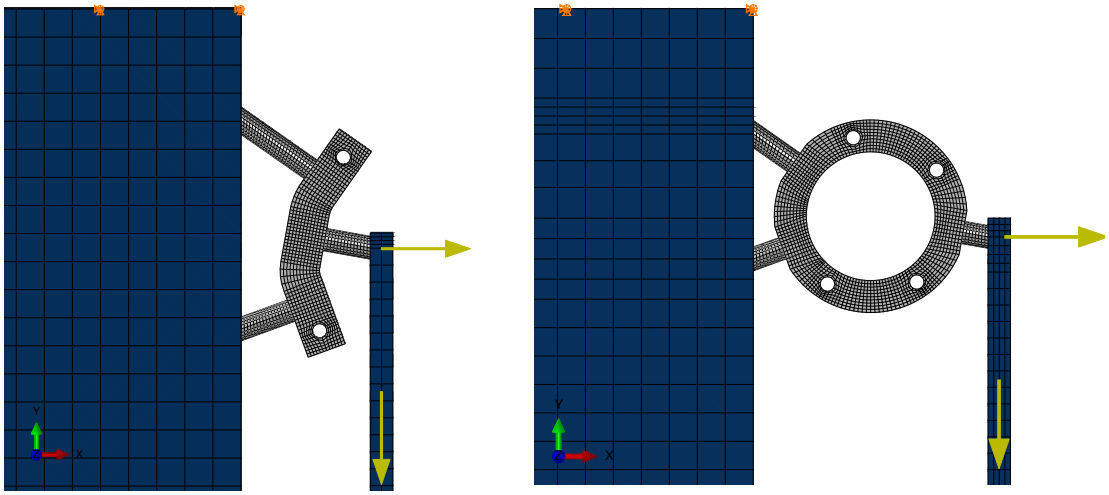

(a) New design

(b) Circular profile

Figure 3.27: Steel profiles

Only the upper part of the model and the vertical force is included in Figure 3.27. The lower part is a mirrored copy where the only difference is the opposite load direction of the horizontal force.

The rotational stiffness was evaluated by applying horizontal and vertical forces of magnitudes corresponding to 10 % of the estimated maximum point load as calculated by Lied & Nordal [2] through the following relations:

$$F = \frac{P \cdot 10\% \cdot L}{z} \tag{3.56}$$

$$V = \frac{P \cdot 10\%}{2} \tag{3.57}$$

The rotational stiffness was then calculated as previously described. Due to the rigid body definition and boundary conditions, the horizontal movement of the column is constrained. Thus, only the movement of the beam contribute to the upper and lower displacements.

To examine the influence of the thickness of the plate, two models with different thicknesses were made. In this section, thickness refers to the width of the plate along the rod axis in side-view. Both had rod inclinations identical to the circular profiles used in test 4 by Lied & Nordal [2].

Results

Table 3.7: Comparison between various configurations and connectors

Configuration Connector type	Thickness [mm]	Rod no.	Free length [mm]	Vertical displacement [mm]	Rotational stiffness [kN m/rad]
70-55-10 Circular	30	CU1 CU2 BU	28.0 44.4 22.9	-0.0460	24 663
70-55-10 Plate	30	CU1 CU2 BU	47.7 76.5 41.1	-0.0199	26 017
70-55-10 Plate	35	CU1 CU2 BU	47.7 76.5 41.1	-0.0192	34 491
70-70-10 Plate	35	CU1 CU2 BU	57.5 48.0 41.1	-0.0199	38 858
70-70-05 Plate	35	CU1 CU2 BU	50.5 54.7 40.3	-0.0198	43 269
45-45-10 Plate	35	CU1 CU2 BU	84.6 96.9 46.3	-0.0231	22 680

A thickness of 30 mm resulted in a rotational stiffness similar to the circular profile. Increasing the thickness to 35 mm caused the plate to be 33 % stiffer. Consequently, it was decided to model the remaining configurations with a thickness of 35 mm.

The configuration which possessed the highest rotational stiffness was 70-70-05 with a thickness of 35 mm. Additional dimensions are presented in Figure 3.28a.

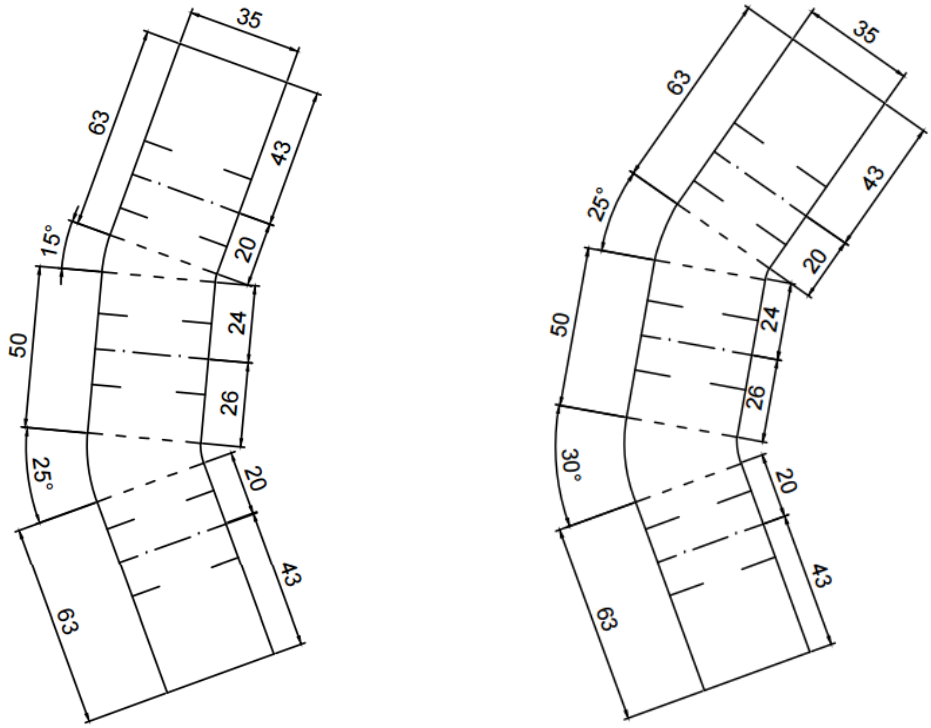

(a) Plate for 70-70-05 with dimensions (b) Plate for 70-55-10 with dimensions

Figure 3.28: Steel plate

The connection with the new steel plate is presented in Figure 3.29 for 75-70-05. As illustrated a considerable part of the beam has to be removed leaving the connector and rods exposed to e.g. fire. Additionally the desired reduction in height was not obtained resulting in the connector extending above the surface of the beam similarly to the circular profile.

Additionally, the steel volume of the different plates was calculated and compared to the circular profile. Even though the material cost of steel is relatively low, it would not be desirable if the steel plate required more material per plate than the circular profile considering that the production cost is presumably lower for the latter. This assumption is based on the need for a customised steel plate, while the circular profile is manufactured by cutting steel pipes. Calculations and results can be found in section A.3.

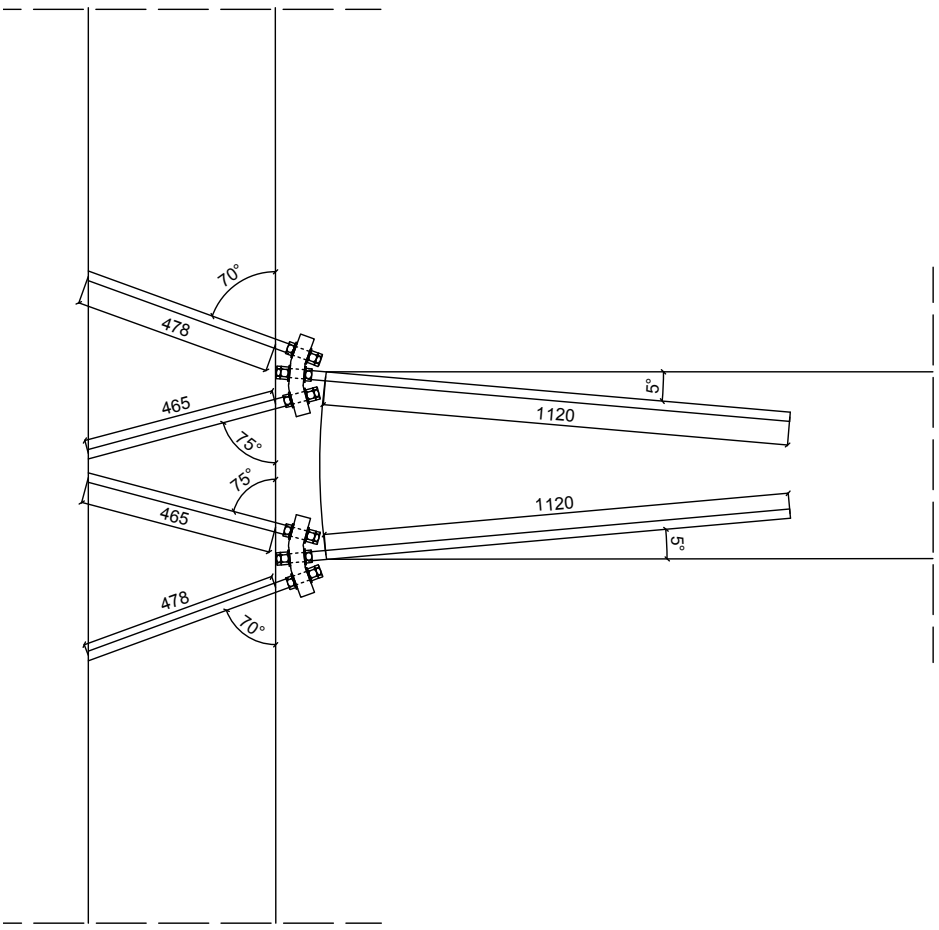

Figure 3.29: 75-70-05 with steel plate

3.3.5 Assembly

On of the main design criteria was to accommodate an uncomplicated assembly phase for the entire connection. The steel profile acts as the sole connecting part between the beam and column and is therefore paramount in order to achieve this objective.

When considering how to fasten the steel profile, there are mainly two alternatives. The first one is based on a similar principle as the circular profile. The plate is split in half along the centre line of the holes for the rods. When the beam and column are in the correct position the two halves would be installed from either side and fastened with bolts. These would penetrate the entire width of the profile perpendicular to the longitudinal axis of the rods. The locations are both ends of the plate, as can be seen in Figure 3.27a. Additionally, there may be need for two bolts in the inner gaps between the rods in order to tighten the two steel halves sufficiently, resulting in the section displayed in Figure 3.30a.

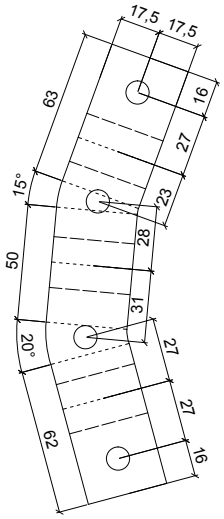

(a) The connector for 75-70-05 with holes for fastening bolts

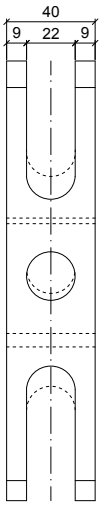

(b) The connector for 75-70-05 with openings for the column rods

Figure 3.30: The two alternatives for assembling the steel connector

The second alternative is to let the holes for the column rods extend to the top of the plate, as illustrated in Figure 3.30b. This allows the steel profile to be placed on the beam rod before it is lifted into position. When the column rods and beam rods are correctly aligned, the profile is pushed toward the column and the nuts are screwed on. In order for this to be possible, a part of the beam surrounding the beam rods has to be removed to allow the steel connector to go clear of the column rods when the beam is lowered into position. This method is best suited for larger angles as the rods are more parallel. Consequently, the required spacing in order to let the end of the rod pass through the profile during the assembly, is reduced.

3.4 Numerical models of various configurations

The use of Abaqus as a numerical tool to model a complete representation of the moment resisting connection is of interest. The intention is to evaluate if numerical simulations may produce results in good agreement with experimental testing.

There are many advantages of a complete numerical model. The main objective, which is measurement of stiffness, may easily be extracted. Also the use of a numerical model enables extraction of normal stresses (σ) and shear stresses (τ) in the steel and wooden parts, and may be useful in the evaluation of the new design.

Cohesive modelling, using the parameters and configurations found in subsection 3.2.2, will be utilised to simulate the withdrawal of threaded rods.

To evaluate the robustness of a full connection model, the experimental testing performed by Lied & Nordal [2] will be of relevance. The dimensions used in the models are displayed in Table 3.8:

Table 3.8: Measurements of parts Abaqus

	Cross section $[mm^2]$	Length $[mm]$
Beam	70×450	2250
Column	70×450	3500
Steel rod	$\pi \times 8^2$	N/A

The model consist of several parts; beam, column and steel connector. To reduce the computational time, the model has been modelled with the use of symmetry. All wooden parts have the depth of 70 mm, which equals half the experimental depth of 140 mm. To model symmetry in the steel connection, the use of one circular profile instead of two has been applied. The circular profiles have been modelled equivalent with the profiles used in the experimental testing by Lied & Nordal according to their specification [2]. The rods were modelled with the use of the inner diameter, d_{rod} = 16.13 mm, and the threaded part was neglected. Material properties described in Table 3.2 and Table 3.3 were used as input values for the different materials. The wooden parts were given local material orientation, identically to the material orientations used in the experimental testing.

All parts in the model are made of C3D8 elements, an eight node solid element. To reduce the computational time, the use of reduced integration has been applied. This would also give a better result for the stresses in each element, as these will be extracted from the Gauss points [17]. The mesh parameters used in subsection 3.2.2

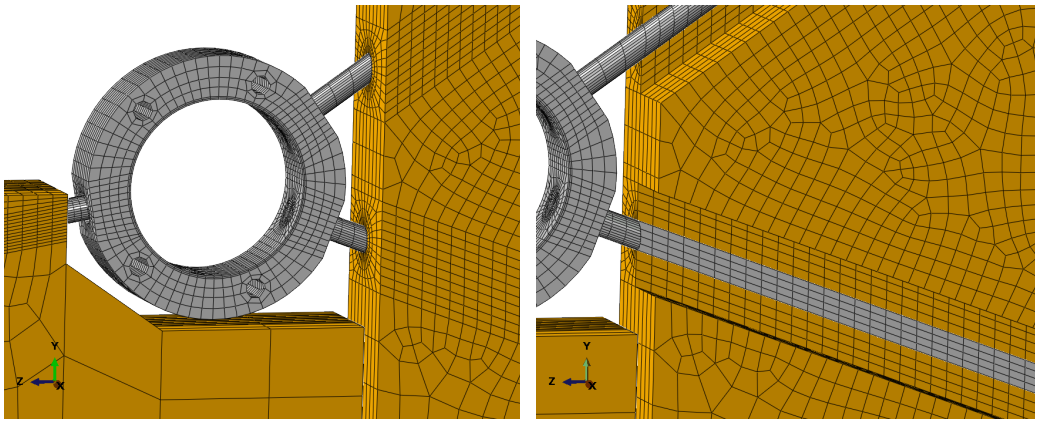

(a) Steel profile (b) Rod in wood

Figure 3.31: Mesh at different parts in the model

to simulate the withdrawal of the rod, have been applied to the rod and wood. As seen in Figure 3.31 some parts have a structured meshing technique and some parts have a non structured meshing technique. The wood surrounding the rod, has a structured meshing technique to avoid excessive distortion of elements due to complicated geometry. The mesh geometry for the rod is listed in Table 3.9. At the loading point the use of rigid body has been applied to simulate a uniform loading, similarly to the load application in the experimental tests.

Table 3.9: Mesh size rod

Edge	Mesh size
Perimeter	$\sim$ 1.57 mm [1]
Length	10 mm

[1] This gives eight elements per 90 degrees.

The Cartesian coordinate system of the model, is given by y-axis in the longitudinal direction of the column and the z-axis in the longitudinal direction of the beam. Due to symmetry, a loading of [0,-$\frac{\mathbf{P}}{\mathbf{2}}$,0] kN was applied at l = 2015 mm from the column face, as done in the experimental testing [2]. To simulate the stress state in the column, the loading applied at the beam were P_{test3} = 36 kN and P_{test4} = 60 kN. This were based on the capacity of the experimental tests by Lied & Nordal [2]. At this magnitude the crack in the column propagated in test 4. As for the new design configurations, the loading will be P_{test4} = 60 kN in order to compare the different models. Boundary conditions were applied to the top and bottom surfaces of the column, clamping the translation in x-, z- and y-direction at bottom, and x-and z-direction at top. At the symmetry line the model was constrained in the x-direction.

Result extraction

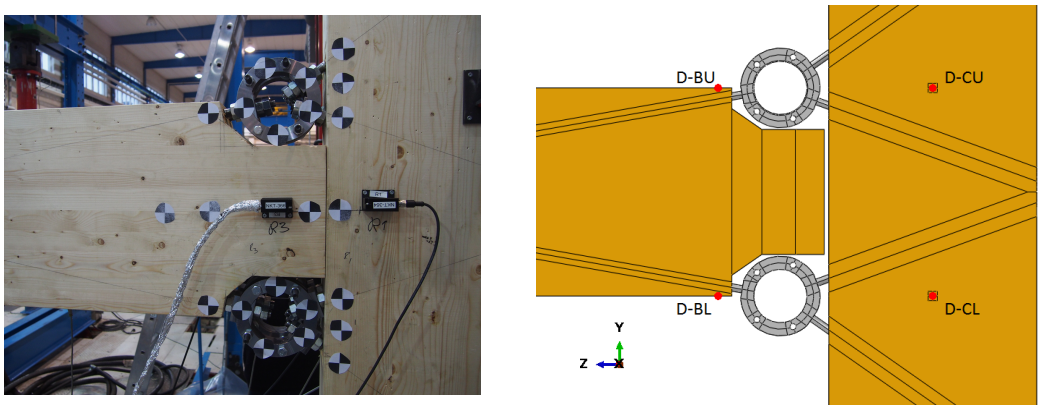

(a) Experimental testing of test 4 [2].

(b) Numerical model of 70-55-10

Figure 3.32: The experimentally tested connection replicated numerically

The rotational stiffness was calculated as described in subsection 3.3.4. Measuring points were located at the column and at the beam. The locations can be seen in Figure 3.32. At these points the horizontal displacement was measured. To evaluate the distribution of forces in the connection, the measurement of forces in each steel rod is of interest. This was done to see that a favourable distribution of forces was achieved with the design. Also the investigation of shear stress in column is of interest, in order to evaluate the magnitude and to see if the stress state can describe the shear crack observed in the column during the experimental tests [2]. As observed in the loading test of configuration 70-55-10, the DIC recordings indicate that the crack propagation started in the outer area of the column as showed in Figure 3.33. The results from the various configurations may be useful to evaluate which one that have the best potential to possess both high stiffness and large load capacity.

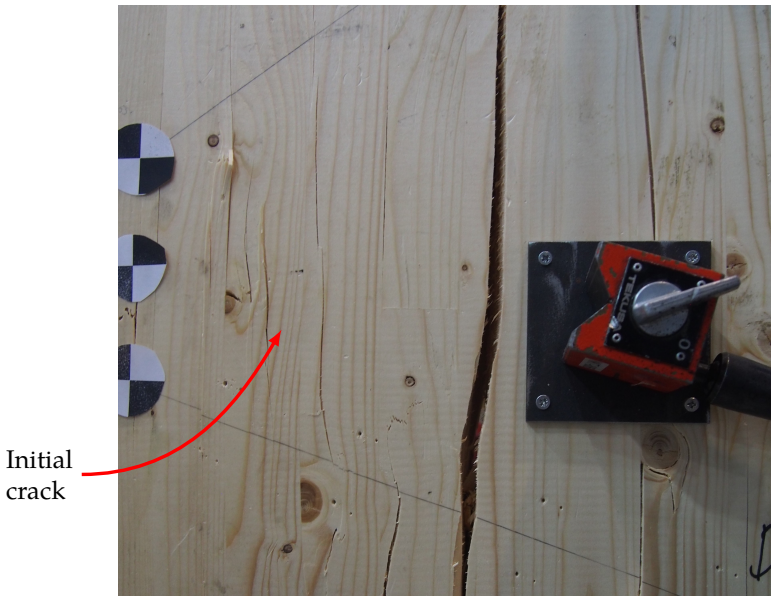

Figure 3.33: Cracking in the column in the experimental testing performed by Lied & Nordal [2].

3.4.1 An overview of the configurations

An array of the different configurations can be seen in Figure 3.34 and Appendix C. As seen in Appendix C, 55-35-10 (corresponding to test 3 by Lied & Nordal [2]) has two shorter rods, these two rods have a length shorter than $l = 450\,\text{mm}$. As mentioned in subsection 3.2.2, the stiffness measured in the cohesive model and the experimental tests do not coincide for shorter embedment lengths. A reduced stiffness for this configuration is therefore to be expected.

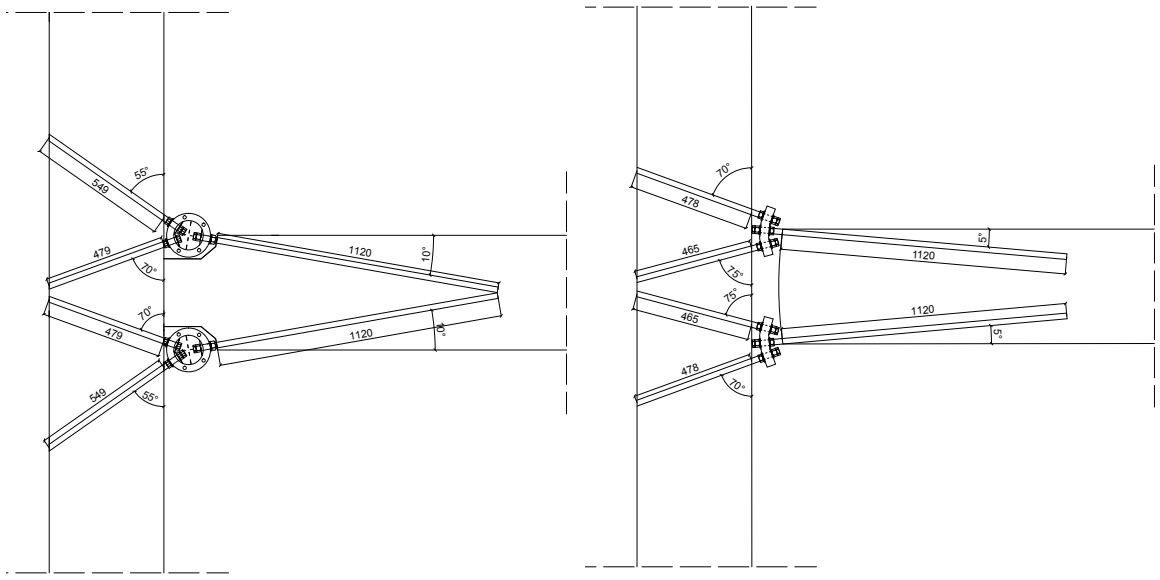

(a) 70-55-10

(b) 75-70-05

Figure 3.34: A variety of different configurations

3.5 Fire design

The connection is designed to be a part of the main structural system in multi-storey buildings. Consequently, the connection is classified as R90 in the WoodSols-specification [1]. This results in strict requirements regarding fire resistance. To investigate the performance of the connection in a fire situation, simplified calculations of the fire resistance of the preliminary design will be performed.

Reduced cross-section method

Evaluation of fire resistance is done by use of the reduced cross-section method in EC5-1-2 [29]. The procedure is to reduce the initial cross-section by the effective charring depth for the duration specified by the fire classification. Due to the large dimensions of the timber elements, one-dimensional charring is assumed.

The effective charring depth is calculated as:

$$d_{ef} = d_{char.n} + k_0 \cdot d_0 \tag{3.58}$$

Where $d_0 = 7\ mm$ and $k_0 = 1.0$ for a duration larger than 20 minutes. $d_{char.n}$ is the charring depth:

$$d_{char.n} = \beta_n t \tag{3.59}$$

Where β_n is the notational design charring depth for one-dimensional charring, incorporating the effect of corner roundings and t is the time of fire exposure. Table 3.1 in EC5-1-2 specifies a β_n of 0.7 mm/min for glulam members with $\rho_{char} \geq 290\,\mathrm{kg/m^3}$.

Considering a fire exposure of 90 minutes, the resulting effective charring depth is:

$$d_{ef} = 0.7\,\frac{\mathrm{mm}}{\mathrm{min}} \cdot 90\,\mathrm{min} + 7\,\mathrm{mm} \cdot 1.0 = 70\,\mathrm{mm} \tag{3.60}$$

EC5-1-2 does also provide rules regarding edge distances and spacings. In order to protect the threaded rods, the required edge distance is:

$$a_1 = d_{ef} + \frac{d_{outer}}{2} = 81.2\,\mathrm{mm} \tag{3.61}$$

Considering a spacing of 40 mm the total depth necessary to satisfy the requirements in EC5-1-2 is:

$$2 \cdot a_1 + 40\,\text{mm} = 202.3\,\text{mm} \tag{3.62}$$

Due to the requirement of moment resisting properties, the capacity of the connection is presumably larger than requirements in limit state design. The consequence is the possibility of locating one of the rods within the charring depth, and let the others carry the load in a fire situation. In order to examine if this is achievable, it is necessary to calculate the total load in the serviceability limit state.

Loading

The purpose of the connection is the transferring of forces from slabs to columns in multi-storey buildings. Thus, the loading in serviceability limit state (SLS) will consist of the self-weight of the slab and an imposed load according to Eurocode 1.

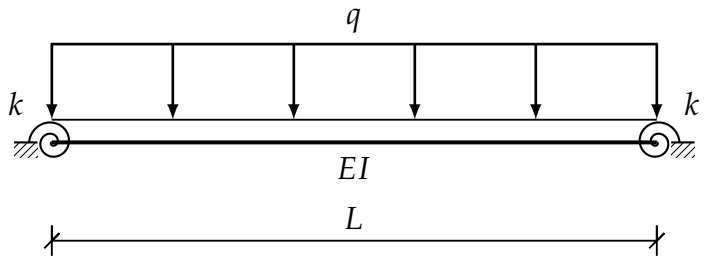

Figure 3.35: Beam with rotational springs at the supports subjected to a uniformly distributed load

By considering the beam in Figure 3.35, which has supports at each end with an equal, specified rotational stiffness and is subjected to a uniformly distributed load, the following formula for the acting moment in the supports can be derived:

$$M_{joint} = \frac{qL^3}{24EI}\left[\frac{L}{2EI} + \frac{1}{k}\right]^{-1} \tag{3.63}$$

The complete derivation may be found in section A.2.

Consequently, the moment in the joint will depend on the rotational stiffness of the connection. In the following calculations a stiffness of 10 000 kN m/rad will be assumed.

Self-weight

The magnitude of the self-weight of the slab is based on a value provided by fellow master students Bjørge & Kristoffersen who constructed a slab weighing 2111 kg according to laboratory equipment [30]. A length of 10 m and a width of 2.4 m results in a self-weight of $0.8626\,\mathrm{kN/m^2}$. This is corroborated by a master thesis by Åby & Hartnes where a line load of 2.07 kN/m is calculated [31]. With dimensions identical to Bjørge & Kristoffersen, the resulting self-weight is $0.8625\,\mathrm{kN/m^2}$. In the following calculations, the self-weight is conservatively approximated to $1\,\mathrm{kN/m^2}$.

Imposed load

NS-EN 1991-1-1 provides requirements for imposed loads on slabs used in structures of different categories. These are found in table NA 6.1 [32]. As the connection and slab are designed as a general case, the category which gives the largest load is selected. C1, C2 and C3 results all in an imposed load of $5\,\mathrm{kN/m^2}$ in table NA 6.2 [32].

Total load

The total load in SLS is calculated according to the rules given in NS-EN 1990 section 6.5.3 [33]. Each load contribution is combined through the following equation:

$$E_d = \sum_{j\geq 1} G_{k,j} + P + \sum_{i\geq 1} \psi_{2,i} Q_{k,i} = G_k + \psi_{2,1} Q_{k,1} \tag{3.64}$$

Where G_k is the self-weight and $Q_{k.1}$ is the imposed load. The factor $\psi_{2,1}$ is given by the national annex table NA.A1.1 for the same categories as imposed loads. The largest factor is for storage areas where $\psi_2 = 0.8$. Conservatively, $\psi_2 = 1.0$ is used, resulting in a total load of:

$$E_d = 1\,\mathrm{kN/m^2} + 1.0 \cdot 5\,\mathrm{kN/m^2} = 6\,\mathrm{kN/m^2} \tag{3.65}$$

This can be expressed as a line load, q, by considering the width of the slab:

$$q = E_d \cdot \frac{b_{slab}}{2} = 6\,\mathrm{kN/m^2} \cdot \frac{2.4\,\mathrm{m}}{2} = 7.2\,\mathrm{kN/m} \tag{3.66}$$

Having defined all the parameters, including $E = 13\,000\,\mathrm{MPa}$, and inserted $I = \frac{bh^3}{12}$

in Equation 3.63, the moment can be calculated as:

$$M_{joint} = \frac{qL^3}{2Ebh^3}\left[\frac{6L}{Ebh^3} + \frac{1}{k}\right]^{-1} = 47.0\,\text{kN m} \tag{3.67}$$

In order to achieve an acting moment of this magnitude, the following point load need to be applied in the numerical simulations:

$$P = \frac{M}{L} = \frac{47.0\,\text{kN m}}{2\,\text{m}} = 23.5\,\text{kN} \tag{3.68}$$

Configuration

Expanding the width from 140 mm to 203.4 mm enables some adjustments that were dismissed previously due to the limited space. E.g. the possibility of locating the two inner rods, CU1 and CL1, in different planes. This facilitates inclinations similar to 55-35-10 that was tested experimentally by Lied & Nordal exhibiting high rotational stiffness [2]. The capacity however, was fairly low as a result of withdrawal of the inner rods due to short embedment length. The reason for the short embedment length was insufficient space for the rods to cross each other. By enabling this, the result may be a configuration possessing both the high rotational stiffness measured in the experimental testing and sufficient moment capacity.

A configuration of 65-70-05 possessing a width of 215 mm was modelled using the same procedure as described in section 3.4. The inclinations were chosen on the basis of the component method and the numerical simulations of the other configurations. Symmetry was utilised, resulting in a width of 107.5 mm. The location of rod CL1 was changed from being aligned with the others, to a horizontal distance of 32 mm from centre line to centre line. An illustration of the section view is displayed in Figure 3.36.

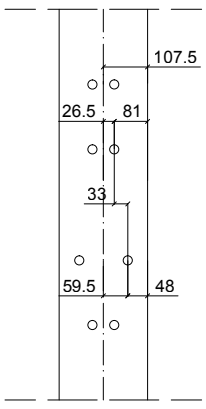

Figure 3.36: Illustration of rod spacings and edge distances for 65-70-05

Rod CL1 are located within the charring depth of 70 mm. In order to control the bearing capacity in a fire situation, these rods were removed from the numerical models and simulated with the load from Equation 3.68. To replicate the statical conditions in a moment resisting frame where the beam is supported on both sides, the free end in the model were constrained in the horizontal direction. A sketch of the configuration including the constraints of the free end of the beam, is displayed in Figure 3.37.

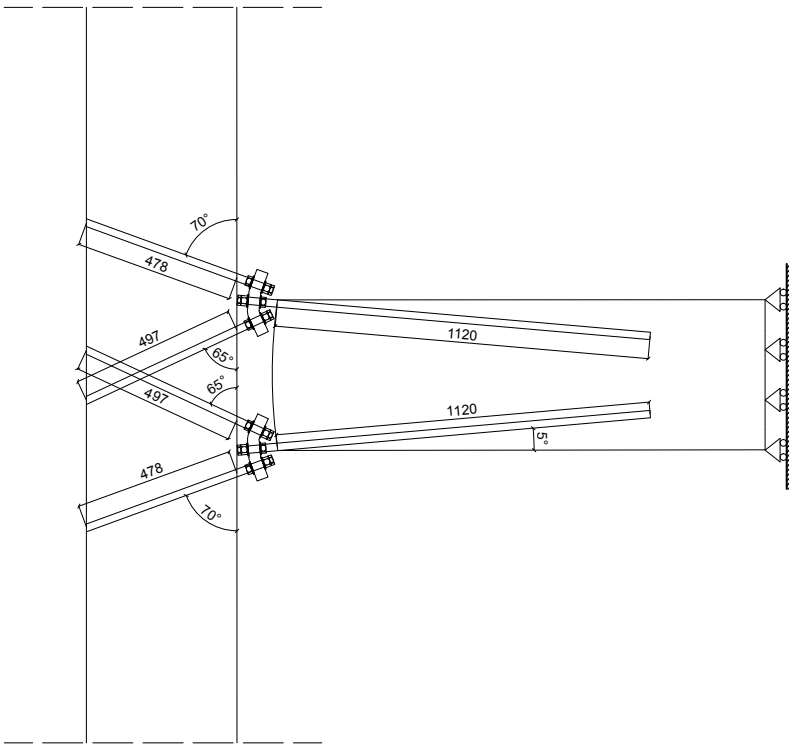

Figure 3.37: 65-70-05

The connection was able to sustain the loading, indicating that the configuration possesses fire resisting properties. It is important to emphasise that this property should be investigated further, e.g. by assigning a reduced modulus of elasticity in the charred section. The objective of the model in this thesis was mainly to investigate how the rotational stiffness is affected by locating the rods in different planes facilitated by a larger cross-section due to fire requirements.

As the illustration display, the connector and the free part of the rods are fully exposed. These have to either be applied a fire protective layer of coating, or insulated by use of e.g. timber, if this connection is to obtain fire resisting properties. It may also be discussed whether a rod inclination of 5 degrees in the beam is the most optimal considering the short distance to the timber surface.

4. Results

In this chapter the results from the numerical simulations will be presented in the following order; axial forces in the rods, rotational stiffness, stress state within the column and deflection of the beam.

4.1 Axial forces in the rods

The stresses in each rod were extracted from the numerical models. These were used to calculate the axial forces in the rods. The calculated forces were decomposed to the horizontal direction in order to control that the estimated forces were in equilibrium. Due to bending of the free part, the values were extracted from the outermost elements embedded in timber. A few configurations displayed bending also for these elements. In order to obtain an approximate equilibrium, the stresses were for these models extracted at either the second or third row of elements depending on the severity of the bending. At these elements the stresses were obtained from the integration points in the four elements at the centre of the rod in order to minimise the bending contribution.

The magnitude of the applied load was based on the load capacity from the experimental testing by Lied & Nordal. For 70-55-10 this was 66.2 kN. As the models utilise symmetry, and thus feature only one half of the connection, the applied load was set to P = 30 kN in order to avoid convergence issues due to failure. The experimental load capacity of 55-35-10 was 39.1 kN and the applied load was thus set to P = 18 kN. The new configurations have inclinations of 70 and 75 degrees and were therefore estimated to have a capacity closer to 70-55-10 than 35-55-10. Consequently these were also simulated with P = 30 kN to have a valid basis of comparison.

The results are presented in Table 4.1. The maximum axial force in the column rod is CL1 in 70-55-10 with a magnitude of 82.14 kN. Considering the percentage of the axial force in rod B, the highest are CL2 in 55-35-10 with 75.9 %. The corresponding value for 70-55-10 is 63.9 %

Comparing angles of 5 and 10 degrees of rod B there are some notable differences. An inclination of 10 degrees results in a marginally higher axial force in rod B, 2 % for 70-70 and 4 % for 75-70. In the column, a more horizontal angle results in an average reduction of 10.5 % and 9.3 % for rod CU1 and CL1 respectively, while the forces in rod CU2 and CL2 increase with 5.9 % and 3.9 %.

Table 4.1: Axial forces in the rods [kN]

Configuration	Zone	Rod C1	Rod C2	Rod B	Equilibrium[1]
55-35-10[2]	U	58.22	48.89	76.86	0.04
	L	58.38	46.98	76.92	−0.99
70-55-10	U	81.94	61.89	129.18	0.48
	L	82.14	61.61	128.65	0.96
70-70-05	U	59.13	79.78	130.09	0.94
	L	59.64	76.74	129.68	−1.04
70-70-10	U	66.58	74.31	133.31	1.11
	L	66.27	72.99	131.70	1.17
70-70-10	U	67.04	57.10	118.08	0.36
(h = 500 mm)	L	67.48	56.22	117.84	0.19
75-70-05	U	62.42	71.57	129.07	−1.04
	L	62.47	70.30	127.58	−0.69
75-70-10	U	69.16	68.58	133.89	−0.62
	L	68.24	68.43	133.10	−0.87

[1] Force equilibrium in the horizontal direction
[2] P = 18 kN

4.2 Rotational stiffness

The rotational stiffness of the different configurations were calculated by the equations derived in subsection 3.3.4. In each numerical model, $\delta_{x.u}$ and $\delta_{x.l}$ were extracted from the nodes displayed in Figure 3.32. The displacements in the z-direction, or horizontal direction, were used as the various $\delta_{x.u/l.column/beam}$. As seen in Table 4.2, the rotational stiffness from both numerical and analytical estimations indicates that a rod-to-grain angle of 5 degree results in a higher rotational stiffness. The difference in rotational stiffness, comparing 5 and 10 degrees in configuration 70-70, is in the range of 27.6 – 35.2 %. For configuration 75-70 with plate profile, the difference is in the range of 35.9 – 41.9 %.

Table 4.2: Rotational stiffness for different configurations [kN m/rad]

Connector	Model	Numerical	Analytical	Experimental
Circular	55-35-10	10 545	12 052	9 079
	70-55-10	13 813	14 263	7 603 (9 189[1])
	75-70-05	16 842	17 402	N/A
Plate	70-70-05	15 416	16 228	N/A
	70-70-10	12 470	12 001	N/A
	75-70-05	20 796	16 570	N/A
	75-70-10	14 649	12 188	N/A
	70-70-10 ($h = 500$ mm)	18 686	15 475	N/A
	65-70-05	18 733	16 156	N/A

[1] Digital Image Correlation measurements.

The configuration with the highest rotational stiffness, according to the numerical simulations, is 75-70-05. An increase in beam height, due to wooden slabs above and below the beam, indicates a favourable solution for the rotational stiffness.

4.3 Stresses in the column

In this chapter the stress states for a selection of configurations are presented. Due to the angle between the rods and the direction of the grains in the column, the relevant stresses are normal stress perpendicular to the grains and shear stresses. The stress states for these are presented for the two configurations that were tested experimentally by Lied & Nordal [2]; 70-55-10 and 55-35-10. Additionally, the configuration that, according to the numerical simulations, possesses the highest rotational stiffness, 75-70-05, is also examined. The stress states for the remaining configurations can be found in Appendix D.

For normal stresses, the upper limit is set to the mean strength as calculated by Lied & Nordal [2], $f_{t.90.mean} = 0.8\,\text{MPa}$, resulting in gray areas where this magnitude is exceeded.

Similarly, the upper limit for shear stresses is set to a mean strength $f_{t.v.mean} = 4.5\,\text{MPa}$, also calculated by Lied & Nordal [2]. Due to the extent of the areas that exceeds this magnitude in the negative direction, the lower limit is set to $f_{t.v.mean} = -5.5\,\text{MPa}$. This was done to avoid all black areas between the inner rods CU1 and CL1.

Additionally, both normal stress perpendicular to the grains and shear stress are plotted along various paths through the column width for all configurations. Only a selection of paths are presented in this chapter, as these should be sufficient for giving an indication of the distributions of stresses over the width of the column for the various configurations. Supplementary plots from other locations in the column can be found in Appendix D.

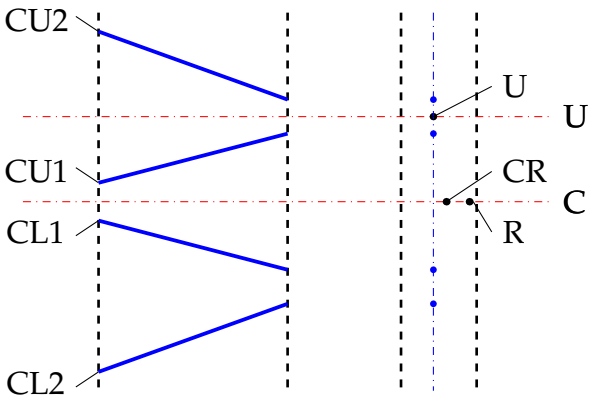

Figure 4.1: Various paths displayed as red lines

4.3.1 Stress states for selected configurations

70-55-10

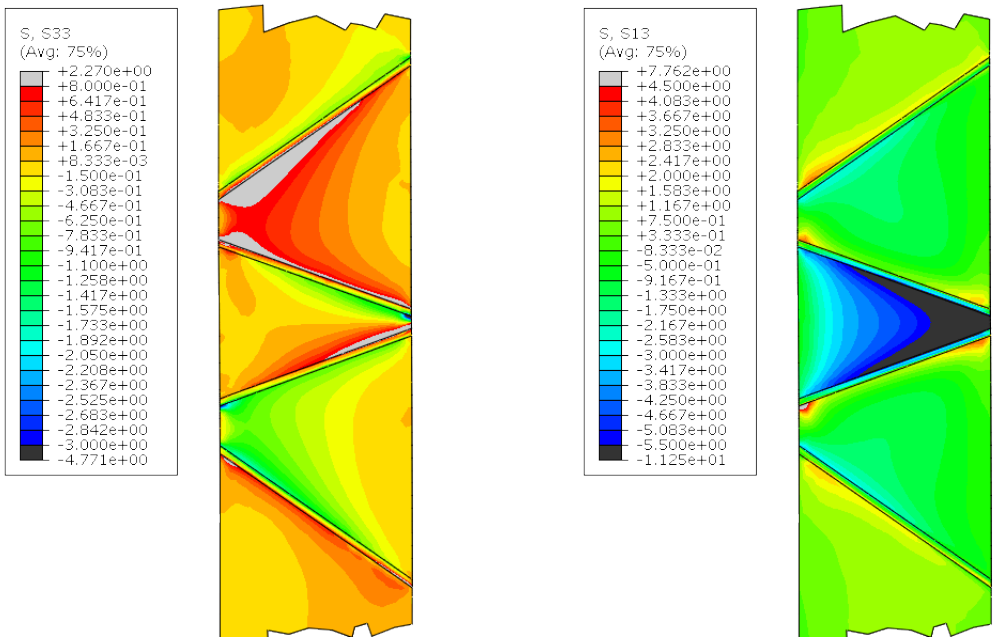

(a) Normal stress perpendicular to the grains (b) Shear stress

Figure 4.2: Stress state in the column for 70-55-10

Figure 4.2a displays a distinct tension zone between the two upper column rods CU1 and CU2. The area of maximum normal stress perpendicular to the grains are found above rod CU1 and below CU2. Additionally, there are local areas along the lower rods CL1 and CL2 that exceeds the mean strength above and below the respective rods.

The only shear stresses of a notable magnitude are between the two inner rods CU1 and CL1, as seen in Figure 4.2b. The maximum value is located where the distance between these two rods are the smallest, i.e. at the section furthest from the beam.

55-35-10

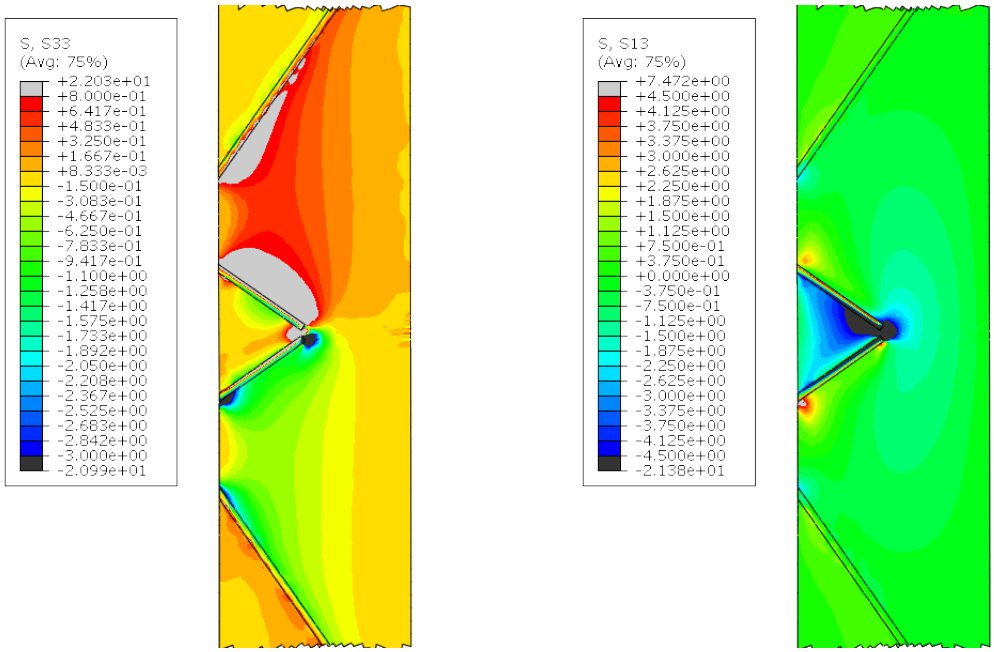

(a) Normal stress perpendicular to the grains (b) Shear stress

Figure 4.3: Stress state in the column for 55-35-10

The large space between the two upper rods, CU1 and CU2, results in a large tension zone where the stresses are of a magnitude close to the mean strength. Along these two rods, and especially CU1, the stresses exceed this limit as indicated by the grey areas in Figure 4.3a. However, except from where the two inner rods, CU1 and CL1, meet, there are no local areas exceeding the mean strength along the two lower rods, CL1 and CL2.

The inclinations that resulted in a large tension zone, results also in a correspondingly small shear zone between the two inner rods, CU1 and CL1. The maximum shear stresses are located where these two end in the midsection of the column.

75-70-05 with plate

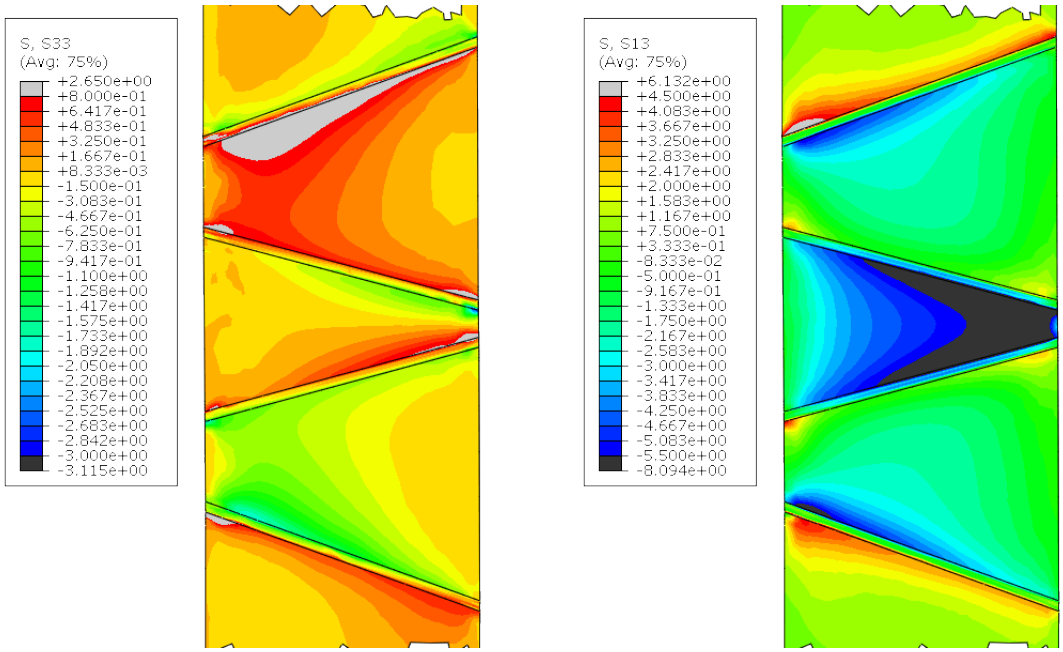

(a) Normal stress perpendicular to the grains (b) Shear stress

Figure 4.4: Stress state in the column for 75-70-05 with plate

The tensile stresses perpendicular to the grains exceed the mean strength below rod CU2. Additionally, there are local areas along the other rods, especially near the timber surfaces, displaying stresses of critical magnitude.

The shear stresses exceed the mean strength between the inner rods. Also for these stresses, there are local areas along the rods exceeding the capacity.

4.3.2 Comparison

Shear zone - right

Stress values extracted at the outer surface, 70 mm from symmetry line, are displayed in Figure 4.5 and Figure 4.6. Normal stresses have values of lower magnitude, between 0 MPa – 0.1 MPa, depending on the configuration and extraction point from column face. The shear stresses are of a higher magnitude, within the range of 3.3 MPa – 3.6 MPa. It follows a half circular path, as expected for the distribution of shear stresses in rectangular profiles.

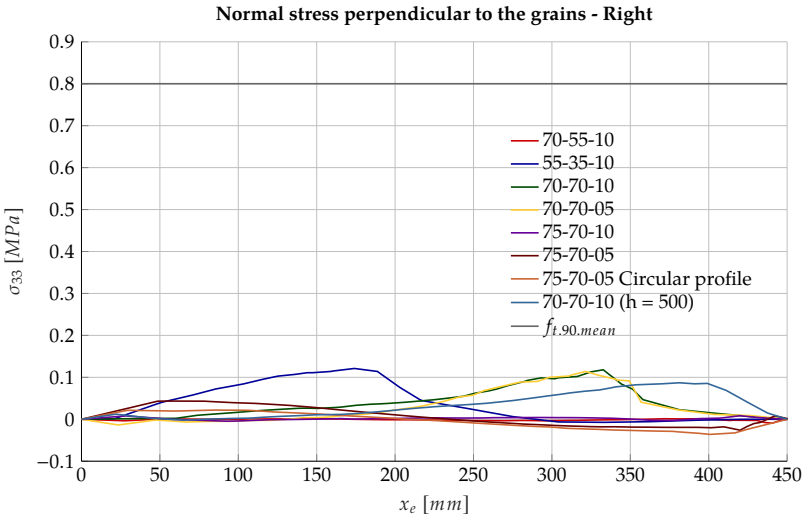

Figure 4.5: Normal stress (σ_{33}) distribution column

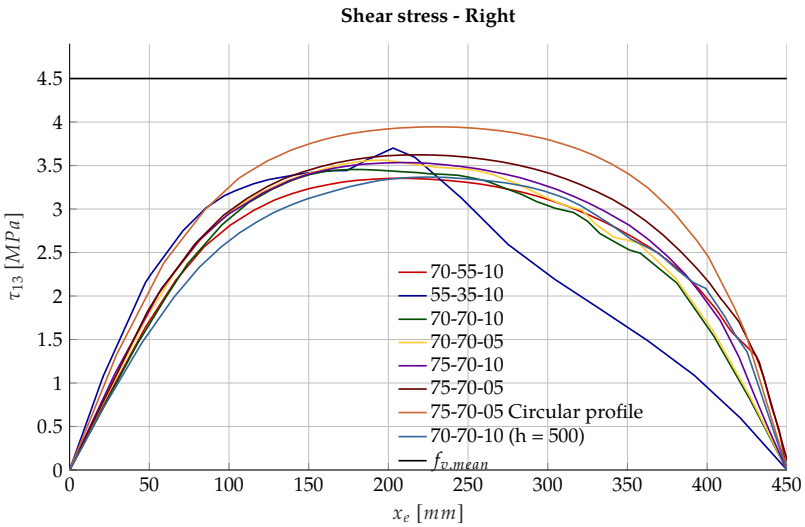

Figure 4.6: Shear stress (τ_{13}) distribution column

Shear zone - centre-right

The stress values extracted at distance 45 mm from symmetry line, corresponding to the right of the centre lines of the rods, are within the same range as stresses extracted at outer face. As seen in Figure 4.7, for configurations where the inner rods, CU1 and CL1, do not meet, the normal stress variation is not significantly higher than stresses extracted at outer face. For the other configurations, there are local stress peaks where the inner rods end. The shear stresses within the column, see Figure 4.8, increases slightly, and range from 4 MPa to 4.5 MPa. Due to local disturbance from the inner rods, that do not penetrate the entire column, there are local stress peaks.

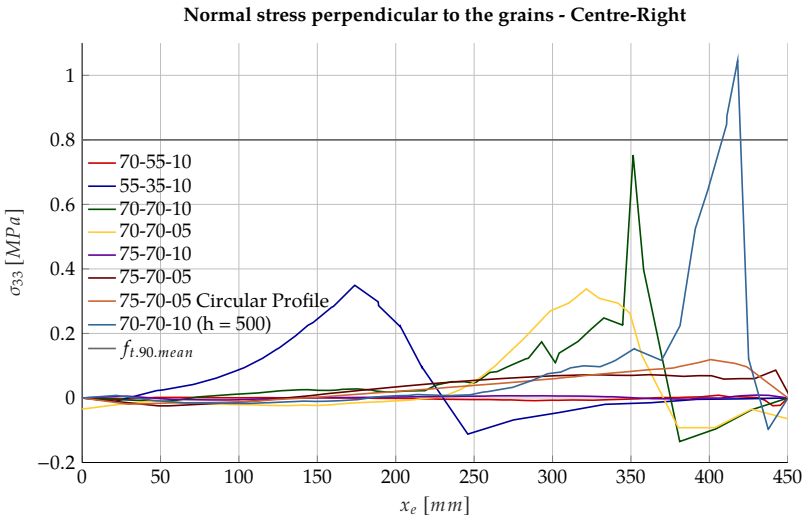

Figure 4.7: Normal stress (σ_{33}) distribution column

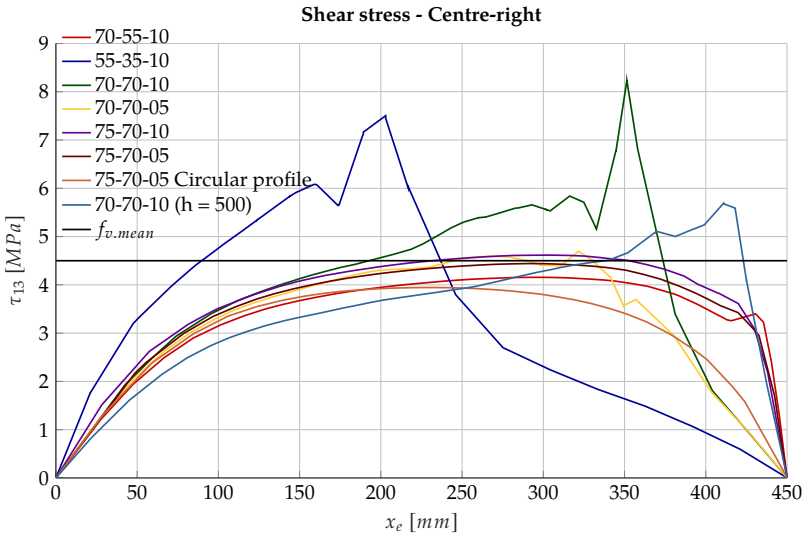

Figure 4.8: Shear stress (τ_{13}) distribution column

Tension zone

In the tension zone, the stress distribution differ from the centre line, the normal stresses have a higher magnitude, and range from 0 MPato1.3 MPa depending on the configuration and extraction point. As seen in Figure 4.9, all configurations, except 70-70-10/05 and 55-35-10, have a peak value of ~ 0.8 MPa. Shear stresses along the same path peaks at a distance approximately 50 mm from the column surface. The peak value range from 0.5 MPa − 3.6 MPa, depending on the configuration.

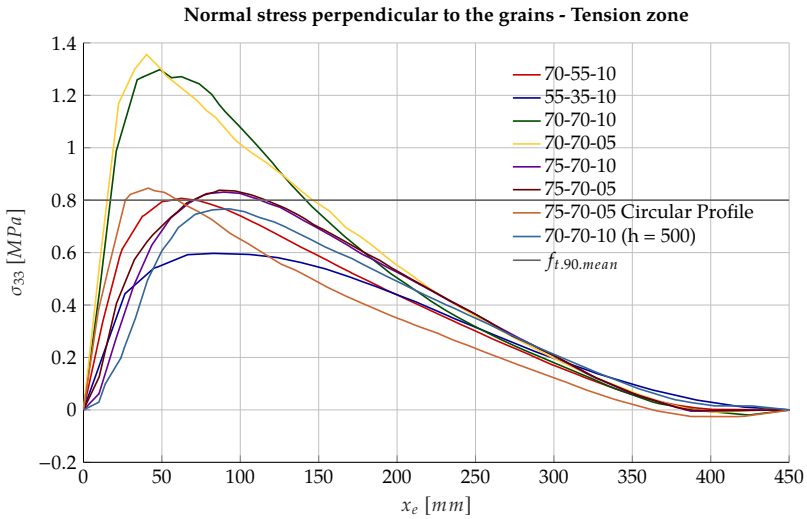

Figure 4.9: Normal stress (σ_{33}) distribution column

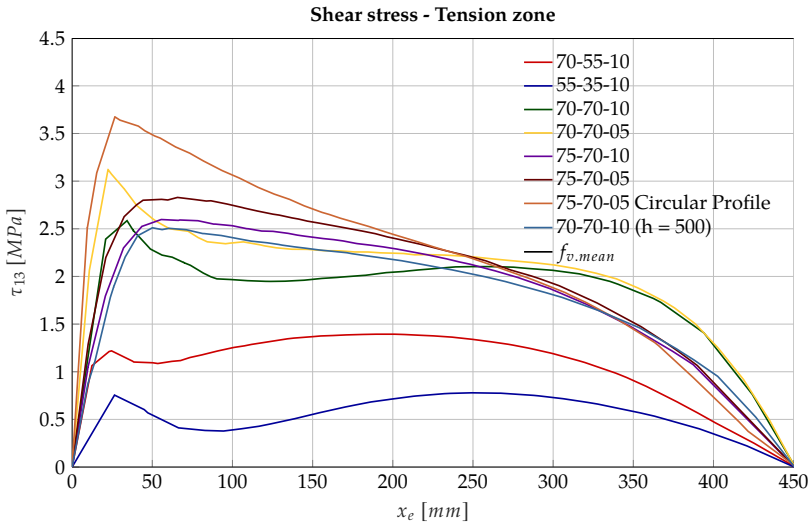

Figure 4.10: Shear stress (τ_{13}) distribution column

Configuration based on fire requirements

The stresses in the tension zone were extracted below rod CU2 in alignment with the centre line of the rod. Due to the two inner rods, CU1 and CL1, in different planes, the stresses in the shear zone were extracted in the middle of these planes at a horizontal distance of 16 mm from either centre line.

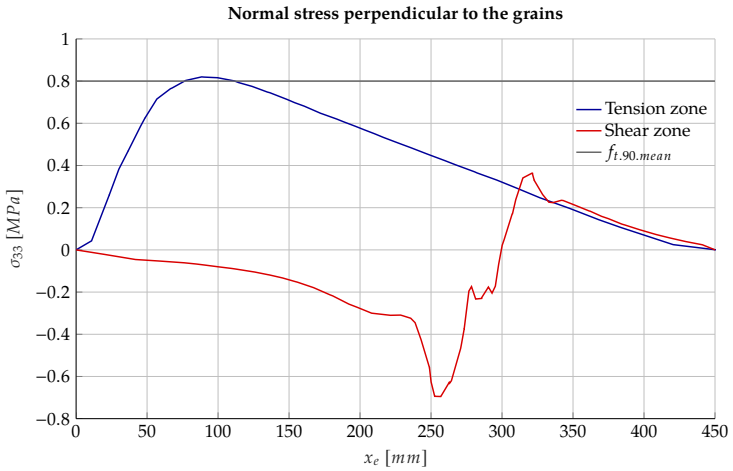

Figure 4.11: Normal stress (σ_{33}) distribution column

The normal stresses in the tension zone are very similar to the other configurations, with a peak at ~ 90 mm of a magnitude similar to the mean strength. In the shear zone the normal stresses act as compressive stresses to a depth of 300 mm, where they change to tensile stresses.

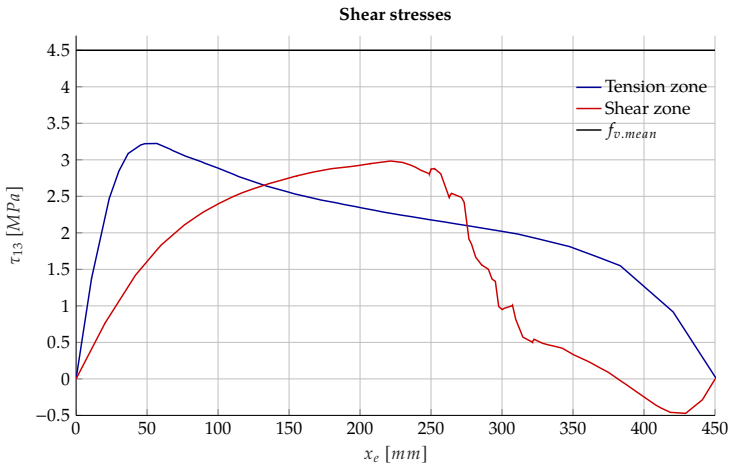

Figure 4.12: Shear stress (τ_{13}) distribution column

The shear stresses in the tension zone follow a similar path as the other configurations possessing an inclination of 70 degrees in rod CU2 . In the shear zone the stress distribution is parabolic to a depth of ~ 250 mm where fluctuation starts. The maximum value in both zones is lower than the mean strength

4.4 Deflection of the beam

To evaluate the stiffness of the connection, deflection at beam tip may be of interest. The deflection is extracted at centre of beam height, at the loading point. As seen in Table 4.3, the deflection of the beam is within the range of 29 mm – 38 mm. The configuration with the smallest deflection is 70-70-10, with a beam height of $h = 500$ mm. The highest is configuration 70-70-10, with a beam height of $h = 450$ mm.

Table 4.3: Deflection middle of beam, at loading point

Connector type	Configuration	Deflection [mm]
Circular	55-35-10	21.6
	70-55-10	33.8
	75-70-05	34.7
Plate	70-70-05	35.9
	70-70-10	38.1
	75-70-05	32.7
	75-70-10	35.4
	70-70-10 (h=500)	28.8
	65-70-05	30.0

5. Evaluation

In this chapter the results presented in chapter 4 will be evaluated and compared to results from analytical calculation methods, experimental testing, and alternative modelling techniques. Additionally, an evaluation of the methods for obtaining the results will be performed.

5.1 Numerical modelling

This section evaluates the modelling techniques, input parameters and constraints applied in the numerical models.

5.1.1 Withdrawal properties

To reproduce a complete configuration, the simulation of rod-wood interaction is essential. Due to limited computing capacity, a reduction in number of elements was desirable. Therefore a simplified modelling technique, that could reproduce withdrawal properties of threaded rods would be advantageous. In this thesis, the use of cohesive surface has been applied to simulate withdrawal. When evaluating the rotational stiffness of the configuration, the ability to reproduce withdrawal is therefore essential.

Numerical model

Deviation of withdrawal stiffness from numerical to experimental, as seen in Figure 3.19, was experienced for shorter embedment lengths and larger angles. Angles between $60 - 90$ degrees are widely used in the various configurations, and a reduction in withdrawal stiffness will influence the rotational stiffness. This reduction may be a result of the simplifications made in the numerical model.

The main difference between the experimental set-up and numerical model, is the neglecting of threaded part at rod face and the absence of the steel plate at the top face of the wooden part. Neglecting the threaded part of the rod may influence the stresses along the rod, in a local manner. However the withdrawal stiffness is achieved for nearly all specimen. The effect of the 5 mm steel plate on the withdrawal stiffness would not be of significance. This plate was used to counteract bending

stresses and prevent tensile splitting failure, but also allowing local deformation on the surface of the specimen in the vicinity of the rod.

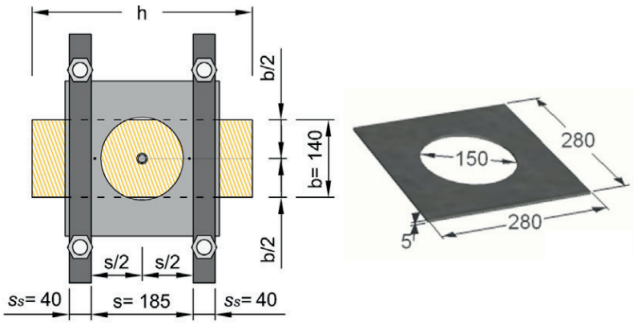

Figure 5.1: Steel plate placed between the supports and specimen

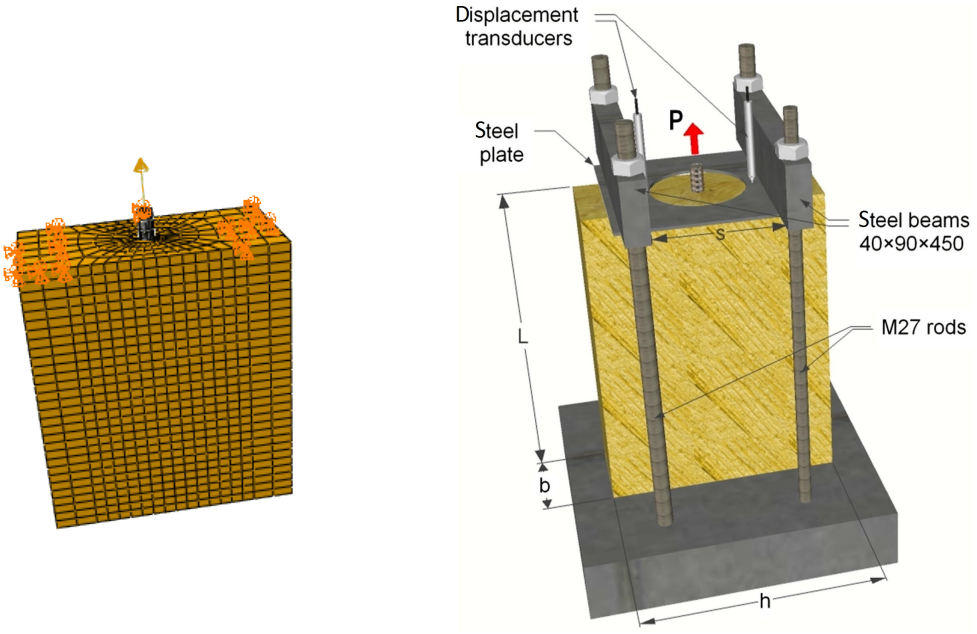

(a) Cohesive withdrawal model

(b) Experimental set-up

Figure 5.2: Difference between cohesive model and experimental set-up

The material values used in this model, see table Table 5.1, were identical to the values used in the numerical simulations by H. Stamatopoulos [10]. The reason was to have a valid basis for comparison between the different modelling techniques. An experimental study on Norwegian spruce, by Kristian B. Dahl, gives the values of $E_{RR} = 800\,\text{MPa}$ [27]. This could explain the reduced withdrawal stiffness in the RR direction, as this is the most relevant direction for larger inclinations. A withdrawal test of specimen with a rod-to-grain angle of 60 degrees and embedment length of $l = 300\,\text{mm}$, with $K_{tt} = 58.25$ and $E_{RR} = 800\,\text{MPa}$, results in $K_w = 77.8\,\text{N/mm}$, an increase from $K_w = 60\,\text{N/mm}$. As seen, different material properties may give a better estimation of the cohesive values and withdrawal stiffness, thus a better withdrawal model.

	E_{LL}	E_{RR}	E_{TT}	G_{LR}	G_{LT}	G_{RT}
Numerical properties	13000	410	410	760	760	30
Norwegian spruce	10700	800	400	600	600	30

Table 5.1: Material properties [MPa], numerical model and experimental values [27]

Withdrawal values

A sensitivity study was performed to evaluate the influence of K_{nn}. As seen in Table 3.4, the influence is of minor importance when the rod is subjected to a vertical force. The influence of K_{nn} was not studied in specimens with an angle that differ from 90 degrees. The withdrawal experiment performed by Grytting & Sæle [13] could therefore be of relevance to evaluate the withdrawal of a rod subjected to axial and lateral loading, using cohesive surface. The use of $K_{tt} = K_{ss}$ is also believed to be of smaller relevance as the withdrawal act in the same direction in both the column and the beam and the only difference is the inclination.

The influence of mesh size was evaluated, see Table 3.4. As seen, the influence, within the range 2 to 10 mm, is of minor relevance, as the difference in withdrawal stiffness is small. The use of 10 mm is a good value of mesh height, as the difference is small and the computational time would increase greatly if a height smaller than 10 mm was used in the models of the entire connection. A mesh height larger than 10 mm could influence the stress output in the column, as there would be fewer elements to represent the stresses. Therefore a larger element height than 10 mm would not be beneficial.

A cohesive value of $K_{tt} = 58.25$ was used in the numerical simulations. Correlation was then obtained for lower angles and larger embedment lengths. As seen in Figure 3.20, the cohesive values do not give a clear regression curve for the different rod-to-grain angles and embedment lengths. Therefore the use of a general formula, as Hankinson's formula, would not be beneficial to represent the values. $K_{tt} = 58.25$ was found by the use of mean values for each angle, where values from each embedment length were used. As seen, in Figure 3.20, the values found at embedment length $l = 300$ mm were significantly higher for some angles. Values found at this length could be excluded, to see if a lower mean value could give equivalent results.

5.1.2 Connector

Numerical simulations were utilised in order to optimise the design and dimensions of the connecting steel part. Various definitions and constraints were imposed in these models which have great significance for the results.

Numerical model

Evaluation of the steel connector was performed by modelling a small section of the full connection. A complete model is preferred in order to correctly replicate the behaviour of the connector. However this is more demanding, both considering time and computational capacity. Due to a simplified model, various techniques were utilised to reproduce the features of a more comprehensive model and to solely evaluate the connector.

The loading was decomposed in the horizontal and vertical directions. The horizontal force was applied at the centre of the intersection between the rods and the beam at the surface facing away from the connector. In reality, the correct location may rather have been at the surface facing the connector. Due to the small width of the beam component (25 mm), this is assumed to have minor importance for the results, especially considering this location was consistent for all models.

The magnitude of the applied load was 10 % of the estimated maximum load calculated by Lied & Nordal, resulting in very small differences between the various configurations. Forces of a higher magnitude may have been helpful in separating the configurations and expose strengths and weaknesses, especially regarding failure modes. As the main focus is the rotational stiffness, it was decided to evaluate this parameter in several configurations rather than several parameters of few configurations.

Both timber components were defined as rigid bodies in order to solely evaluate the steel connector. By removing e.g. withdrawal from the model, the remaining parameters are the dimensions and material properties of the steel parts. Additionally, by not featuring the bending of the timber components due to the compression and tension forces in the rods, the differences in location of the rods due to different connector types and configurations were not evaluated.

The rods were connected to the timber components using tie constraints, making them behave as cantilevers. In reality, the softness of the wood surrounding the rod may be considered to prolong the length of the part that can be considered as a cantilever. This is however consistent with the definition of free length as described

in the component method in subsection 3.1.2. Both rods and steel connector were merged to one part, making the interaction stiffer than in reality. As this was consistent for all models, this definition is presumed to be of minor importance.

The definition of rigid body and tie constraints enable the opportunity of assigning a fairly fine mesh of the steel part without increasing the computational time significantly. Global seeds of 3 mm were assigned to both rods and connector for all models. Due to the small element size, and the relative performance of the various configurations as the main interest of these simulations, it was not performed a sensitivity study of various meshes.

Rotational stiffness

All values are assumed to be considerably higher than in reality due to the definitions and constraints previously described. They do however give an indication of the relative performance of the various configurations.

The configuration possessing the highest rotational stiffness was 70-70-05. This was 11.4 % stiffer than the similar 70-70-10. The reason being the shorter free length of the beam rod. This is also why 45-45-10 performed so poorly. The free length of the column rods in this configuration were 97 mm and 85 mm, whereas the corresponding dimensions for 70-70-10 were 55 mm and 51 mm.

These results indicate the importance of the free length of the rods. The free length of rod BU in the beam is slightly reduced with increasing rod-to-grain angle of rod CU1. The reason is that the plate becomes more levelled at larger angles, thus reducing the space needed to fasten rod CU1. This is illustrated in Figure 3.25.

In order to evaluate the performance of the steel plate, it is of most relevance to consider the circular profile and the plate with an identical combination of inclinations, as displayed in Figure 3.28b. Despite the greater free lengths, the plate with a thickness of 35 mm exhibited an increase in rotational stiffness of 39.8 % compared to the circular profile.

The vertical displacements of the models with the steel plates are nearly identical. As the only difference was the rod inclinations, this was expected. The most interesting observation is that these displacements are approximately half the magnitude of the vertical displacement of the circular profile.

5.1.3 Models of configurations

The calculation of rotational stiffness is, in this thesis, dependent on the accuracy of the numerical model. A comparison between experimental and numerical rotational stiffness, reveal that the numerical model is too stiff. This may be a combination of the simplifications in the numerical model, like the steel part, and the numerical parameters, as withdrawal properties.

Simplifications made in the different parts within the model, including column, beam and steel connector, may exhibit higher stiffness than a physical part. The numerical steel part contain various simplifications. In the experimental testing, this was assembled by several separate parts, as circular steel profiles and threaded rods connected together with the use of bolts and nuts. As seen in Figure 5.3, the nuts are not included in the numerical model, instead the rod is merged with the steel profile, as one part. Therefore the interaction between the rod and profile is fully rigid. This may be a valid simplification, as the nuts when tightened, could withstand some local rotation. The free length of the rod is somewhat decreased. In the experimental testing, the upper circular profile, where the entire rod is subjected to tension, the free length would be measured from the outer nut, as this resist translation. In comparison to the numerical model, where the free length is measured from the outer face of the circular profile, there was a somewhat smaller distance than in the corresponding physical part. Only a small percentage of the increased stiffness in the numerical model may be contributed to this simplification, and it is desirable to enlighten other sources to the increased stiffness. For the lower profile, the inner nut is withstanding translation, and the numerical model would be a good simplification.

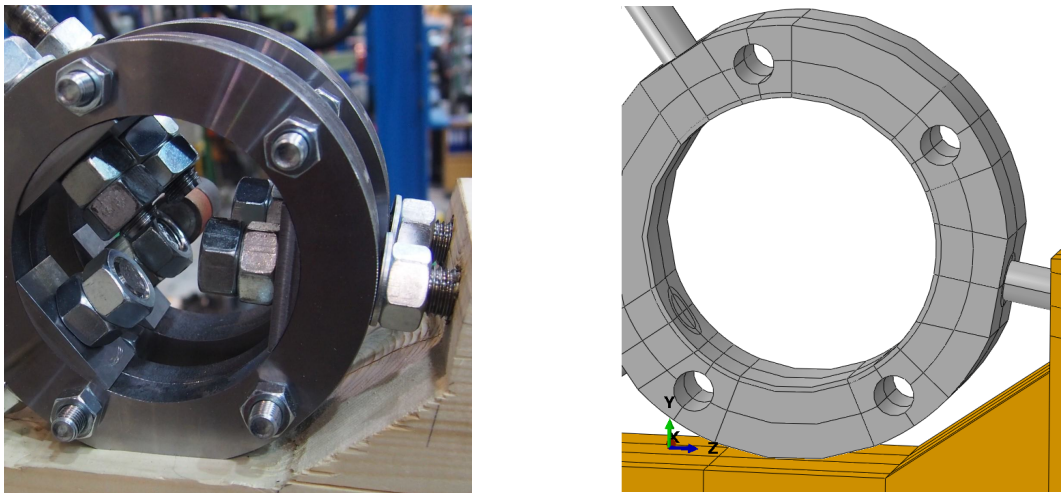

(a) Profile with nuts (b) Profile without nuts

Figure 5.3: Difference between numerical and experimental profile

The withdrawal stiffness parameters have a considerable influence on the rotational stiffness, as these parameters and the steel connector is the tie between the column-to-beam interaction. The use of a different Young's modulus, as $E_{RR} = 800\,\text{MPa}$, would affect the withdrawal stiffness properties and result in a reduction in $K_{tt} = K_{ss}$. The consequence may be a reduced rotational stiffness in the configuration model. To replicate the experimental testing, rods with $d_{inner} = 16.13\,\text{mm}$ were used. This differ from the experimental withdrawal testing performed H. Stamatopoulos, where $d_{inner} = 15.00\,\text{mm}$ was used [10]. An increase in the rod diameter would increase the interaction area between rod-wood, and may increase the withdrawal stiffness. Therefore a reduction in $K_{tt} = K_{ss}$ is desirable.

As for the numerical model, the wooden plastic properties are not included. This may also result in a reduced stiffness for higher load levels, but not within the elastic area. Another consequence could also be a better distribution of stresses within the wood, as the peak stresses would be smeared out due to the plastic properties.

5.2 Results

In this section, the results presented in chapter 4 will be evaluated and compared to analytical calculation methods where available.

5.2.1 Axial forces in the rods

According to the estimated distribution of forces calculated in subsection 3.1.1, 70-55-10 should possess an approximately even distribution. This is not validated by the numerical model as the axial force in rod CU1 is 63.4 % of the force in rod BU, while the percentage for rod CU2 is 49.7 %.

The most even distribution is 75-70-10 where all the forces are ~ 50 % of the force in the beam rod. The analytical estimation resulted in a distribution of 39 % and 61 % for CU1 and CU2 respectively. Interestingly, 75-70-05 had a distribution of 48.4 % and 55.5 % in the numerical models. It seems that decreasing the inclination of rod B results in an more uneven force distribution in the column rods, at least for the selected configurations. Consequently, if an angle of 5 degrees is desired due to the lower axial force, there are two alternatives in obtaining an even force distribution. Either align rod CU1 even more horizontally, or reducing the rod-to-grain angle of rod CU2. A configuration somewhere between 70-55-10 and 75-70-05, e.g. 70-60-05 would have been interesting to examine.

It is important to emphasise that the procedure of obtaining the axial force contains several variables, especially regarding the selection of elements to extract the stresses from. A finer mesh of the rods may have enabled extraction of stresses at the same location in each model, as the distortion of elements due to bending would have been reduced.

5.2.2 Rotational stiffness

Configuration 55-35-10 have a significant lower rotational stiffness than 70-55-10. The experimental results indicate that the rotational stiffness in reality is higher. The measured withdrawal stiffness for higher angles and smaller embedment lengths, was, as mentioned in subsection 3.2.2, at a lower magnitude than measured in the withdrawal experiment. As seen in Appendix C, configuration 55-35-10 have rods with both small embedment length, l = 250 mm, and a smaller angle of 55 degree. If the rod CU1, in configuration 55-35-10, was to be pulled out before rod CU2,

the combination of free length and lateral loading for rod CU2 would significantly reduce the rotational stiffness.

Both the numerical simulations and the component method indicate that a configuration with larger angles, would have given a higher rotational stiffness. Also the use of an inclination of 5 degrees for the beam rod is favourable. The configuration with the highest rotational stiffness, for both the numerical simulations and the component method, is 75-70-05. The increase in stiffness from 70-55-10 to 75-70-05 is in the range of 16.2 – 50.5 %. If the stiffness of 70-55-10, measured in the experimental testing, is used as a reference value, the increase in numerical stiffness would result in a experimental stiffness in the range of 11 404 kN m/rad – 13 783 kN m/rad. Measurements from both the DIC and sensors are utilised as a reference rotational stiffness value. These magnitudes result in an acting moment corresponding to $\sim$ 80 % of a fully rigid connection.

Increasing the beam height to $h = 500$ mm, indicates a favourable solution for the rotational stiffness. A comparison between the configurations 70-70-10, with a beam height of $h = 450$ mm and $h = 500$ mm respectively, results in increase of stiffness in the range of 28.9 – 49.8 %. The percentages are based on values from both the component method and numerical results.

5.2.3 Stresses in the column

In this section the stress states presented in section 4.3 will be evaluated and comparisons between the various configurations will be made.

70-55-10

The stress states display a distinct tension zone between the two upper rods, CU1 and CU2, and a shear zone between the two inner rods, CU1 and CL1. It is in these zones that the stresses reach a critical magnitude. Additionally, there are local areas with normal stress perpendicular to the grains above the mean strength along the two lower rods, CL1 and CL2. Especially the area above CL1 is critical, as this is also the location for maximum shear stresses.

Lied & Nordal provided a recording of the experimental testing of this configuration, displaying the crack propagation in the column [2]. Although the largest shear crack was located at the centre line of the column, the recording shows that the initial cracking originated closer to the entry point of the rods, as illustrated in Figure 5.4a. This crack propagation is explained by the stress state in Figure 5.4b displaying the

largest normal stresses perpendicular to the grains at the same location as the initial cracking.

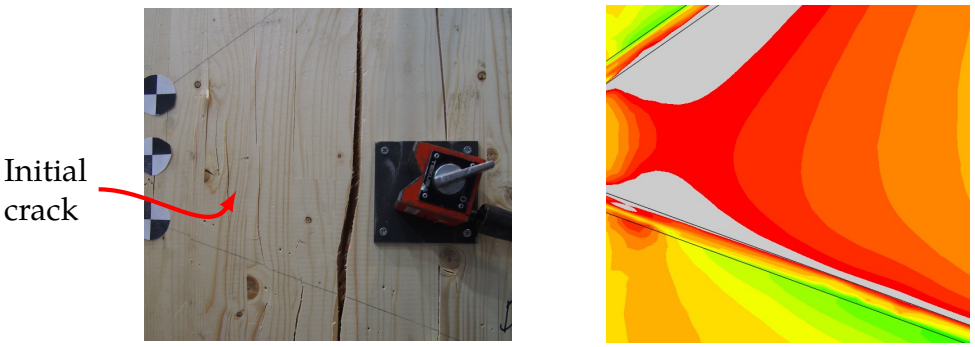

(a) Crack propagation (b) Stress concentration

Figure 5.4: Cracks in the column in experimental testing of test 4 (corresponding to 70-55-10) by Lied & Nordal and visualization of stress concentration from numerical simulation

55-35-10

This configuration possess the smallest rod-to-grain angles in the column, resulting in the largest space between the two upper rods, CU1 and CU2. Due to the large tension zone, the areas exceeding the mean strength are also correspondingly large. Especially the size of the area above rod CU1 indicate normal stresses perpendicular to the grains of a critical magnitude over the entire embedment length. This can explain the low capacity experienced in the experimental testing [2].

The consequence of a large tension zone is a correspondingly smaller shear zone. In this configuration the two inner rods, CU1 and CL1, end at the midsection of the column in close proximity of each other. Naturally, due to rod CU1 in tension and CL1 in compression this is the location for the maximum shear stresses.

75-70-05

The normal stresses perpendicular to the grains reach a critical value below rod CU2. Where the two previously evaluated configurations displayed significant areas exceeding the mean strength above CU1, this configurations do not, apart from minor, local areas near the column surfaces. The more horizontal alignment of rod CU1 may be a reasonable explanation.

In the shear zone displays this configuration the lowest magnitude of shear stresses. It seems that a larger rod-to-grain angle of the inner column rods, CU1 and CL2, lead to reduced normal stresses near these rods and lower maximum shear stresses.

Comparison of stresses in the shear zone

For the graphs displaying the distribution of stresses near the outer edge of the column, it is mainly the shear stresses that are of a significant magnitude. From the previously evaluated stress states, this is expected. All configurations are nearly identical. The only discrepancy is the 55-35-10 where the curve alternate from parabolic to approximately linear at a depth of ~ 200 mm. This corresponds to the location of where the inner rods, CU1 and CL1, end. A similar disturbance may be observed in the curves belonging to 70-70-10 and 70-70-05 at a depth of ~ 200 mm where also the inner rods end inside the column.

The graphs displaying the stresses closer to the centre line of the column show significant normal stresses perpendicular to the grains for a few of the configurations. Common for these, are that the inner rods CU1 and CL1 do not penetrate the entire column. The peaks in the graphs correspond to where these rods end. Similar peaks are observed in the graphs displaying the shear stresses. The relative location of these are maximum tensile stresses in front of the rod ends, followed by maximum shear stress at an approximate location corresponding to the intersection of the longitudinal axes of these rods. This tendency is corroborated by e.g. Figure 4.3 displaying the stress states for 55-35-10. For the other configurations, the maximum shear stresses are located at a similar magnitude as the mean strength at a depth of 225 mm to 360 mm. Among these configurations, 70-55-10 displayed the overall lowest shear stresses, while the 75-70-10 and 75-70-05 with the circular profile exhibited the largest. The reason may be the closer distance between the inner rods, resulting in shear stresses exceeding the mean strength at a shorter distance from the column surface.

The configuration designed based on fire resistance, 65-70-05, has the inner rods, CU1 and CL1, in different planes. Where these rods cross each other, corresponds to the disturbance of the curve displaying the normal stresses in the shear zone. The negative peak is located where the intersection starts at ~ 250 mm, and the positive peak at ~ 310 mm coinciding with the end of the crossing rods. The magnitude of the negative stresses is higher than the positive, which is favourable considering the higher mean strength of glulam for compressive stresses than tensile stresses. Fluctuations in the curve displaying the shear stresses may also be observed in the same area as the normal stresses. The configurations where the two inner rods do not completely penetrate the column, experienced stress peaks. This do not occur for 65-70-05. Instead, crossing of the rods seems to reduce the maximum value of the shear force as the parabolic section of the curve is still rising at the point where the fluctuation starts. Of the configurations with a column width of 70 mm, 75-70-05, with the circular profile, possessed the lowest maximum shear stresses of

~ 4 MPa. As seen in Figure 4.12, 65-70-05 displays shear stresses of a considerably lower magnitude.

Comparison of stresses in the tension zone

The maximum magnitude of normal stresses perpendicular to the grains are located at a distance of 50 mm to 75 mm from the column surface for all configurations. This is consistent with the stress states which display a larger area of stresses exceeding the mean strength at this location. The configuration exhibiting the lowest maximum tensile stresses is configuration 55-35-10 with the smallest rod-to-grain angle of rod CU2. Due to the inclination, the area of maximum stresses is shifted upwards as it increases perpendicular to the longitudinal axis of the rods. The consequence is that the path of extraction is too far from the rod in order to display the area exceeding the mean strength. Altering the path for this configuration was discussed, but it was ultimately decided to keep the original to be consistent with the other configurations.

The configurations with column rod inclinations of 70-70 and $h = 450$ mm differs from the others by exhibiting maximum tensile stresses of ~ 1.3 MPa, whereas the remaining configurations peaks at magnitudes corresponding to the mean strength of 0.8 MPa. By examining the stress state of 70-70-10 in Figure D.1a, the area exceeding the mean strength is extremely large compared to 75-70-10. It seems that the ending of the two inner rods inside the column results in several local disturbances along the rods, ultimately leading to a stress concentrations near the column surface. These fluctuations along the rods can be observed in all configurations where the inner rods do not penetrate the entire column width, although they are not as distinct for 55-35-10. Measures were attempted in order to remove the stress fluctuations, but none were successful.

The shear stresses are as expected below the mean strength, in tension zone, for all configurations. The 75-70-05 configuration with the circular profile exhibits the highest stresses explained by the shortest distance between the upper rods. The configurations with the smallest rod-to-grain angles, 70-55-10 and 55-35-10, display the lowest stresses. By examining the stress states for these configurations it was evident that the combination of smaller angle and large distance between the upper rods results in lower shear stresses. Configurations possessing an even larger distance than 70-55-10, e.g. 75-70-05, display shear stresses of a notable magnitude along the upper rod CU2. Consequently, it may be assumed that the governing parameter regarding the magnitude of shear stresses in the tension zone, is the inclination.

As expected the stresses in the configuration designed based on fire resistance, 65-70-05, do not differ considerably from the other configurations in the tension

zone. The curve displaying the normal stresses follows a similar path with a peak at ~ 90 mm and a magnitude similar to the mean strength. The distribution of shear stresses is also similar, but has a maximum value of a higher magnitude than the majority of the others. The very similar configuration 70-70-05 exhibits the maximum value, but at a shorter distance into the column. The curve also declines with a faster rate to a distance of ~ 250 mm where the two curves coincide. The distance between the two upper rods is shorter in 70-70-10 due to the larger angle of rod CU2 which seems to effect the shear stresses near the timber surface.

5.2.4 Deflection of the beam

The maximum deflection measured at centre height of the beam at the loading point was for the configuration 70-70-10. The deflection measured at this point was $w_{beam} = 38.1$ mm. The configuration with the lowest deflection was 55-35-10, $w_{beam} = 21.6$ mm. However, as this configuration was only loaded with $P = 18$ kN, configuration 70-70-10, with increased height, have the lowest comparable deflection of $w_{beam} = 28.8$ mm. As seen in Table 4.3, the difference between the circular and plate profile is small. Configuration 75-70-05 has a deflection of $w_{beam} = 34.7$ mm and $w_{beam} = 32.7$ mm, with circular and plate profile respectively. As seen in Table 4.2, configuration 75-70-05 with circular profile have a reduced rotational stiffness compared to the configuration with plate, and may account for the increased deflection measured at beam tip.

5.3 Connector

This section will evaluate the properties of the steel connector not related to the numerical modelling, as these are elucidated in subsection 5.1.2

5.3.1 Design

The final design of the connector did not have the desired reduction in height which was mentioned when evaluating the circular profile in section 3.3. The horizontal dimension in side-view however, was considerably reduced as illustrated in Figure 5.5.

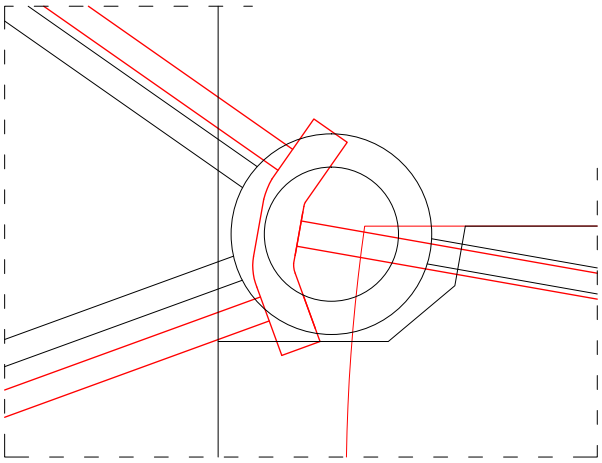

Figure 5.5: Illustration of the dimensions of the new connector compared to the circular profile

The new connector requires that a considerable part of the beam has to be removed, resulting in no direct beam-to-column contact. The experimental testing performed by Lied & Nordal indicated that the contribution of the timber-timber-interaction to the rotational stiffness was very small [2]. This is corroborated by the numerical simulations which were performed without timber-to-timber contact. Consequently, this should not negate the potential increase in rotational stiffness due to the change in profile.

During the evaluation of the rotational stiffness of the various connectors, it was observed that the free lengths of the rods have great significance for the rotational stiffness. The limiting factor for these, using the new connector, is the required spacing in order to fit nuts on the rods. In the design procedure described in section 3.3, it was assumed that two nuts with a height of 15 mm each on the tension side are necessary. As the space for these are the limiting factor for the free lengths, it

may be worth investigating if two nuts really are needed. In test 4 by Lied & Nordal it was only used one nut for one of the column rods, without being a limiting factor in the experimental testing. However, considering the dimensions and magnitude of the acting forces in this connection, it is presumed that two nuts or a single one of larger dimensions are needed, especially when taking long-term effects into account. A consequence is that the free lengths used in the models in this thesis can not be reduced.

5.3.2 Assembly

The main concern regarding the new steel connector is the assembly. The connection is designed to be a part of moment resisting frames up to 10 storeys. These are constructed as continuous columns and the beam/slab would thus need to be lifted into position. The connector functions as the sole part connecting the beam to the column through the threaded rods. Consequently a simple assembly of the connector results in an uncomplicated assembly phase for the entire connection. Paramount in achieving this, is to design the connector to allow for deviations. These may originate from imprecise screwing angle, inaccurate location of the rods and incorrect length of these.

The problem for a design to allow for deviations, is the reduction of stiffness. By designing the holes for the threaded rods excessively large to account for inaccurate alignment of the column and beam rods, these would be free to move inside the holes. Ultimately the plate was designed with holes for the rods of a diameter of 22 mm similarly to the design of the circular profile by Lied & Nordal, where an engineering deviation of 1-2 mm was specified [2].

By cutting the plate in half and use fastening bolts perpendicular to the rod axes enables an uncomplicated assembly phase. This principle was used for the circular profile and worked satisfactory in the experimental testing by Lied & Nordal [2]. There are some uncertainty regarding the location of the holes for the fastening bolts. Presumably, two in the inner gaps between the rods are needed in order to tighten the two halves sufficiently. This is not desirable considering that the arches of the plate are the locations of maximum bending stresses due to the tension and compression forces in the rods. However, the dimensions of the plate are chosen in order to achieve high stiffness, and as a consequence presumably possess a capacity of sufficient magnitude that the removal of steel in these areas do not present a problem.

The alternative of letting the holes for the column rods extend to the top of the plate seems favourable as the connector then would be a single part. The weakness of this design is the removal of timber surrounding the beam rods, prolonging the free length of these. Results from both numerical simulations and the analytical estimations have indicated the importance of keeping the free lengths as short as possible. Presumably, prolonging the free length may negate the gain in stiffness due to having the connector as a single part. Consequently, this alternative does not seem to be the best option.

Due to the dimensions of the steel connector, a ductile failure mode seems improbable. However, the numerical simulations indicated highest stresses in the beam rods near the connector surface. Consequently, the connection may fail due to bending of the free part of the beam rods, rather than withdrawal. This should however be investigated further.

6. Concluding remarks

This chapter presents concluding remarks regarding the use of numerical analyses to investigate the effect of various rod-to-grain angles and connector types. Additionally, proposals for further work is presented.

6.1 Conclusion

In order to establish numerical models of moment resisting beam-to-column connections, the simulation of withdrawal is essential. Cohesive zones were implemented as an alternative to the modelling of threads. A combination of a mean stiffness parameter in the radial and tangential directions, and a interpolated value for the specified angle in the normal direction, resulted in withdrawal stiffness that correlated well with experimental results, especially for smaller angles and longer embedment lengths.

Two configurations that had been tested experimentally were replicated numerically in order to validate the results from the simulations. The discrepancies in rotational stiffness were 16.1 % and 81.7 %. The poor correlation were contributed to the inability of the cohesive zone to replicate the experimental withdrawal stiffness for the angles and embedment lengths featured in this configuration.

A new steel connector was designed. The numerical simulations indicated a higher rotational stiffness than the previously used circular profile. Implementation of the connector imply the removal of a part of the beam resulting in no timber-to-timber interaction. Based on numerical analyses and experimental testing performed previously this should not negate the increase in stiffness due to the change of connector type.

The stress states in the column of the various configurations were evaluated in order to investigate the crack propagation experienced in the experimental testing. Both the shear stresses and the tensile stresses in the shear zone become excessively large if the two inner rods, CU1 and CL1, do not penetrate the entire column width. Generally, a larger distance between these two rods seems favourable regarding the magnitude of the shear stresses, as 70-55-10 exhibited the lowest. In the tension zone, all configurations, except for 70-70-10 and 70-70-05, display maximum tensile stresses of a value similar to the mean strength. The two exceptions experienced fairly extreme magnitudes which were contributed to the ending of the two inner

rods, CU1 and CL1, inside the column, resulting in fluctuations of stresses along the rods ultimately leading to a stress concentration near the column surface.

Of the numerically simulated configurations, 75-70-05 exhibited the highest rotational stiffness with 20 796 kN m/rad. By using the relative difference between the numerical and experimental rotational stiffness for 70-55-10 as an indication of the enhanced stiffness in the models, the experimental rotational stiffness of 75-70-05 may be in the range of 11 404-13 783 kN m/rad. Increasing the distance between the steel connectors is favourable, displaying an increase of 28.9 - 49.8 % using $z = 500$ mm compared to an identical configuration with $z = 450$ mm.

A configuration designed based on fire requirements, possessing a larger width of the timber components and column rods in different planes, displayed promising results. The stresses in the shear zone were considerably lower, while the rotational stiffness was nearly of a similar magnitude as 75-70-05. Although one rod was located within the charring depth, the connection had sufficient capacity to sustain the loading in SLS in a fire situation.

6.2 Proposals for future work

The numerical analysis of a beam-to-column connection has proven to be beneficially when considering parameters as stress state, force distribution, rotational stiffness and deflection. However, improvements to reduce the numerical stiffness within the numerical model is desirable.

To reduce the numerical stiffness within the model, several properties may be optimised. The withdrawal stiffness parameters, K_{tt} and K_{ss}, has the potential to be reduced with the use of other material properties as E_{RR}. Alternative withdrawal tests, as a combination of axial and lateral loading, would be beneficial to investigate how the withdrawal properties are effected in more complicated loading situations. A better representation of the material behaviour, as optimisation of linear-elastic and plastics properties, are of interest. This could give a better representation of stress distribution within the column, especially at higher loads levels.

Simulation of crack propagation in the column may give a better indication of the ultimate failure load and better understanding of where the initial cracking starts. To simulate crack propagation, XFEM or cohesive elements within the column may be applied.

The use of experimental testing is also of interest, as they may verify the results from the numerical simulations. Additional testing that can reveal the connections abilities, are fire testing and dynamic loading. Fire tests to reveal the connections capacity regarding fire resistance and dynamic loading to evaluate fatigue and the critical eigenfrequency.

References

[1] Kjell Arne Malo, Haris Stamatopoulos, Nesheim, and Solem. Requirements, lay-out and design considerations of a building system. DRAFT Version, 01 2017.

[2] Kristine S. Lied and Kjersti I. Nordal. A conceptual study of glulam connections using threaded rods and connecting circular steel profiles. Master's thesis, NTNU, 2016.

[3] Manfred Augustin. *Handbook 1 Timber Structures*. Leonardo da Vinci Pilot Projects, "Educational Materials for Designing and Testing of Timber Structures - TEMTIS", 2008.

[4] GGI. About wood, science of wood, 2017. `https://www.ggi-mm.com/wood/`.

[5] Hans Larsen and Enjily Vahik. *Practical design of timber structures to Eurocode 5*. Thomas Telford Limited, 2009.

[6] European Committee for Standardization (CEN). *NS-EN 14080:2013 Timber structures - Glued laminated timber and glued solid timber - Requirements*. Standard Norge, 2013.

[7] Haris Stamatopoulos and Kjell Arne Malo. Connections with threaded rods in moment resisting frames. *World Conference on Timber Engineering*, 2016.

[8] Nina Westerheim. Conceptual study of connections using glulam and long threaded bars exposed to fire loading. Master's thesis, NTNU, 2015.

[9] Haris Stamatopoulos. *Withdrawal Properties of Threaded Rods Embedded in Glued-Laminated Timber Elements*. PhD thesis, NTNU, 2016.

[10] Haris Stamatopoulos and Kjell Arne Malo. Withdrawal stiffness of threaded rods embedded in timber elements. *Construction and Building Material*, 116:263–272, 2016.

[11] Haris Stamatopoulos and Kjell Arne Malo. Withdrawal capacity of threaded rods embedded in timber elements. *Construction and Building Material*, 94:387–397, 2015.

[12] Haris Stamatopoulos and Kjell Arne Malo. Withdrawal of pairs of threaded rods with small edge distances and spacings. *European Journal of Wood and Wood Products*, pages 1–12, 2017.

[13] Halvor Grytting and Eirik D. Sæle. Axial and lateral loaded threaded rods in timber structures. Master's thesis, NTNU, 2015.

[14] Hallvard O. Veium. Axially loaded threaded rods in glulam connections. Master's thesis, NTNU, 2016.

[15] O. Volkersen. Die nietkrafverteilung in zugbeanspruchten nietverbindungen mit konstanten laschenquerschnitten. *Luftfahrtsforschung*, 15:41–47, 1938.

[16] European Committee for Standardization (CEN). *Eurocode 5: Design of timber structures, Part 1-1: General Common rules and rules for buildings*. Standard Norge, 2004.

[17] Kolbein Bell. *An engineering approach to FINITE ELEMENT ANALYSIS of linear structural mechanics problems*. Fagbokforlaget Vigmostad & Bjørke AS, 2014.

[18] Kolbein Bell. *MATRISESTATIKK Statiske beregninger av rammekonstruksjoner*. Fagbokforlaget Vigmostad & Bjørke AS, 2010.

[19] Malkus D. S. Plesha M. E Witt R . J Cook, R. D. *Concepts and applications of finite element analysis*. John Wiley & Sons. Inc., 2001.

[20] Dassault Systèmes. *Abaqus Analysis User´s Guide*. Dassault Systèmes Simulia Corp, 2014.

[21] Kjell M. Mathisen. Lecture notes, tkt 4191 nonlinear finite element analysis, 2013.

[22] A. A. Griffith. The phenomena of rupture and flow in solids. *Philosophical Transactions of the Royal Society of London A: Mathematical, Physical and Engineering Sciences*, 221(582-593):163–198, 1921.

[23] G.R. Irwin. Fracture dynamics. *Fracturing of metals*, page 147–166, 1948.

[24] Anthony C Fischer-Cripps. *Introduction to Contact Mechanics*. Springer, 2007.

[25] Hillerborg A. *Application of the fictitious crack model of different types of materials*. International Journal of Fracture, 1991.

[26] Online Dokumentation help. *Abaqus 6.14-1 Analysis User´s Manual*. Dassault Systèmes Simulia Corp, 2014.

[27] Kristian B. Dahl. *Mechanical properties of clear wood from Norwegian spruce*. PhD thesis, NTNU, 2009.

[28] Persaud R Symos, D and H Stainslaus. Slip modulus of inclined screws in timber-concrete floors. *Institution of Civil Engineers, Cambridge, UK*, 2009.

[29] European Committee for Standardization (CEN). *Eurocode 5: Design of timber structures, Part 1-2: General - Structural fire design*. Standard Norge, 2004.

[30] Henning Bjørge and Terje Kristoffersen. personal communication.

[31] Martin Flattum Hartnes and Kim André Åby. Timber composite floor. Master's thesis, NTNU, 2016.

[32] European Committee for Standardization (CEN). *Eurocode 1: Actions on structures, Part 1-1: General actions. Densities, self-weight, imposed loads for buildings*. Standard Norge, 2002.

[33] European Committee for Standardization (CEN). *Eurocode 0: Basis of structural design*. Standard Norge, 2002.

Appendices

A. Calculations

A.1 Force distribution - MatLab-script

The MatLab-script calculating the force distribution for column rod inclinations of 75 and 70 degrees as an example.

```
P=10;
z=450;
L=2000;
alpha_u=70;
alpha_l=75;
F=[P*L/z;
    p/2];
T=[sin(alpha_u*pi/180) sin(alpha_l*pi/180);
   cos(alpha_u*pi/180) -cos(alpha_l*pi/180)];
Fx=inv(T)*F
```

A.2 Acting moment in the joint

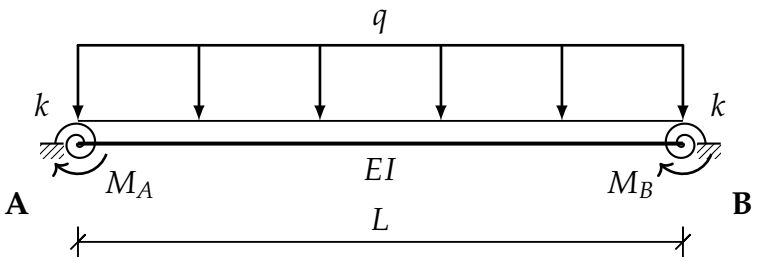

Figure A.1: Beam with rotational springs at the supports subjected to a uniformly distributed load

The moment-rotation relation for rotational springs are defined as:

$$M = -k \cdot \phi \tag{A.1}$$

Due to symmetry in Figure A.1:

$$M_A = M_B \tag{A.2}$$

$$\phi_{AB} = \phi_{BA} \tag{A.3}$$

The total rotation at support A is the sum of rotations due to the moment in both supports and the uniformly distributed load:

$$\phi_{AB} = \phi_{AB}(M_A) + \phi_{AB}(M_B) + \phi_{AB}(q) \tag{A.4}$$

Each contribution can be calculated by use of formulas from Euler-Bernoulli beam theory:

$$\phi_{AB}(M_A) = \frac{ML}{3EI} \tag{A.5}$$

$$\phi_{AB}(M_B) = \frac{ML}{6EI} \tag{A.6}$$

$$\phi_{AB}(q) = \frac{qL^3}{24EI} \tag{A.7}$$

Additionally, the stiffness of the joint will affect the rotation. Equation A.1 may be written as:

$$\phi_k = -\frac{M}{k} \tag{A.8}$$

Enforcing rotational equilibrium at the support:

$$\phi_q - \phi_{AB}(M_A) - \phi_{AB}(M_B) - \phi_k = 0 \tag{A.9}$$

And inserting the beam formulas:

$$\frac{qL^3}{24EI} - \frac{ML}{3EI} - \frac{ML}{6EI} - \frac{M}{k} = 0 \tag{A.10}$$

Rearranging to find an expression for the moment:

$$M_{joint} = \frac{qL^3}{24EI}\left[\frac{L}{2EI} + \frac{1}{k}\right]^{-1} \tag{A.11}$$

A.3 Comparison of material usage

Circular profile:	Inner diameter	115.2	mm
	Outer diameter	172.3	mm
	Volume:	457 387	mm^3

Plate 70-55-10	Dimensions				Area	Volume
	Length	Angle	Radius [mm]			
	[mm]	[°]	Inner	Outer	[mm^2]	[mm^3]
A1:	63				2 205	88 200
A2:	50				1 750	70 000
A3:	63				2 205	88 200
A4:		25	20	55	573	22 907
A5:		30	15	50	596	23 824
Hole:		360		11		39 914
Total:						253 217

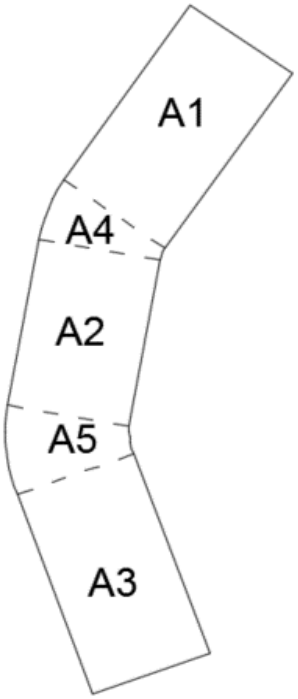

Plate 70-70-05	Dimensions				Area	Volume
	Length	Angle	Radius [mm]			
	[mm]	[°]	Inner	Outer	[mm^2]	[mm^3]
A1:	63				2 205	88 200
A2:	50				1 750	70 000
A3:	63				2 205	88 200
A4:		15	10	45	252	10 079
A5:		25	15	50	496	19 853
Hole:		360		11		39 914
Total:						236 418

Plate 45-45-10	Dimensions				Area	Volume
	Length	Angle	Radius [mm]			
	[mm]	[°]	Inner	Outer	[mm^2]	[mm^3]
A1:	63				2 205	88 200
A2:	50				1 750	70 000
A3:	63				2 205	88 200
A4:		35	6	41	502	20 097
A5:		45	11	56	1 184	47 360
Hole:		360		11		39 914
Total:						273 943

Steel volume reduction Plate vs circular profile		
Plate 70-55-10	Plate 70-70-05	Plate 45-45-10
44.6 %	48.3 %	40.1 %

A.4 Component method applied to the steel plate

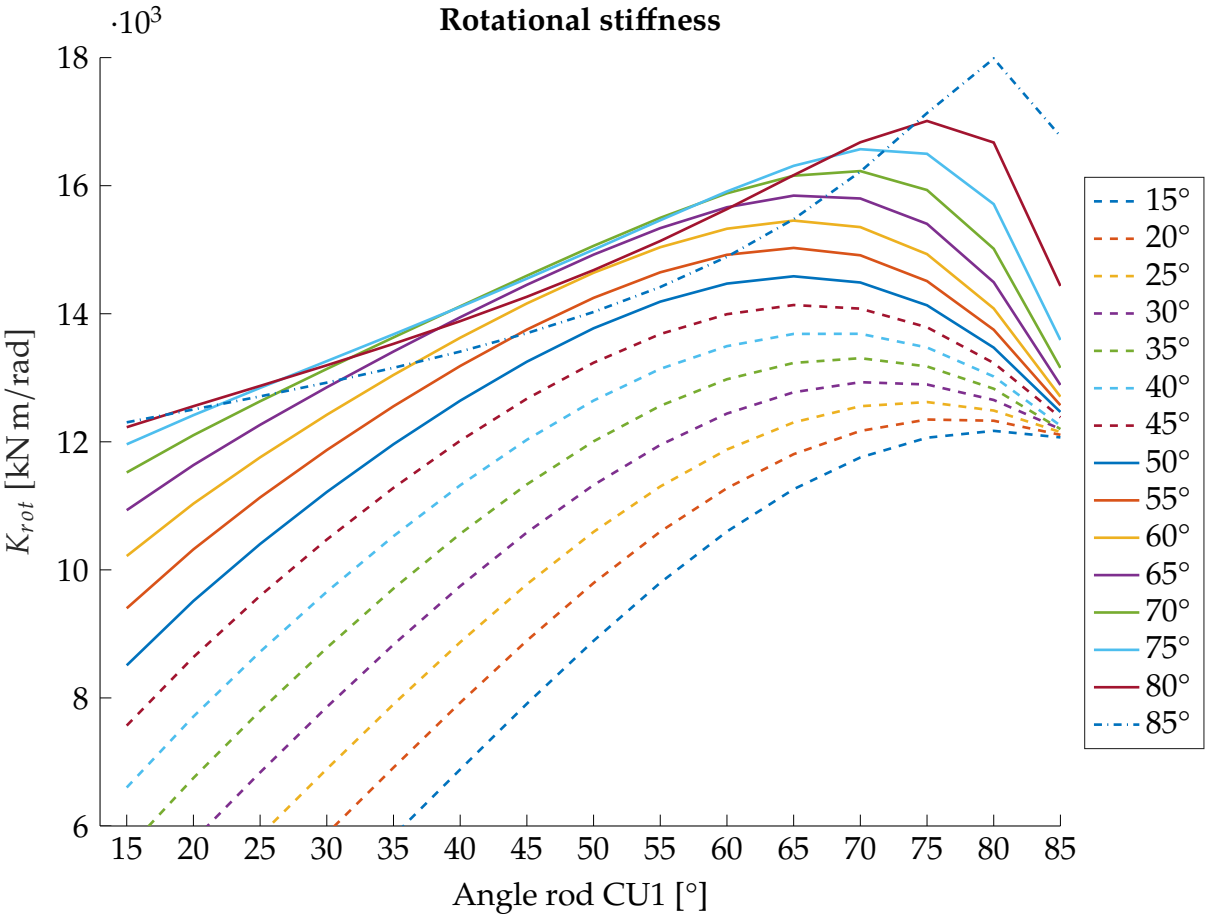

Figure A.2: Rotational stiffness for varying rod-to-grain angles for the column rods with the new steel profile. The angle of rod BU in the beam is 5 degrees

B. Cohesive zone parameters

B.1 Withdrawal calibrated at l = 100 mm

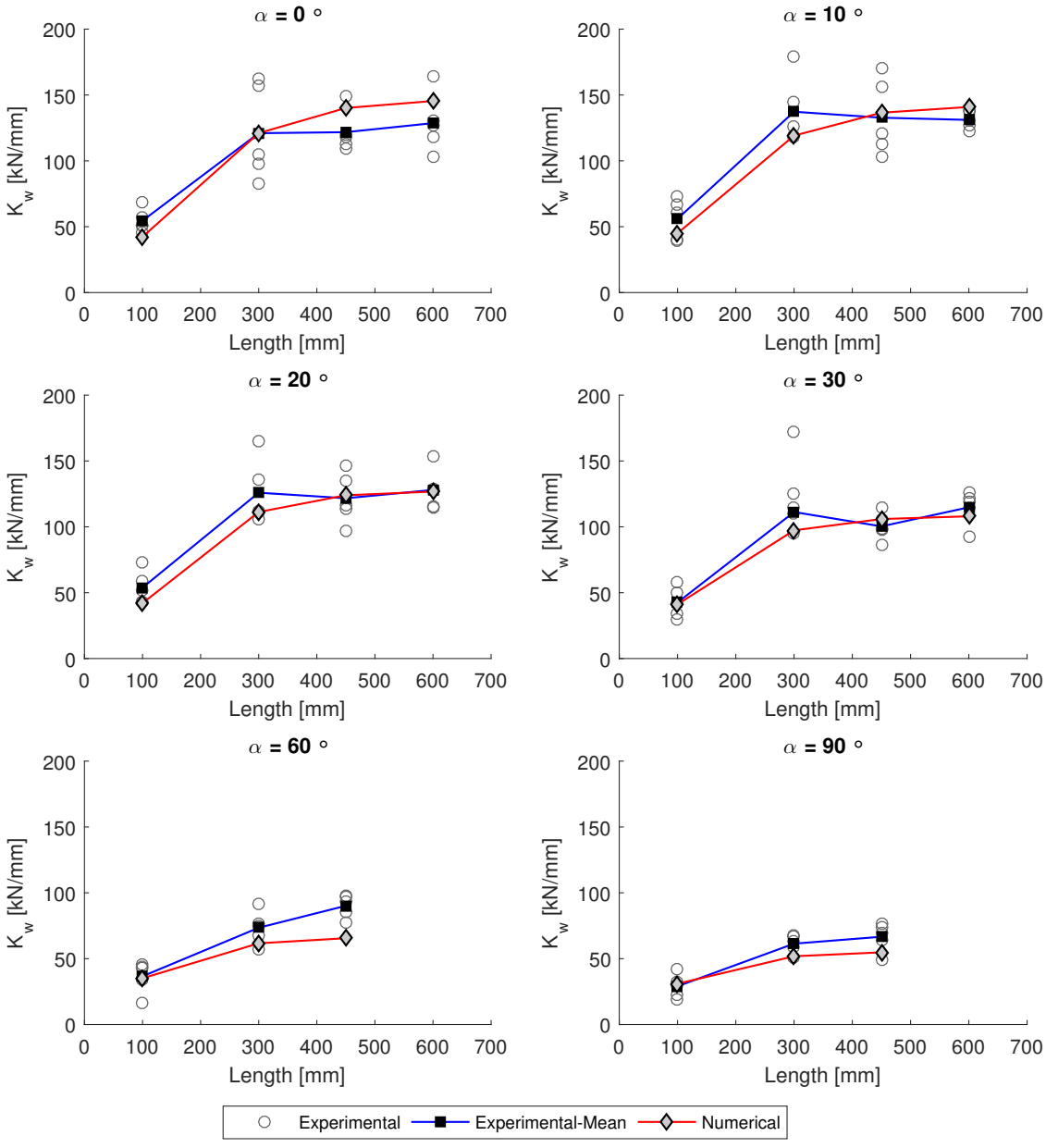

Figure B.1: Withdrawal stiffness calibrated at $l = 100\,\text{mm}$

B.2 Withdrawal calibrated at l = 300 mm

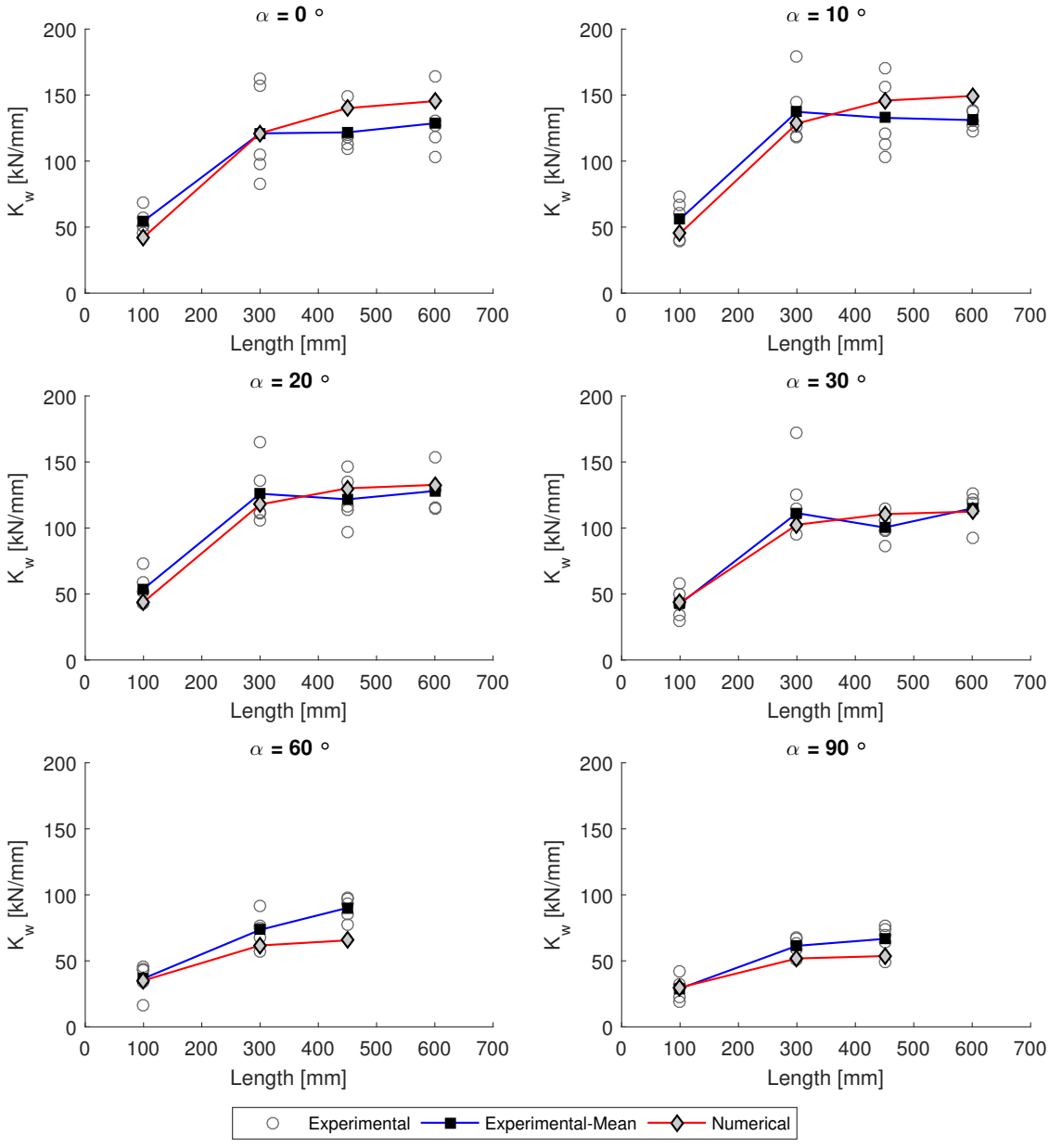

Figure B.2: Withdrawal stiffness calibrated at $l = 300\,\text{mm}$

C. Sketches of the configurations

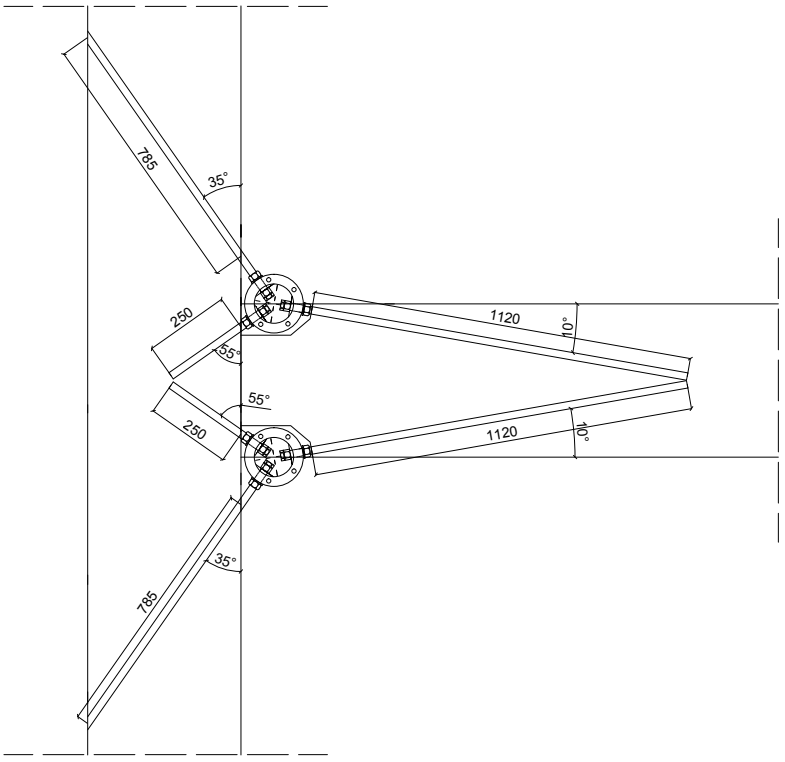

Figure C.1: 55-35-10

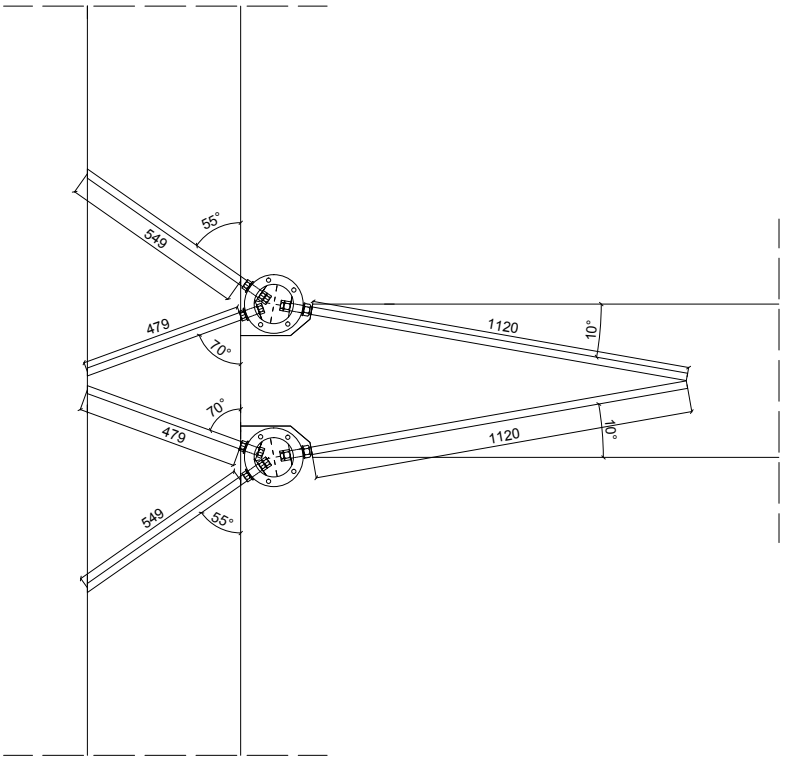

Figure C.2: 70-55-10

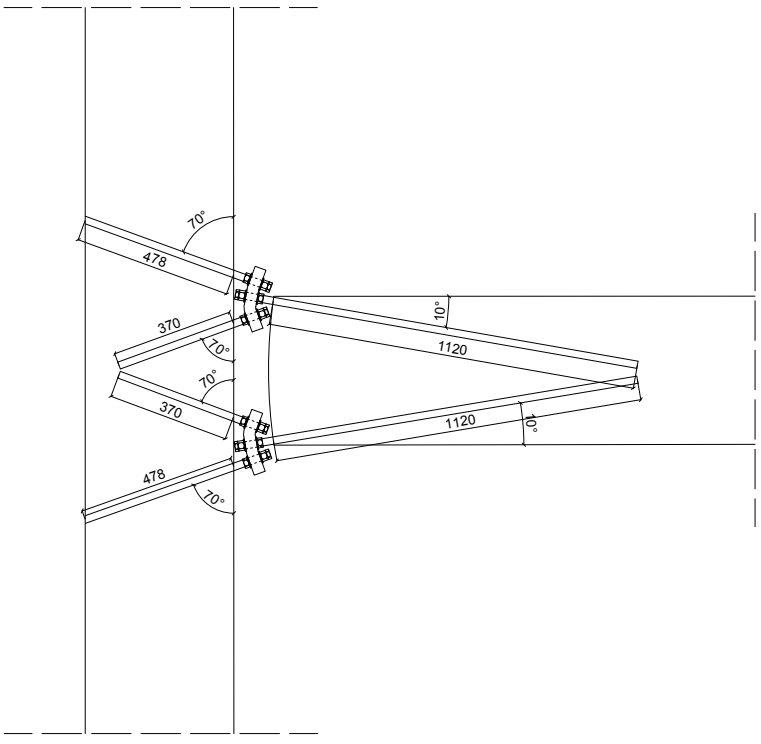

Figure C.3: 70-70-10

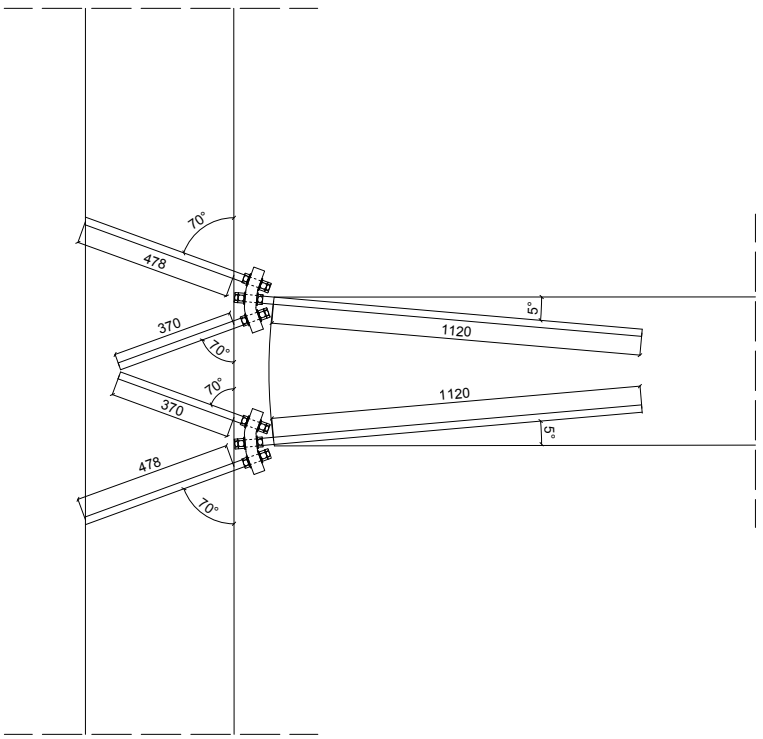

Figure C.4: 70-70-05

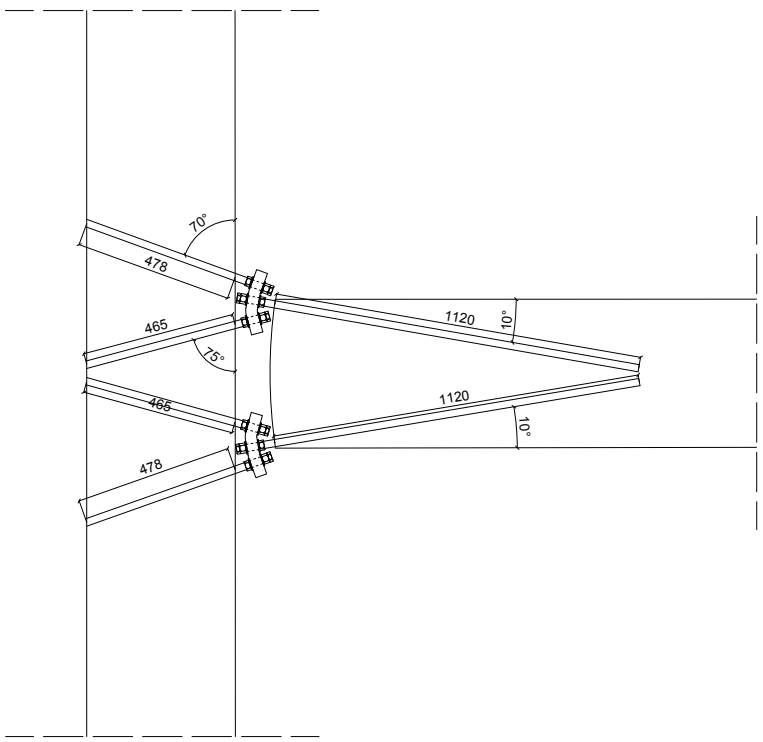

Figure C.5: 75-70-10

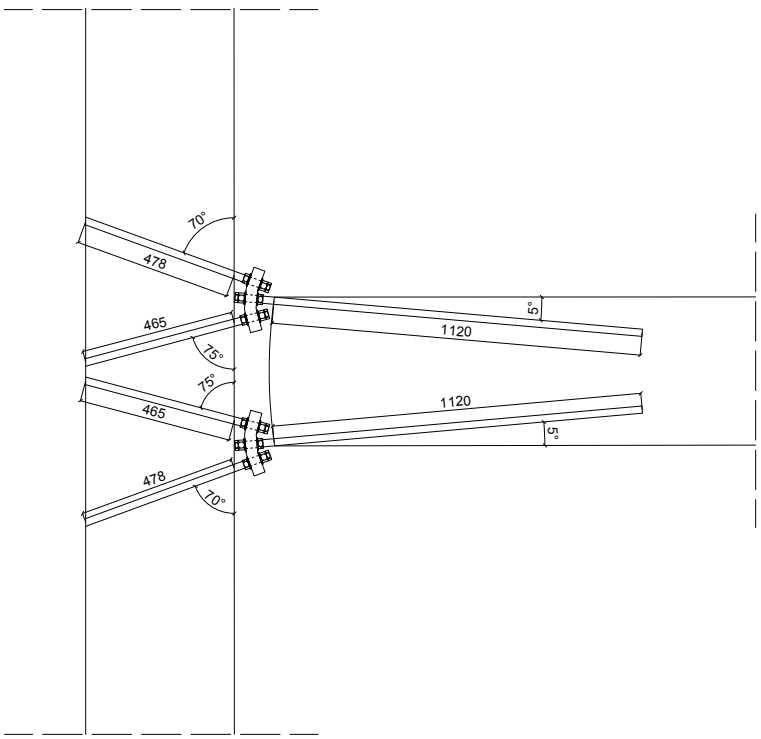

Figure C.6: 75-70-05

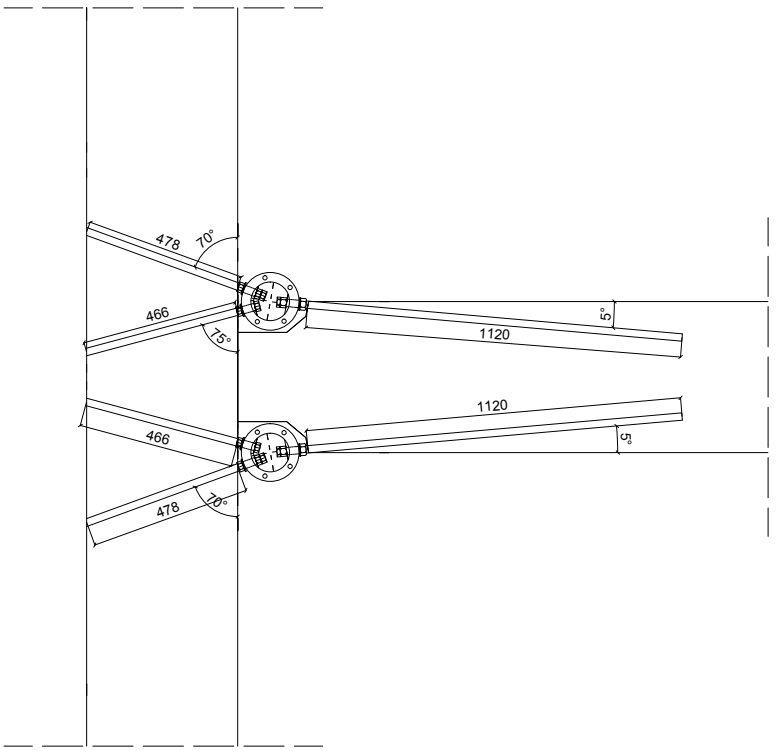

Figure C.7: 75-70-05 with circular profile

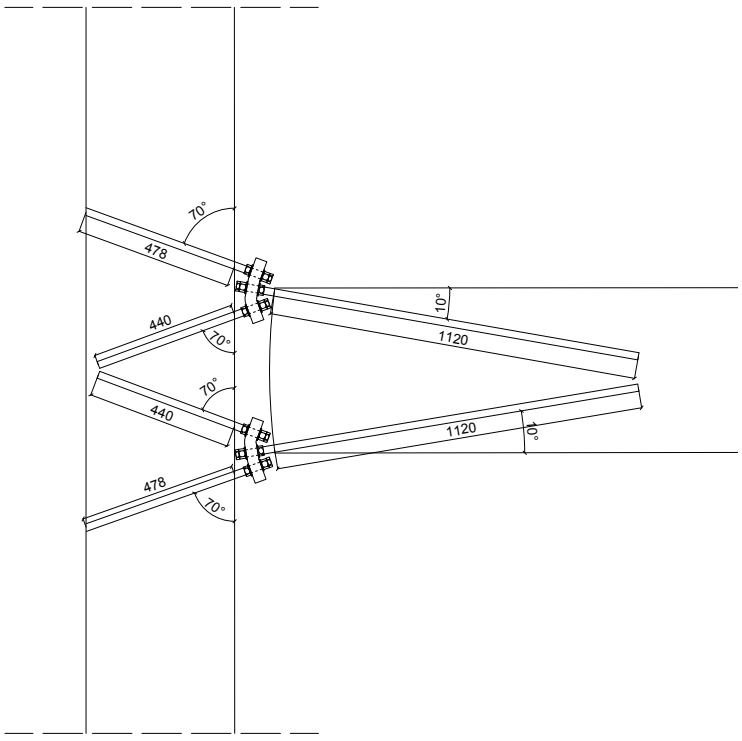

Figure C.8: 70-70-10 ($h = 500\,\text{mm}$)

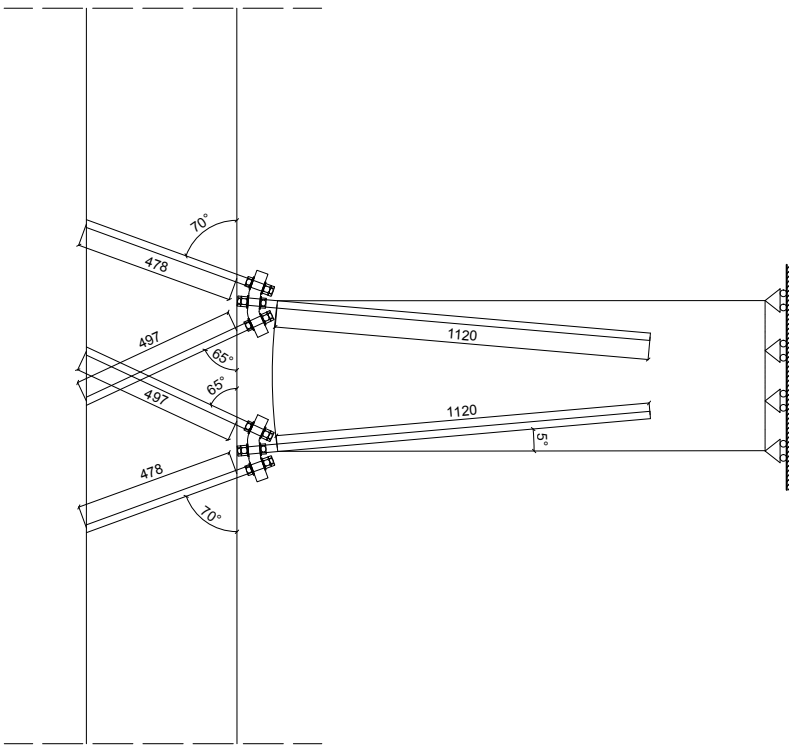

Figure C.9: 65-70-05

D. Stresses in the column

D.1 Stress states

70-70-10

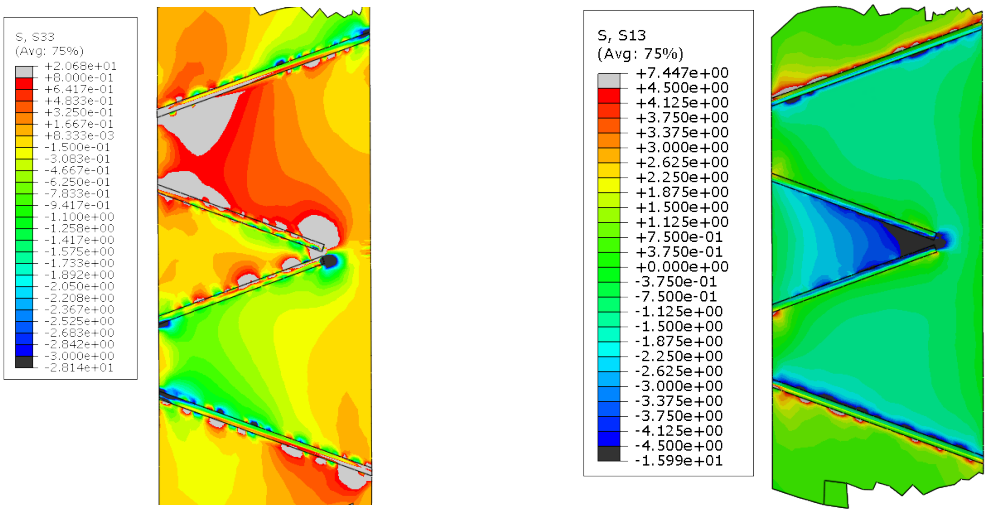

(a) Normal stress perpendicular to the grains (b) Shear stress

Figure D.1: Stress state in the column for 70-70-10

70-70-05

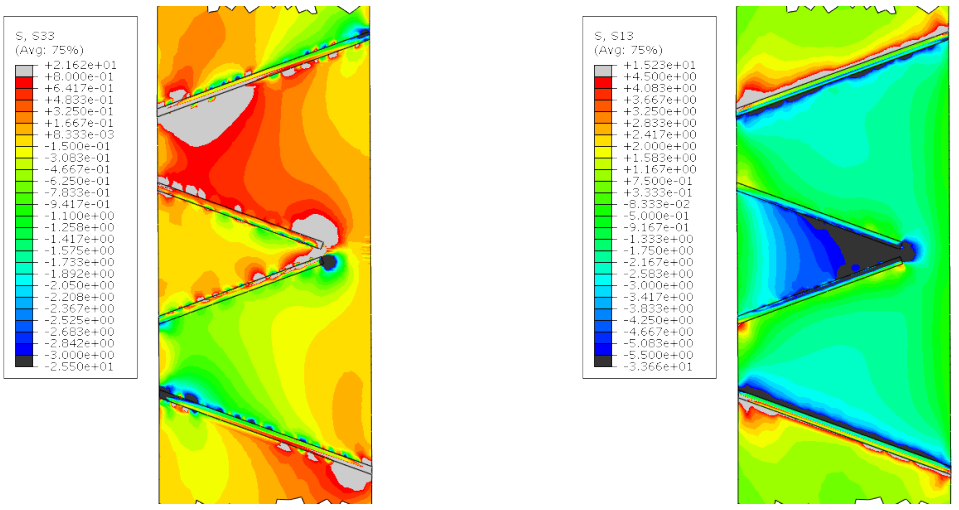

(a) Normal stress perpendicular to the grains (b) Shear stress

Figure D.2: Stress state in the column for 70-70-05

75-70-10

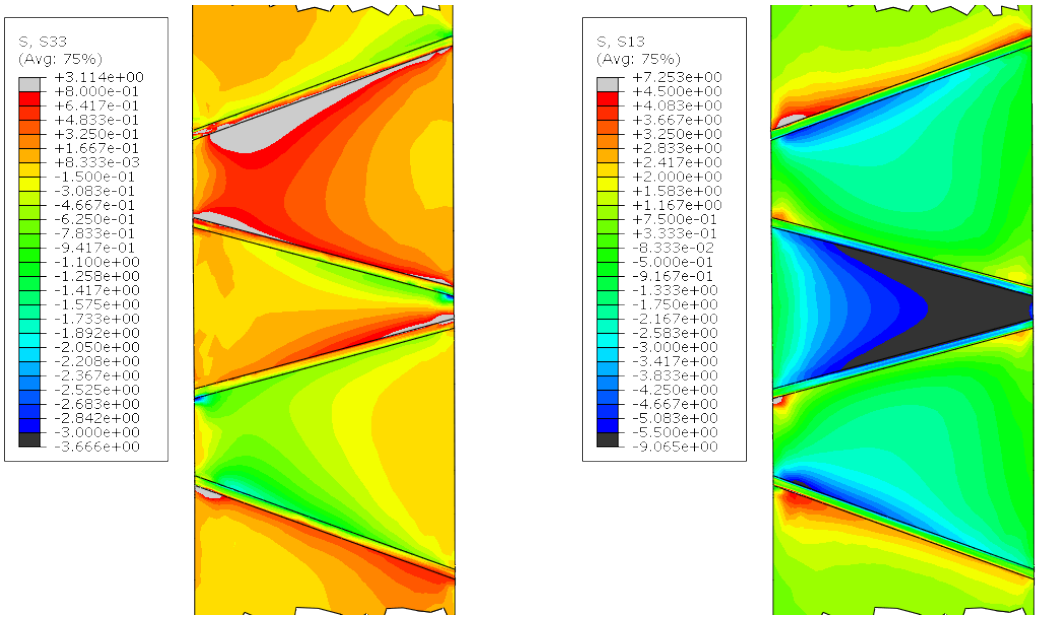

(a) Normal stress perpendicular to the grains (b) Shear stress

Figure D.3: Stress state in the column for 75-70-10

70-70-10 with h = 500 mm

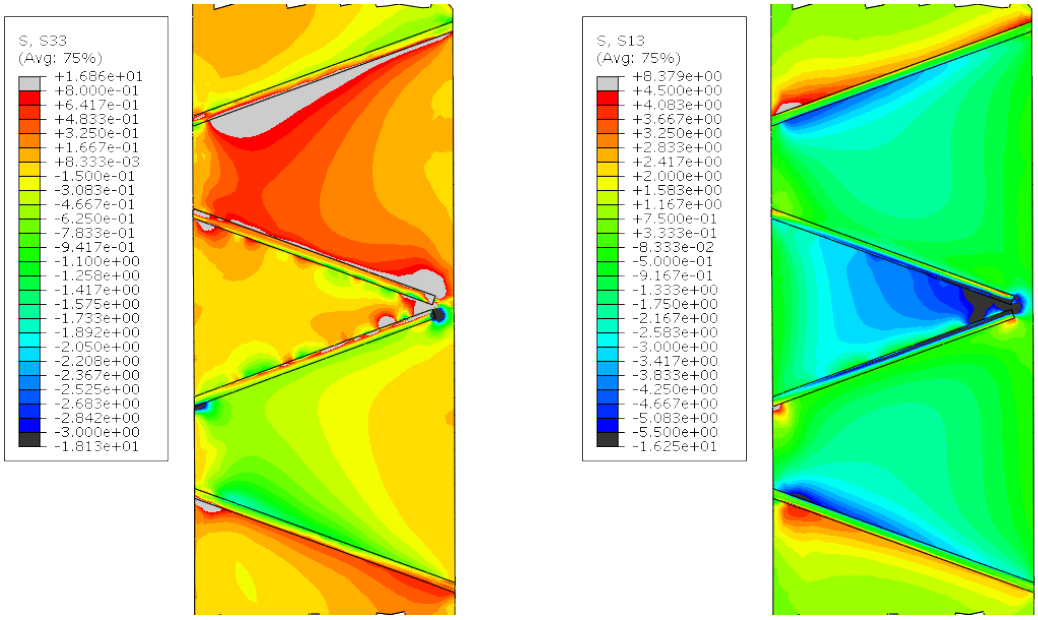

(a) Normal stress perpendicular to the grains (b) Shear stress

Figure D.4: Stress state in the column for 70-70-10

65-70-05

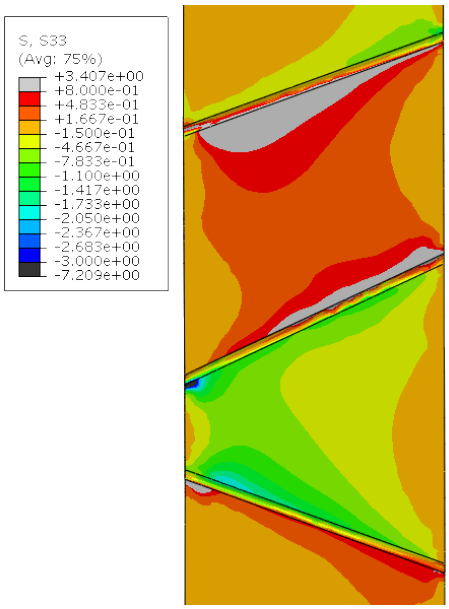

(a) Normal stress perpendicular to the grains

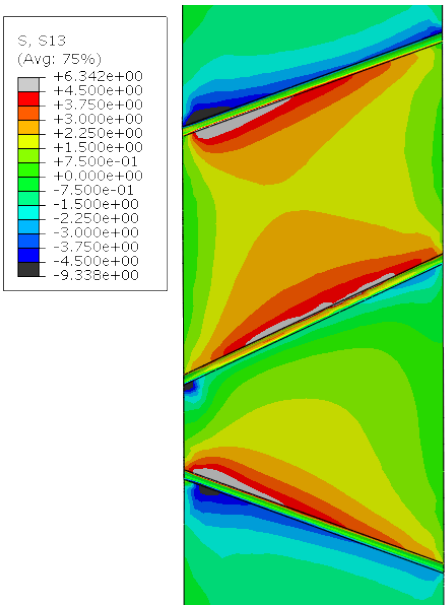

(b) Shear stress

Figure D.5: Stress state in the column for 65-70-05

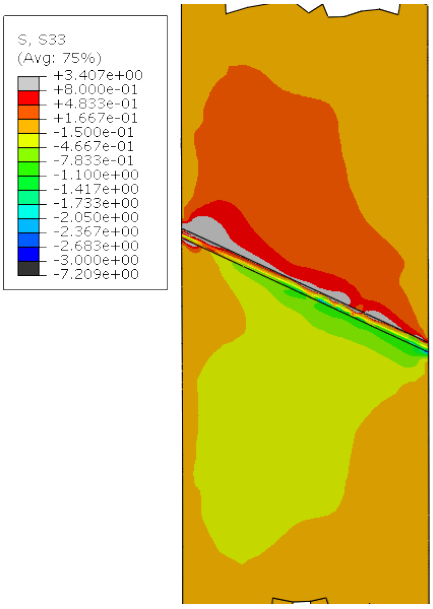

(a) Normal stress perpendicular to the grains

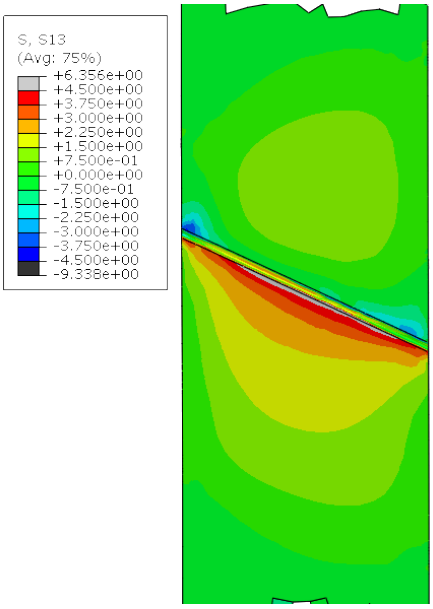

(b) Shear stress

Figure D.6: Stress state in the column for 65-70-05

D.2 Comparisons

The stresses extracted directly between the inner rods along the center line exhibits excessive peaks where these end. Dissimilar to the other graphs, also the configurations where the rods CU1 and CL1 penetrate the entire column experience similar peaks. These are located ≈ 20 mm from the column surface which is consistent with the tendency elucidated in the previous paragraph of the location of maximum shear stresses before the end of the rods. Of these are the 70-55-10 of the highest magnitude. The reason is presumably the shortest distance between the two inner rods.

D.2.1 Center

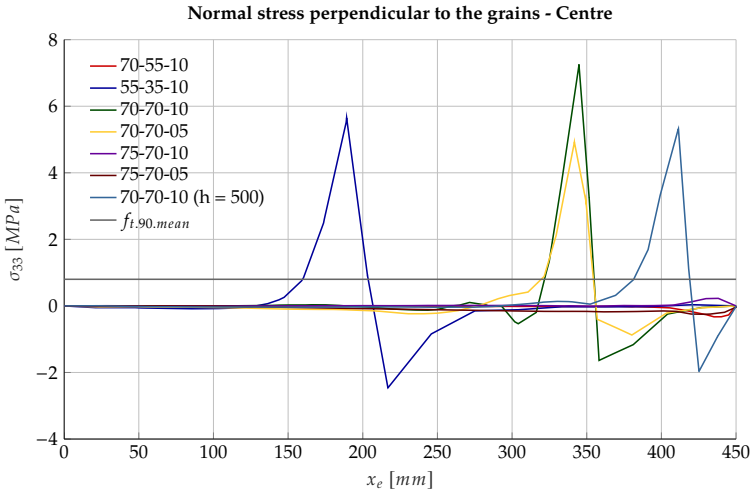

Figure D.7

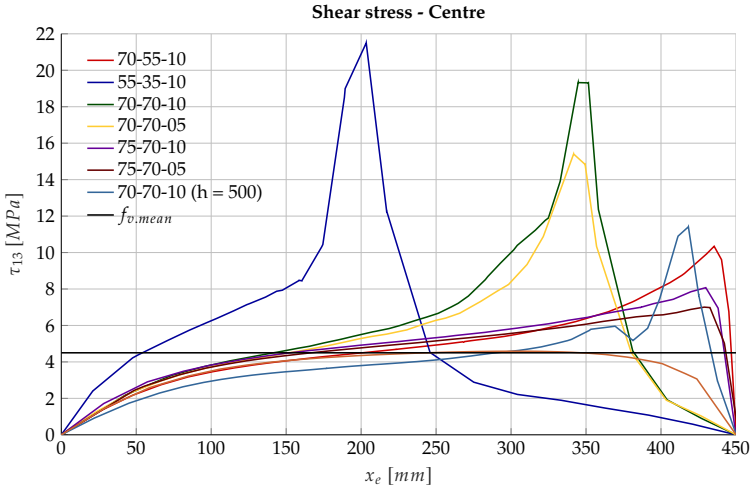

Figure D.8

D.2.2 Left

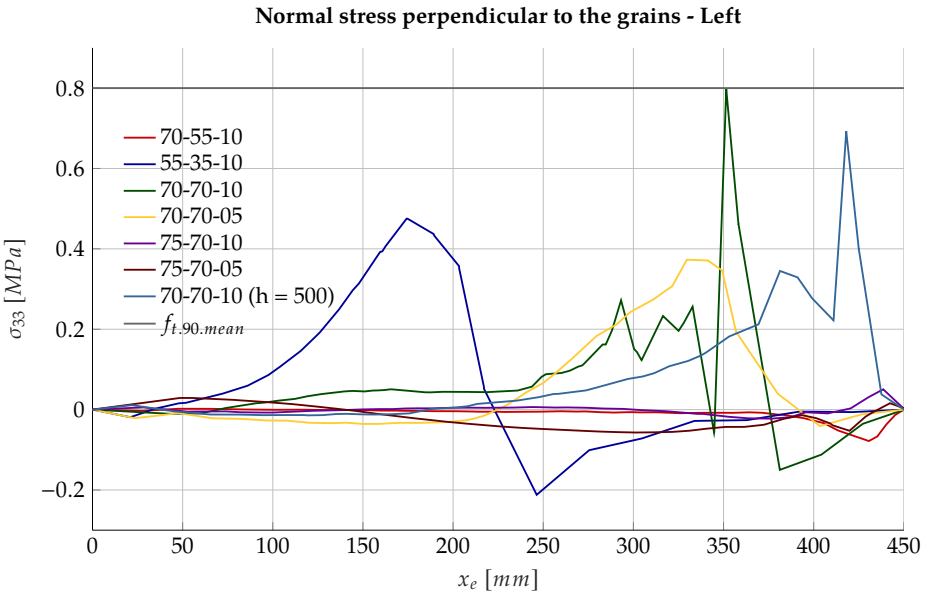

Figure D.9

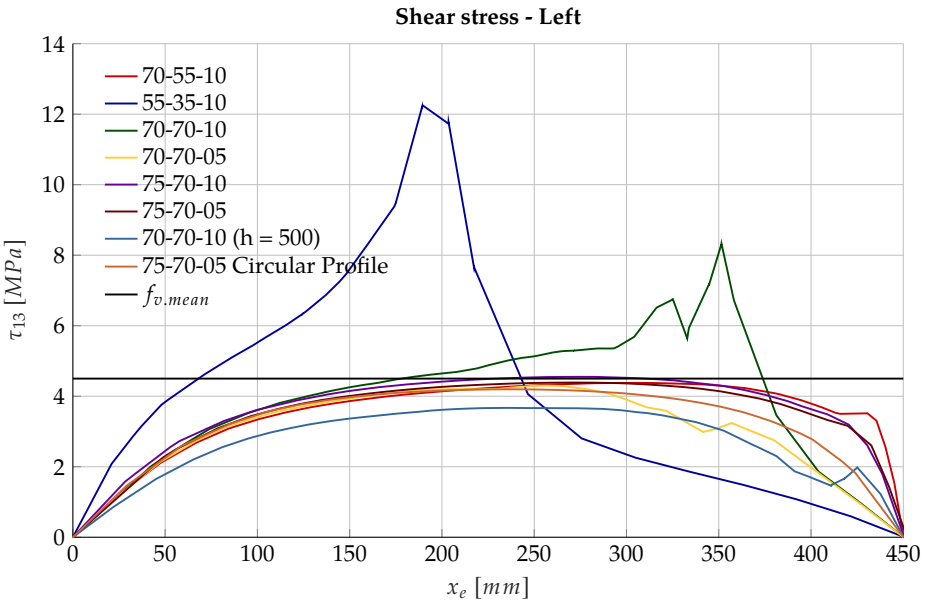

Figure D.10

E. Stresses in the rods - Withdrawal models

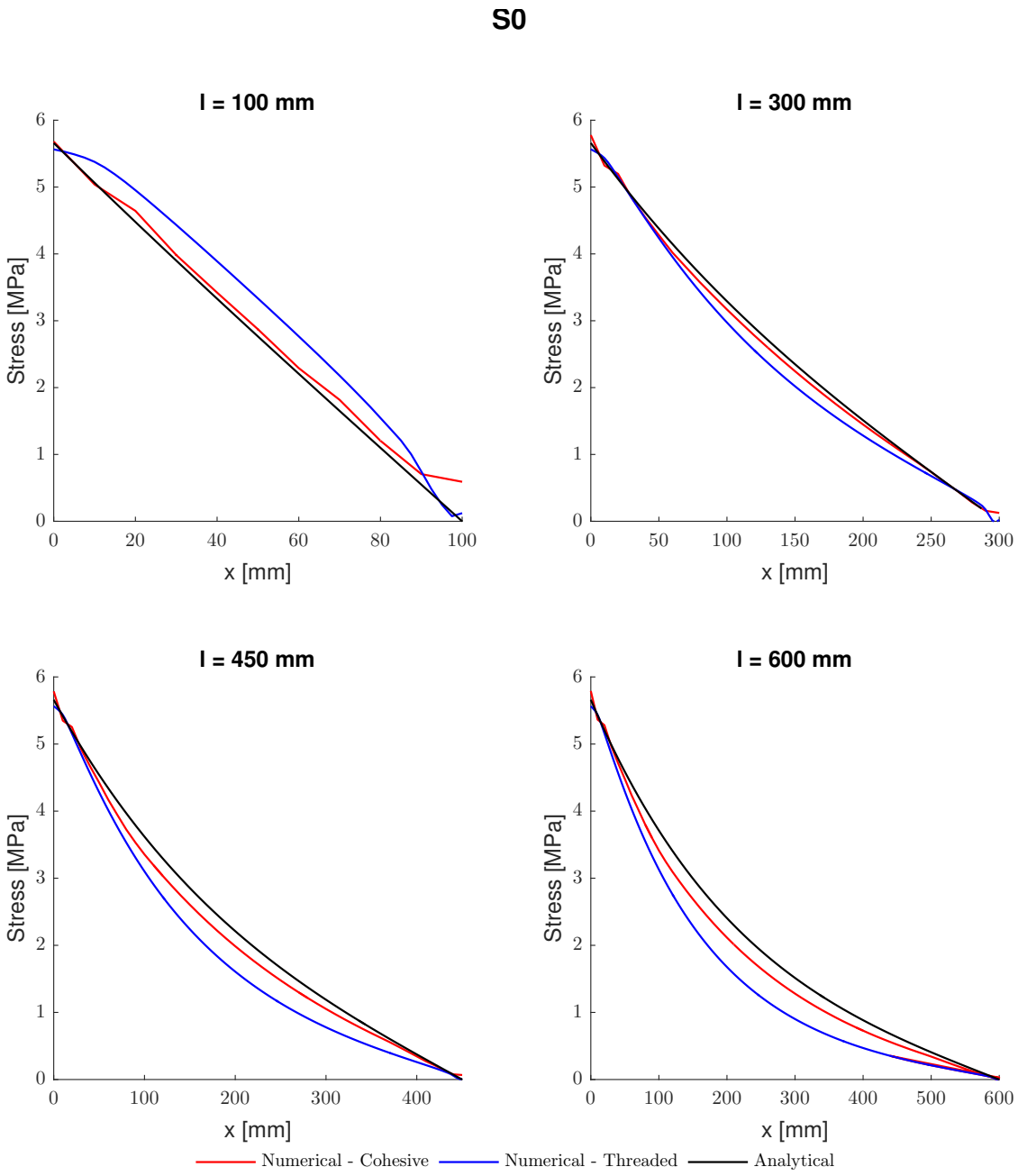

Figure E.1: $\alpha = 0°$

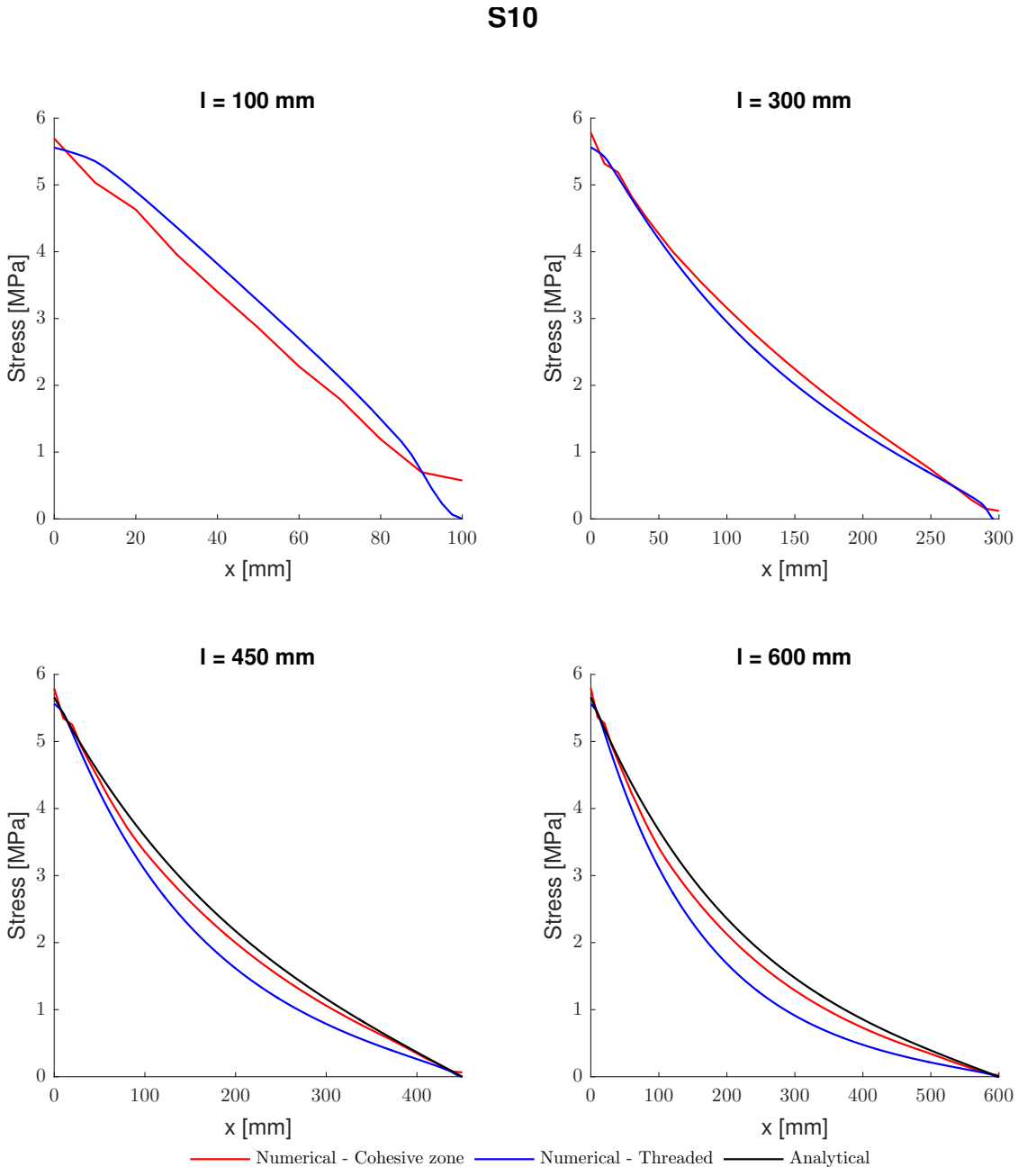

Figure E.2: $\alpha = 10°$

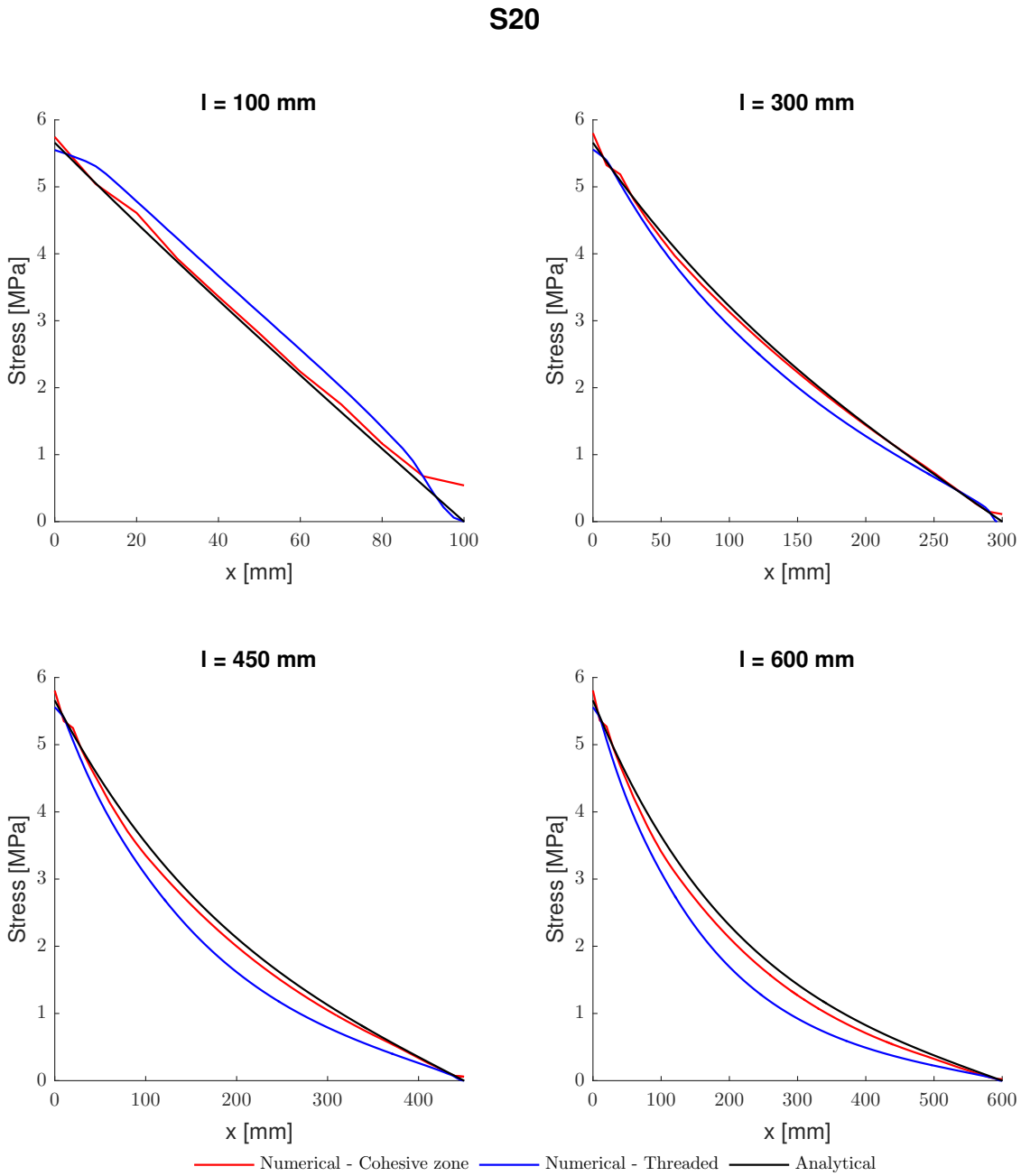

Figure E.3: $\alpha = 20°$

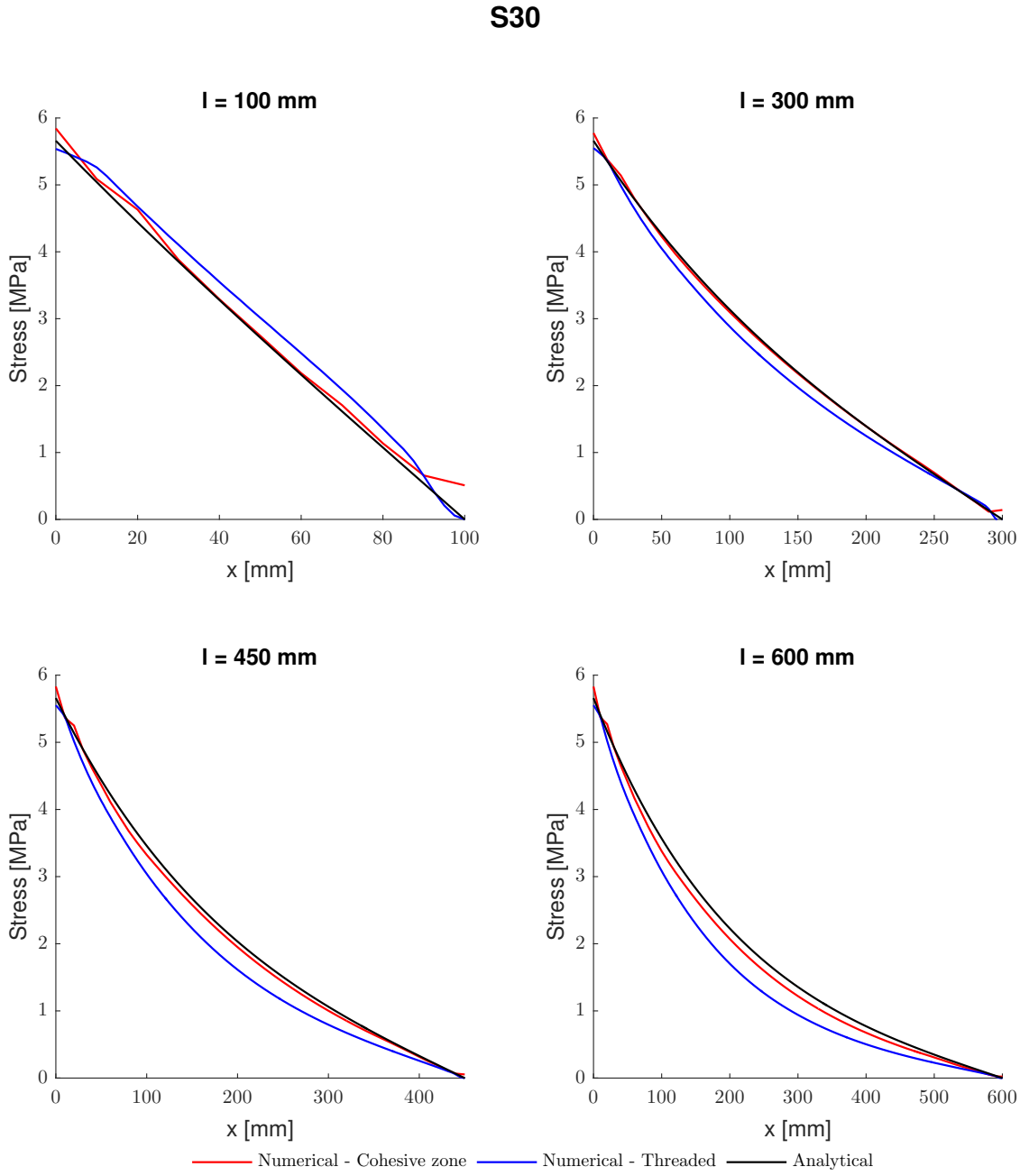

Figure E.4: $\alpha = 30°$

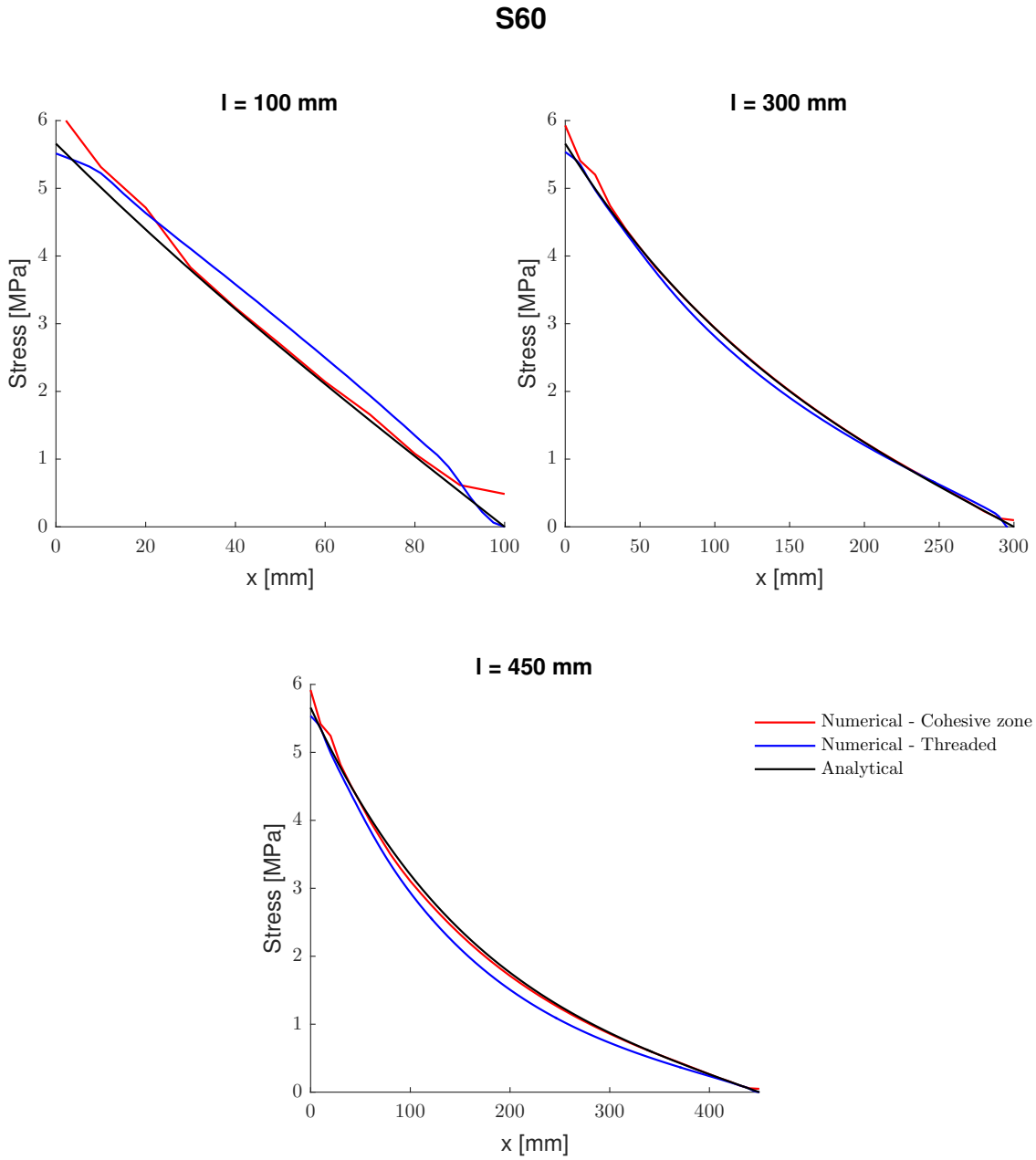

Figure E.5: $\alpha = 60°$

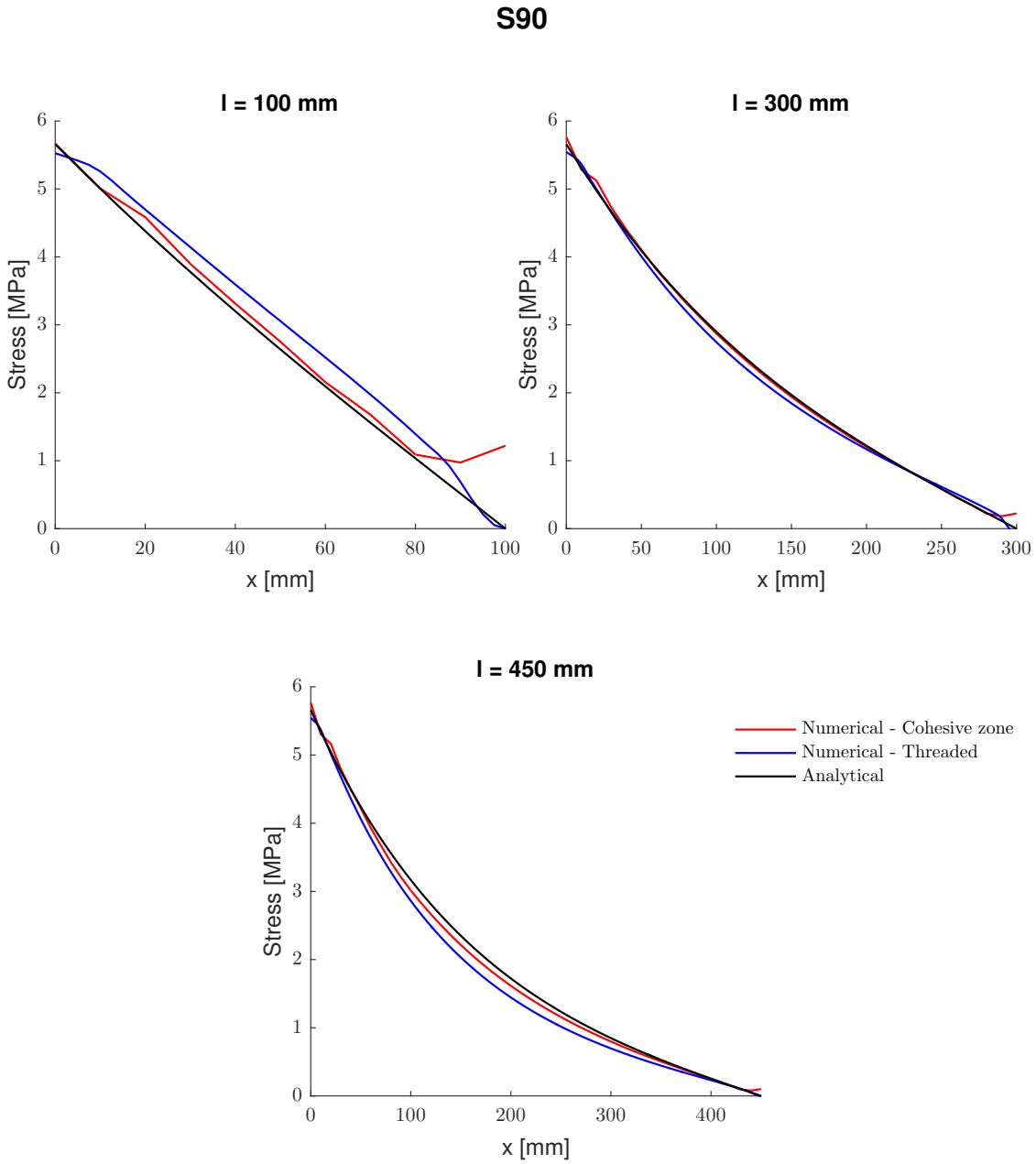

Figure E.6: $\alpha = 90°$

F. Documentation of numerical models

F.1 Withdrawal models

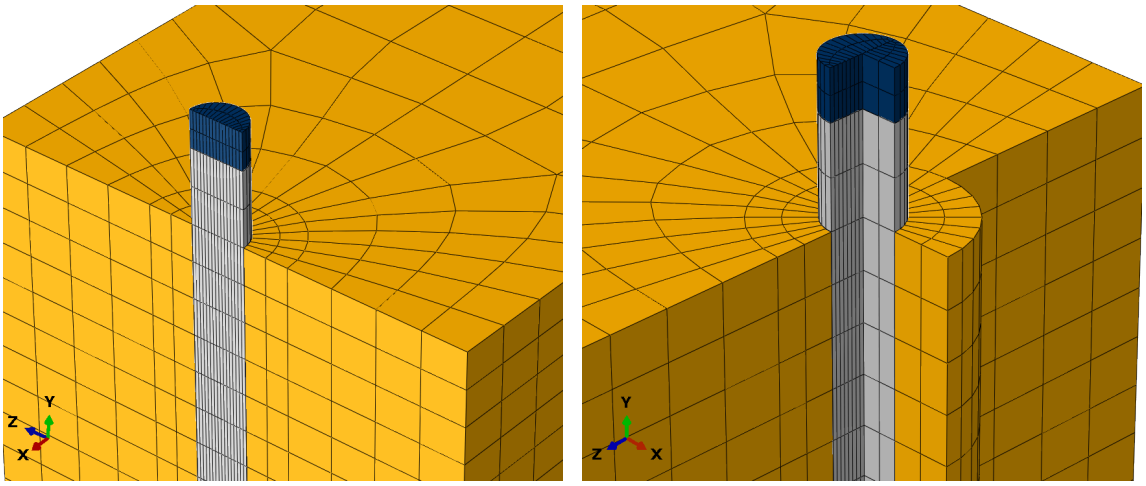

(a) (b)

Figure F.1: Inner section of withdrawal model

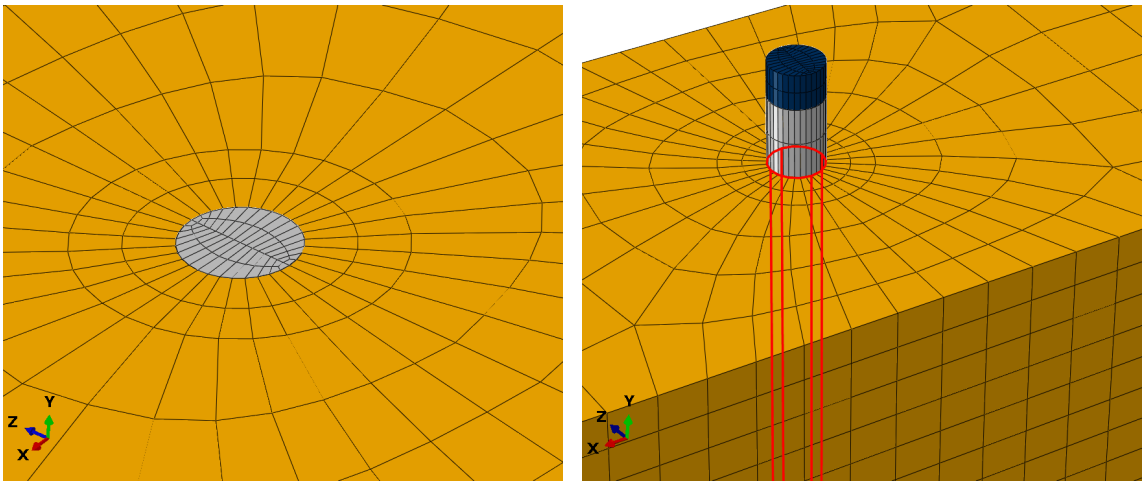

(a) Mesh rod and wood (b) Cohesive surface

Figure F.2

F.2 Connector

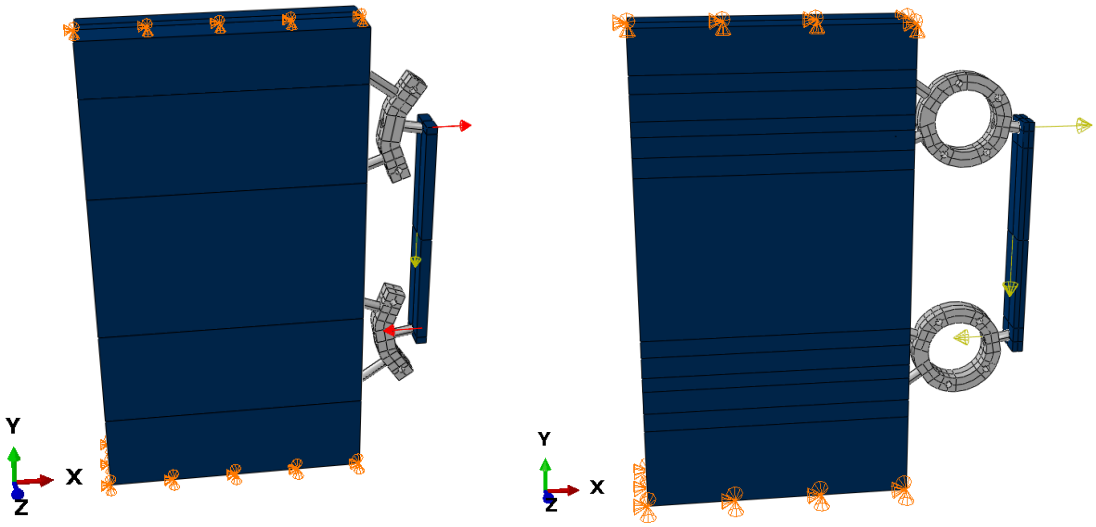

(a) Plate profile (b) Circular profile

Figure F.3

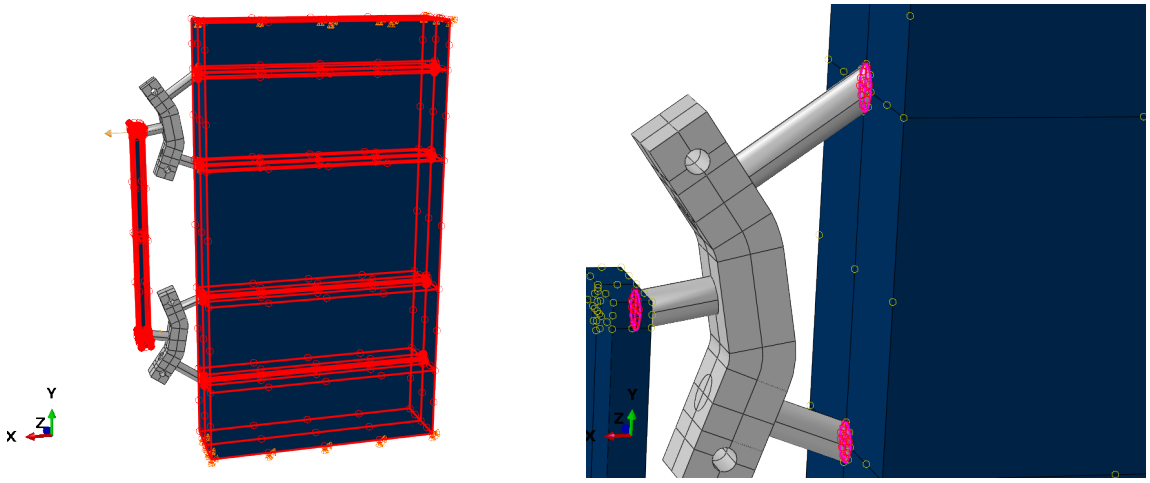

(a) Rigid body, illustrated in red (b) Tie constrain, illustrated in pink

Figure F.4

F.3 Connection

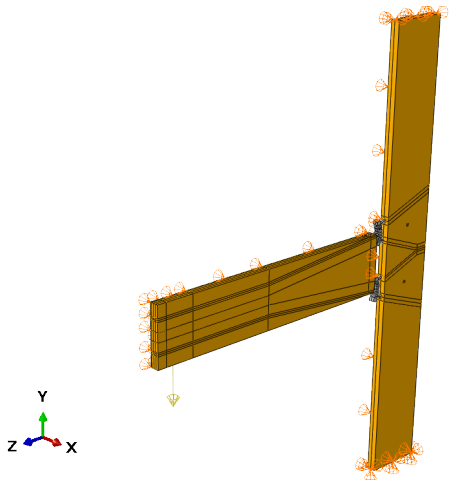

(a) 70-70-05

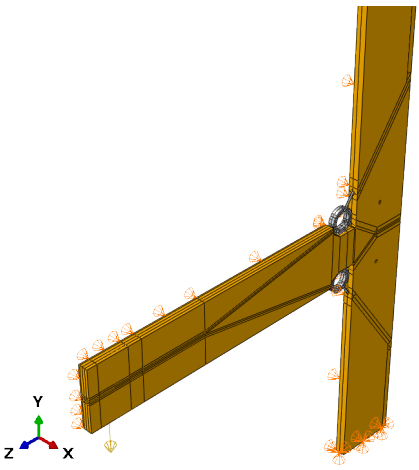

(b) 55-35-10

Figure F.5

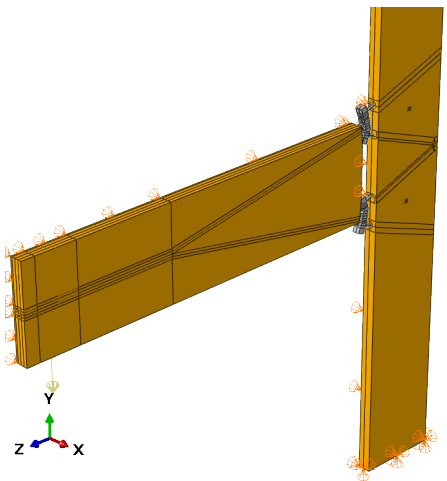

(a) Increased height 70-70-10

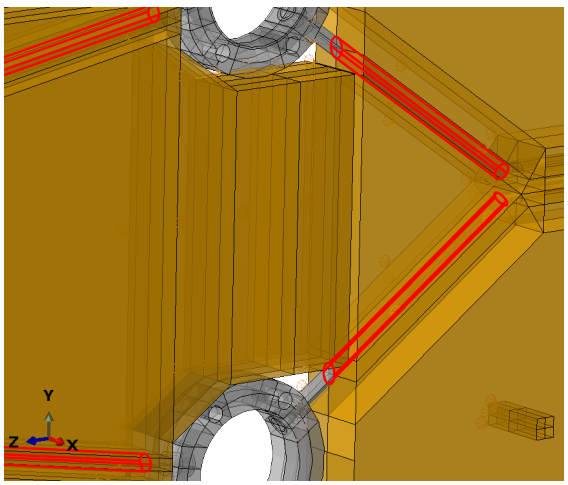

(b) Cohesive surface, 55-35-10

Figure F.6

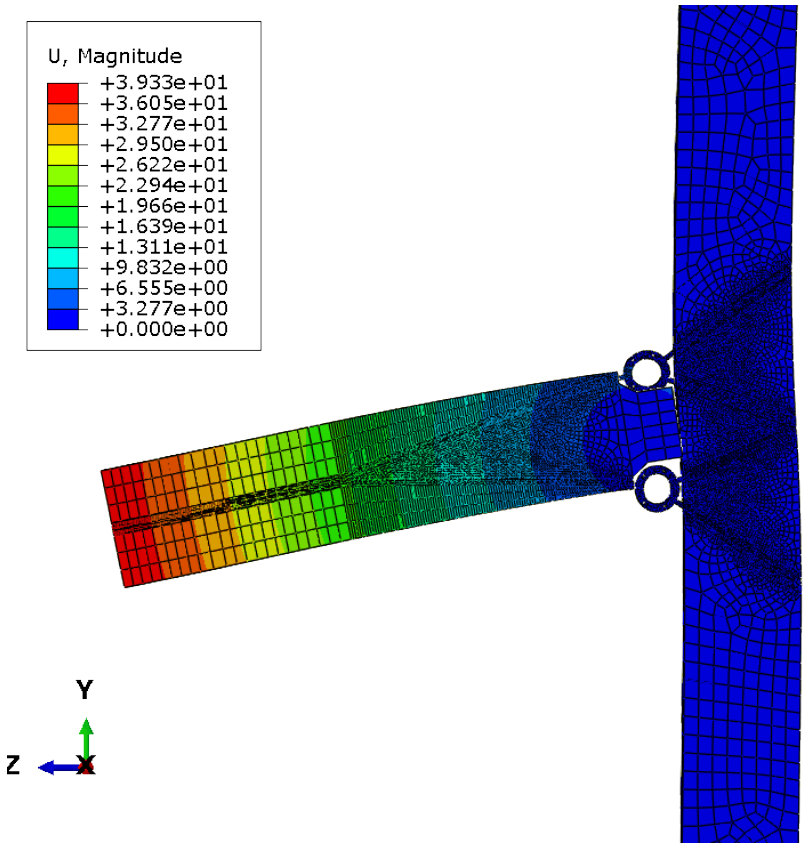

(a) Displacement 70-55-10, magnified by a factor of 10

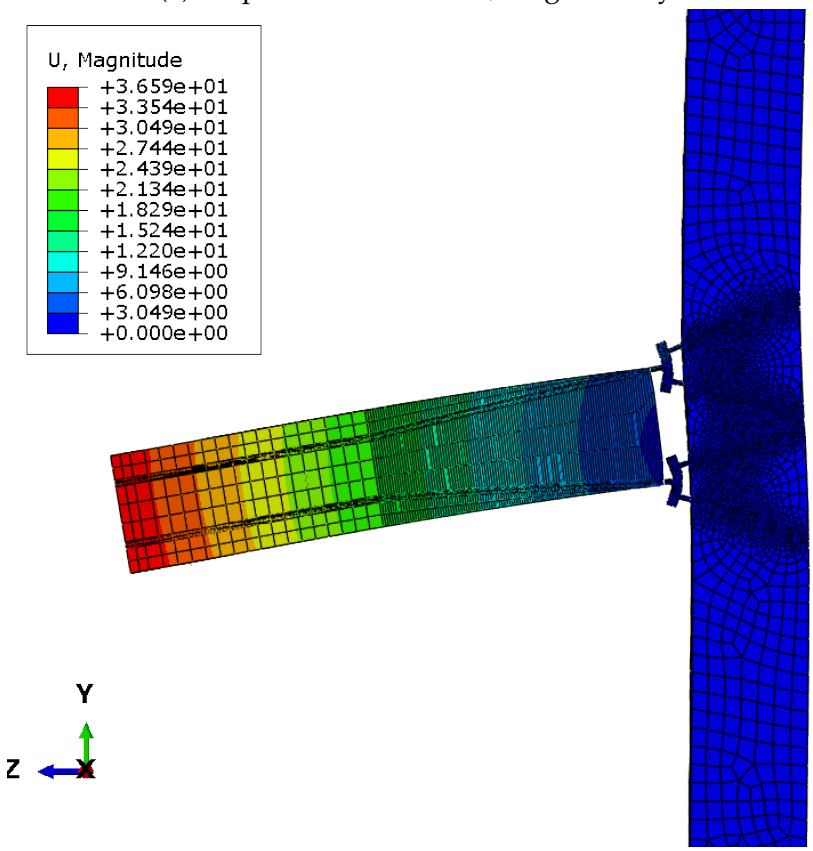

(b) Displacement 75-70-05, magnified by a factor of 10

Figure F.7

G. Digital resources

This appendix contains an overview of the digital resources used in this thesis. All the resources are delivered to supervisor Kjell-Arne Malo.

Table G.1: Digital resources

Name	Program	Description
MasterThesis-DragesetHoff.pdf	-	PDF-file of this thesis
masterthesis.zip	-	zip-folder containing the LaTeX-code including figures
ComponentMethod.xls	Excel	Spreadsheet provided by Ph.D-candidate Aivars Vilguts
ComponentMethodModified.xlsx	Excel	Modified version adapted to the new connector
Connector.xlsx	Excel	Rotational stiffness of the connectors
Loading&Stiffness.mcdx	MathCad	Calculation of the moment in the connection
ExperimentalConfigurations.cae	Abaqus	Models of the experimentally tested configurations
NewConfigurations.cae	Abaqus	Models of the new configurations
Withdrawal.cae	Abaqus	Cohesive withdrawal models
Connector.cae	Abaqus	Models of the steel connectors
Configurations.dwg	Autocad	Sketches of the configurations
Connectors/XX-XX-XX.dwg	Autocad	Sectional view of the connectors
ColumnStresses.m	MatLab	Plots of the stresses in the column
RodStresses.m	MatLab	Plots of the stresses in the rods
CohesiveParameters.m	MatLab	Plots of the cohesive parameters
CohesiveRodStresses.m	MatLab	Plots of the stresses in the rods in the withdrawal models
ForceDistribution.m	MatLab	Script calculating the distribution of forces